ELECTRON CLOUD STUDIES AT FERMILAB

BY

YICHEN JI

Submitted in partial fulfillment of the
requirements for the degree of
Doctor of Philosophy in Physics
in the Graduate College of the
Illinois Institute of Technology

Approved Linda Spentzouris
Advisor

Chicago, Illinois
December 2019

TABLE OF CONTENTS

Page

LIST OF TABLES v

LIST OF FIGURES ix

LIST OF SYMBOLS x

ABSTRACT xi

CHAPTER

1. INTRODUCTION 1

1.1. Electron Cloud formation mechanism 3
1.2. Secondary Electron Yield (SEY) studies 4
1.3. Simulation studies 7
1.4. E-cloud measurement 8

2. SEY MEASUREMENTS 10

2.1. Introduction 10
2.2. SEY station 12
2.3. SEY Measurement Results 22
2.4. Conclusion 30

3. E-CLOUD GENERATION SIMULATION 32

3.1. Introduction 32
3.2. POSINST electron cloud build-up code 34
3.3. POSINST simulation results 40
3.4. Chapter conclusion 54

4. ELECTRON CLOUD MEASUREMENTS 56

4.1. Introduction 56
4.2. The RFA set-up 58
4.3. Experimental Data 65
4.4. Comparison of data to simulations 70
4.5. Conclusion 86

5. CONCLUSION 89

5.1. SEY measurements 89
5.2. The POSINST simulations 90
5.3. RFA measurements 93

5.4. SEY coating choice for Fermilab upgrades 94
BIBLIOGRAPHY 96

LIST OF TABLES

Table Page

1.1 Beam intensity for each stage of the MI upgrades 2

2.1 Deconditioning study for TiN 27

2.2 Deconditioning study for A-Carbon 29

3.1 Simulation Inputs Parameters 39

3.2 Beam intensity for each stage of the MI, corresponding E-cloud density and SEY threshold 53

4.1 MI parameters 63

4.2 MI input parameter for BlonD simulation 72

5.1 Beam intensity for each stage of the MI, corresponding safe and danger SEY threshold 92

LIST OF FIGURES

Figure Page

1.1 E-cloud generation multipacting process. Secondary electrons are knocked off the wall due to impact of seed electrons. Relativistic proton bunches pass by further accelerating the secondary electrons. These may impact the vacuum chamber walls again, creating more secondaries. These cartoons are generated by Jeff Eldred [1]. . . . 3

1.2 SEY curves used in simulation (left), and measured with the MI station (right). 5

2.1 The SEY station 12

2.2 The station sample. 13

2.3 The isolating ceramic that separates the arm from the MI vacuum chamber. 14

2.4 The primary current is measured by applying a +150V bias to the sample and recapturing all secondary electrons; The total current is measured by applying a -20V bias to the sample and rejecting all secondary electrons. 15

2.5 Typical measurements of I_t, I_p and SEY. The 9 measurements for the 3×3 grid are superimposed in b and c. Variation in I_p is a property of the gun. 16

2.6 The leakage current measurement for general leakage current behavior and leakage current behavior over measurement time window. The leakage current was measured over 5 minutes for a general trend. The leakage current is also measured for typical measurement procedure. In a typical measurement, the system waits 3 minutes and then take leakage current measurement. The I_p measurement takes about 70 s, the I_t measurement takes about 630 s. A linear fit is applied to the I_p measurement; a 3 order polynomial fit is applied to the I_t measurement. 18

2.7 The isolating ceramic and the plastic chamber with nitrogen system. 19

2.8 Comparison between good and bad cases of the leakage current. . 21

2.9 The TiN coating rig under operation. Picture taken by David Capista and Marty Murphy. 23

2.10 The first TiN measurement set. 23

2.11 Peak SEY of samples in MI (top) and MI beam intensity (bottom) over four years of measurement. 25

2.12 TiN and SS316L comparison study. 26

2.13 A-Carbon and SS316L comparison study. 29

3.1 The Furman-Pivi-model fitted to measured SEY. 36

3.2 The SEY curves used in simulation. 37

3.3 Total E-cloud density at a single location in the RR dipole region with 5.5×10^{10} protons per bunch, total of 29×10^{12} protons. When filling pattern is 0, there is no beam in bucket, when filling pattern is 1, there is beam in bucket. 40

3.4 E-cloud density within one sigma region of the proton beam compared to the E-cloud density within vacuum chamber. The orange line is the E-cloud density inside the vacuum chamber, the blue curve is the E-cloud density with in the one sigma region of the proton beam. 41

3.5 E-cloud distribution within the vacuum chamber cross section at specific time. The blue line is the vacuum chamber. Beam located at the center of the vacuum chamber. X and y axis are position relative to the vacuum chamber center, color scale is electron counts. 42

3.6 Some other POSINST outputs. 43

3.7 Incident angle and energy distribution for wall collision over the full simulation. 45

3.8 The comparison between M. Furman's result and my simulation. . 45

3.9 Dependence of average E-cloud density over one full turn on beam intensity for different SEY values. The subfigures show this dependence for different regions of the MI and RR. The round beam pipe region for MI is on field free region. The MI dipole and MI field region share the same elliptical beam pipe. The RR field free and dipole region share the same elliptical beam pipe. 48

3.10 The SEY and beam intensity contour plots for different E-cloud densities. Each line represents sets of (Beam intensity, SEY) points that are at the threshold of the E-cloud density represented by that line. So, any Beam intensity, SEY value above the line will have at least the E-cloud density value represented by that line. In order to have an E-cloud density less that the one represented by a line, the (Beam intensity, SEY) values in the accelerator must fall below that line. 50

3.11 The E-cloud density dependence on SEY for PIP-II beam intensity (70×10^{12} protons). 51

4.1 The Retarded Field Analyzer. The picture and drawing are created by Michael Backfish [2] 59

4.2 The RFA signal over a full acceleration cycle for Main Injector. The blue trace is the raw data, and the orange trace is filtered data. The beam intensity was 50×10^{12} protons. 62

4.3 The RFA signal zoomed in for 5 turns. The blue trace is the raw data, and the orange trace is filtered data. The beam intensity was 50×10^{12} protons. Note that this is electron induced current, the signal is negative. 62

4.4 The RFA processed signal with 50×10^{12} beam intensity and 1.3 SEY. 64

4.5 The RFA signal vs screen voltage compared to collision energy simulation 66

4.6 The Peak-to-Valley RFA signal of 8 different intensities 67

4.7 The Mean-to-Valley RFA signal of 8 different intensities 67

4.8 The RFA signal measuring electron cloud density compared with the simulated bunch length (σ_t) over an acceleration cycle. The bunch length was simulated using the BlonD code with MI conditions. The beam intensity was 50×10^{12} during the measurement. 68

4.9 Simulation of the electron bombardment rate over one turn for different combinations of SEY and bunch length. One revolution (turn) takes about 11 μs. Top left: no cloud buildup, top right: build up but no saturation, bottom left: slow build up to saturation, Bottom right: fast build up to saturation. BL stands for bunch length, beam intensity = 50×10^{12}. 69

4.10 The wall current bunch length measurements at 50×10^{12} beam intensity. 71

4.11 The initial and final macro-particle phase space distribution for the MI in BlonD simulation. 72

4.12 The beam energy ramp and RF voltage ramp during the acceleration cycle used for the BlonD simulation. 73

4.13 The linear fit between the BlonD simulation result and the wall current monitor measurements 74

4.14 The BlonD simulated bunch length (blue curve); eight wall current bunch length measurements (yellow circles); and the scaled, simulated bunch length (yellow curve). 75

4.15 The POSINST simulated bunch length dependency of the electron bombardment rate for different SEY and beam intensities. 77

4.16 The POSINST simulated electron bombardment rate dependence on bunch length for different values of SEY and beam intensities. . . 78

4.17 The simulation and measurement match for the new conversion factor. Comparison of the mean to valley RFA signal and bombardment rate for the three beam intensity that show clear E-cloud build up. 81

4.18 The POSINST simulated bunch length dependency for 1.25 SEY. . 82

4.19 E-cloud bombardment rate versus bunch length for various SEY values near 1.25. 82

4.20 The simulated ratio $R_{1.43}/R_{0.9}$ for 1.125 to 1.3 SEY and 40×10^{12} to 70×10^{12} protons beam intensity. The blue curve is the ground noise level (1.25 $\mu A/cm^2$) line. RFA cannot measure data below blue line. 86

LIST OF SYMBOLS

Symbol	Definition
E-cloud	Electron cloud
SEY	Secondary Electron Yield coefficient
MI	Fermilab Main Injector
RR	Fermilab Recycler Ring
SS316L	Stainless Steel 316L
TiN	Titanium Nitride coating or Titanium Nitride coated SS316L
A-carbon	Amorphous Carbon coating or Amorphous Carbon coated SS316L
RFA	Retard Field Analyzer

ABSTRACT

The presence of unwanted electrons in an accelerator vacuum chamber, known as E-cloud (E-cloud) can potentially cause operational problems in the Fermilab Main Injector (MI) and Recycler Ring (RR). E-cloud has caused instability in the RR in the past, and although it is not currently a problem, there is measurable E-cloud in the MI accelerator. There are planned beam intensity increases due to upgrades of the Fermilab accelerator complex, so E-cloud could become a problem.

Some work has been done by others previously to understand how low SEY (Secondary Electron Yield coefficient) coatings might mitigate production of E-cloud, and to model the mechanism whereby E-cloud causes beam instability [1–4]. Using previous studies as a base, this research took several approaches toward understanding the risk of E-cloud at Fermilab. The evolution of the SEY of the SS316L (stainless steel), TiN coated SS316L, and amorphous carbon coated SS316L were measured in-situ using a SEY measurement station in the MI tunnel. The SEY of these materials change over time either due to bombardment of the E-cloud, or disruption of vacuum conditions. The SEY evolution was tracked over a several year period to find out how long it takes for the SEY of each material to reach its lowest level, and how much the SEY rises during deconditioning periods of poor vacuum. The SEY measurement results can be used to determine whether the SS316L will be a problem at upgrade intensities, and if so, whether or not TiN and A-Carbon coatings can mitigate E-cloud related problems sufficiently.

Direct measurements of the E-cloud were done as well, and compared to simulation. The E-cloud bombardment rate was measured at different beam intensities and bunch lengths. It was possible to get detailed information on how the E-cloud varies over the acceleration cycle, where sensitivity to bunch length is reflected in the evolution of the E-cloud. The Retarding Field Analyzer (RFA) measuring the E-cloud

bombardment rate was near the instrument that is used to measure the SEY of the beam pipe material. This proximity provided an accurate SEY value for simulations, so that the simulated E-cloud bombardment rate could be better compared to measurement. Bunch length measurements and computations generated accurate bunch length information also needed as input for simulations. After this careful control of the input parameters, the POSINST simulations of E-cloud were a good match to direct measurements. This gave confidence that predictions could be made concerning the E-cloud densities at upgrade intensities. These densities were compared against corresponding proton densities to predict the SEY required to avoid instabilities. That prediction and the information provided by the SEY measurements provide helpful information regarding the risks of E-cloud effects at future beam intensities at Fermilab.

CHAPTER 1
INTRODUCTION

Fermilab is currently focusing on the intensity frontier [5], meaning the goal of the lab is to produce proton beams of the highest possible intensity. The main focus of their physics program is on neutrino experiments (NuMi [6], NOVA [7], DUNE/LBNE/LBNF [8]). These neutrino experiments require high beam intensity because the more beam delivered to target, the more neutrinos that will be delivered to the experiments. Fermilab also hosts the Mu2e [9] and Muon g-2 [10] experiments, which also require high beam intensity.

As a result of these experimental requirements, a series of upgrades are either finished, underway or planned for the future. Currently, Fermilab is putting 700 kW of proton beam power onto the NuMi target [11]. The PIP [12] upgrades were finished in 2017; these increased the output beam power of Main Injector from 400kW to 700kW via slip stacking in the Recycler Ring [13]. Currently an upgrade aims to increase the Main Injector (MI) beam output power to 900 KW by increasing the Booster repetition rate from 15 Hz to 20 Hz [14]. Then the next major upgrade to be carried out is the Proton Improvement Plan Phase II (PIP-II) [15]. This is a plan to increase the beam power to 1.2MW and provide a platform for future 2MW operation by building an 800 MeV superconducting Linac. The beam powers and intensities for these upgrades are given in Table 1.1. Over the course of past upgrades, a cloud of unwanted electrons in the vacuum chamber of the accelerator, called E-cloud, was observed and even caused beam instabilities for a short time in the Recycler Ring (RR) [1]. As the beam intensity of Fermilab continues to increase due to on-going and future upgrades, E-cloud is a potential disruption to operations.

The electron cloud (E-cloud) effect [16] is the generation of unwanted electrons inside an accelerator beam pipe. E-cloud generation can cause a range of problems:

Table 1.1. Beam intensity for each stage of the MI upgrades

Stage	Beam power	Beam intensity	MI cycle time
Before PIP-I	400 kW	24×10^{12} protons	1.33s
PIP-I	700 kW	50×10^{12} protons	1.33s
Current upgrade	900 kW	55×10^{12} protons	1.2s
PIP-II	1.2 MW	70×10^{12} protons	1.2s

vacuum degradation, extra heat load on accelerator components, emittance growth and beam instabilities. E-cloud is observed at the CERN-LHC [17] and causes degradation of vacuum, extra heat load on the beam chamber, emittance growth and beam instabilities. E-cloud is also observed at the CERN-PS/SPS [18] and causes beam instability. E-cloud was observed and has caused instabilities at the BNL RHIC machine [19], and for the eRHIC project at BNL E-cloud could potentially limit the proton ring performance by over-heating the superconducting magnets [20]. At KEKB in Japan, E-cloud is observed for their positron ring [21], and studies on the mitigation of E-cloud are still on-going [22]. For the BEPC in Beijing, E-cloud is also observed and is being studied [23].

As for Fermilab, E-cloud was observed in the MI and the Tevtron as early as 2006 [24], and studies of E-cloud behavior in the Fermilab accelerator complex started then [25]. An instability caused by E-cloud was observed at RR in 2015 [1] and studied by Sergey A. Antipov as part of his thesis research [3]. In Antipov's research, he explored the mechanisms by which E-cloud causes instabilites. He found that the RR combined function magnets (a magnet that functions as both a dipole and a quadruple) trap electrons and cause E-cloud build up. The dipole component causes the E-cloud to have a spatial distribution that increases the liklihood of causing beam instabilities.

Michael Backfish did his thesis on E-cloud by studying the mitigation of

cloud formation through the potential use of coatings that could be applied to the beampipe [2]. In his thesis, Backfish studied E-cloud generation from different beam pipe coatings (Titanium Nitride, Amorphous carbon and Diamond Like Carbon) using a set of Retarded Field Analyzers (RFA) to measure the E-cloud in the region of each coated beam pipe. Comparisons were done of the E-cloud density for these different materials over time.

1.1 Electron Cloud formation mechanism

When a bunched proton beam passes through an accelerator vacuum chamber, E-cloud is generated by first creating a seed electron population that is then amplified through a multipacting process. Seed electrons are generally generated through (1) ionization of residual gas by the beam particles, (2) emission of electrons from the vacuum chamber wall due to incident synchrotron radiation and (3) lost beam particles scatter electrons off the vacuum chamber wall.

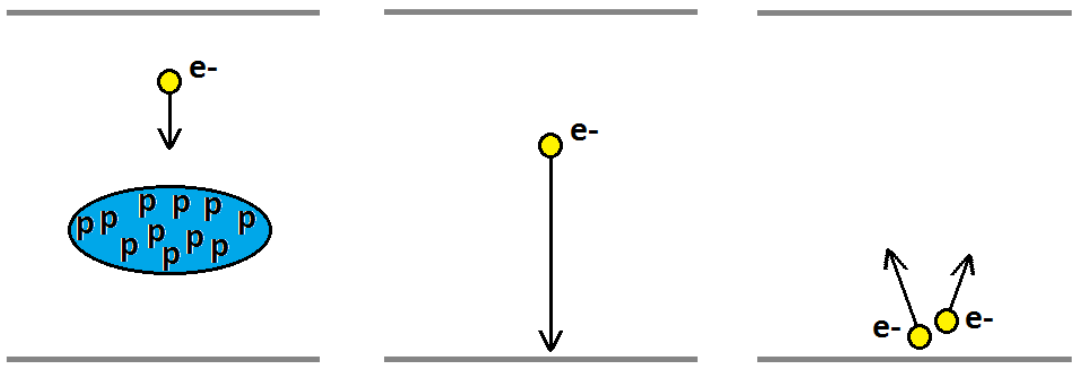

(a) A passing beam bunch energizes the seeding electron.

(b) The Seeding electron hits the vacuum chamber wall.

(c) More than 1 electron is "knocked" off the vacuum chamber wall.

Figure 1.1. E-cloud generation multipacting process. Secondary electrons are knocked off the wall due to impact of seed electrons. Relativistic proton bunches pass by further accelerating the secondary electrons. These may impact the vacuum chamber walls again, creating more secondaries. These cartoons are generated by Jeff Eldred [1].

The E-cloud generation multipacting process is shown in figure 1.1. First the seed electrons get energized by a particle beam bunch, then the energized primary seed electrons hit the vacuum chamber wall and "knock" out more than one electron (the secondary electron emission process), then the next proton bunch comes along to the location of electron production and energizes the secondary electrons, and the whole process repeats. The electron population inside the beam pipe grows exponentially during this process, forming an E-cloud. Eventually this process will reach an equilibrium E-cloud density when the force between the electrons cancels the kick from the beam [25].

The E-cloud build up is a dynamic process. There is no reliable theoretical model that describes the process. Simulations are needed to study and understand the process. There are many input parameters that are needed to generate reliable simulation results. The beam parameters, beam pipe geometry, and externally applied fields all have to be well known for accurate modeling by the simulation. Luckily, the majority of these input parameters required to simulate the E-cloud generation process are well known for the Fermilab accelerator complex. One major parameter that has not been well known for the Fermilab accelerator complex is the Secondary Electron Yield (SEY) coefficient.

1.2 Secondary Electron Yield (SEY) studies

The Secondary Electron Yield coefficient (SEY) measures on average how many electrons got knocked off the material surface with one incident electron. It is defined as the following equation

$$SEY = \frac{I_{SEY}}{I_{Incident}} \tag{1.1}$$

Where $I_{Incident}$ is the incident electron current and the I_{SEY} is the secondary electron current. The SEY is a material surface property. The SEY of a lot of materi-

als are well studied for the purpose of understanding the secondary electron emission process [26, 27]. In addition to its role in the production of E-cloud, the secondary electron emission process plays a major role in other applications. In the R&D of RF cavities, the secondary electron emission process plays a major role in multipacting, a process where electrons get energized by an oscillating RF field, generating an E-cloud and causing problems [28, 29]. For scanning electron microscopes, the secondary electron emission is an important tool in constructing the surface image [30].

During E-cloud build up, the SEY determines how many secondary electrons are created. The exponential growth rate heavily depends on the SEY. The SEY is a function of the incident electron energy E_0 and the incident angle θ of the primary electrons. Figure 1.2 shows the SEY dependence on incident electron energy; the right plot shows SEY curves obtained from measurements in the MI, while the left plot shows SEY input curves for E-cloud simulations.

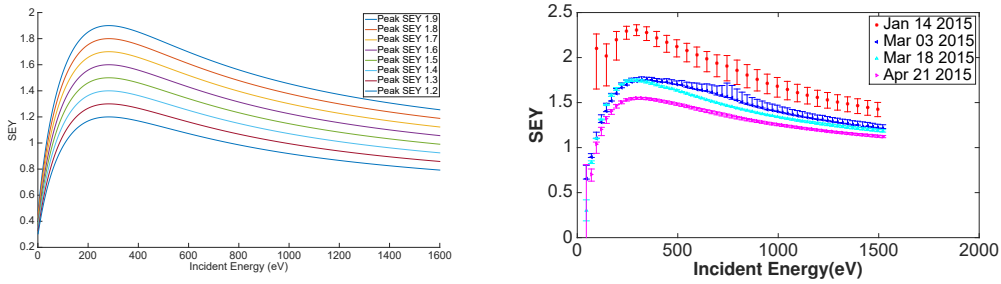

(a) SEY curves used in simulation.

(b) SEY curves of stainless steel measured in MI.

Figure 1.2. SEY curves used in simulation (left), and measured with the MI station (right).

Since the SEY curve is a material surface property, the surface condition of a material can change its SEY curve dramatically. When electrons bombard a material surface there is a "dose" effect, or conditioning process, that slowly decreases the SEY of the surface [31]. The E-cloud build-up process involves electrons bombarding

the material surface. Even after the E-cloud is saturated and the E-cloud population stops growing, the electrons are still bombarding the material surface. Thus, the E-cloud "cooks" the vacuum chamber surface, and decreases the SEY over years of accelerator operation.

To understand the E-cloud build up process, it is important to have a good understanding of SEY curve and also of how that SEY curve changes over accelerator operation cycles. E-cloud generation can be suppressed by low enough SEY. In some cases, E-cloud related problems can be resolved by the decreasing SEY of the vacuum chamber wall as it conditions. Since the SEY of an accelerator will conditions to lower values because of normal accelerator operation, it is plausible that E-cloud related problems will vanish spontaneously because of the conditioning effect. The instability observed in the RR vanished in later operations [1, 11]. In cases that conditioning effects fail to reduce the SEY to a point where E-cloud related problems vanish, applying a low SEY coating on the beampipe or using a low SEY material can potentially solve the problem. In order to solve the SEY related problems, an understanding of the SEY properties of the beampipe and how they change over time is necessary.

One of the main focuses of this research was to monitor the long-term development of SEY curve behavior over many accelerator cycles. This was done using an in-situ MI station that allowed deployment of different materials and coatings directly into the beampipe wall. The measurement of SEY for different materials has been on-going for years, both for accelerator related research and in other fields of physics [30–33]. The SEY of pure metals has been well studied decades ago [26]. The research of low SEY coatings have been on-going in the field of accelerator physics. An Amorphous Carbon (A-Carbon), coating was developed at CERN for their accelerator complex [34, 35]. A Titanium Nitride (TiN) coating has successfully decreased

the SEY at KEK [36]. KEK also developed a Diamond Like Carbon (DLC) coating for their accelerator complex [37]. In this research, Stainless Steel 316L (SS316L), TiN coated SS316L and A-Carbon coated SS316L samples were installed on the MI beam pipe wall for in-situ SEY measurements. The SEY development studies of SS316L, TiN coated SS316L and A-Carbon coated SS316L in the MI environment is presented in Chapter 2. While lower SEY materials are being tried out worldwide for accelerators, detailed studies of how they condition in the presence of beam, and decondition when vacuum degrades, is rarely done. A special station is needed that can be installed in the tunnel at the accelerator beampipe. At Fermilab this station is located very near a detector that can directly monitor the electron cloud. This provides a unique opportunity to study E-cloud properties when the SEY is well known.

1.3 Simulation studies

Since a theoretical solution for E-cloud generation is not available, it is necessary to simulate the process in order to understand E-cloud build-up. E-cloud related simulation codes are generally classified into two types. E-cloud build-up codes that treat the beam as a static input, only track the E-cloud activity and ignore the E-cloud beam interactions. POSINST [38–41] and PyECLOUD/ECLOUD [42–46] are some of the widely used build-up codes. WARP-POSINST [47, 48] is a widely used E-cloud/beam interaction self consist code, the self consist code track the activity of both beam and E-cloud. The dramatic difference in the time scale of E-cloud development and beam development requires a large amount of computational power to model the interaction of the beam and the E-cloud. The E-cloud develops on a bunch-by-bunch time scale, while the beam develops on a turn-by-turn time scale. The beam revolution frequency in the MI is 90 kHz, with a 11 μs period, and there are 588 buckets (spaces that could hold one bunch of beam) over the full ring. The beam

bunches pass a specific location in the ring with a frequency of 53 MHz, with an 18 ns period. The bunch-by-bunch time scale is 588 times higher than the turn-by-turn time scale.

Based on the findings of a previous RR instability study [1,3], the E-cloud has to reach certain electron density to cause an instability. Even when such an instability occurs, if conditioning of the beampipe material is still in progress, the problem may resolve itself as the SEY drops. The 2015 instability observed in the RR did go away without active remediation. Based on simulation studies for this and other research [49], the E-cloud population can have up to 5 orders of magnitude difference for different beam parameters and SEY values. E-cloud build-up simulations are needed to figure out weather or not E-cloud will cause problems in a specific parameter space.

The POSINST code was used to simulate the E-cloud build up process in this research. POSINST was used to study the E-cloud population dependence on SEY, beam pipe geometry, external magnetic fields and beam parameters. Important beam parameters that heavily influence E-cloud generation are beam intensity (number of protons inside beam pipe) and bunch length (beam longitudinal distribution); both of these affect the particle density of the protons in the beam. E-cloud density dependence on SEY, beam intensity and bunch length are presented in Chapter 3. Calculated SEY thresholds to suppress E-cloud at beam intensities planned for the upgrade are also presented in Chapter 3.

1.4 E-cloud measurement

There are many ways to determine the presence of an E-cloud. A beam instability or emittance growth may indirectly indicate E-cloud generation. There are also methods to directly measure E-cloud generation. Jeff Eldred's and Seygey A.

Antipov's studies were based on a microwave sideband measurement of the E-cloud density for MI and RR [3, 4]. Michael Backfish used the Retarded Field Analyzer (RFA) to measure the E-cloud density for MI [2]. The RFA measures the bombardment rate from the E-cloud generation process at a small part on the beam pipe wall.

In this research, the RFA was used to measure the E-cloud generation process. The RFA used in this research is the same instrument used by Michael Backfish [2], with modification of the data acquisition and analysis procedure. These modifications are based on Ubaldo Iriso Ariz's study at RHIC [50].

The E-cloud build up process was successfully observed in MI using the RFA. The dependence of the E-cloud bombardment rate on beam intensity, bunch length and fill pattern was measured. The RFA measurement results are compared with the POSINST simulation results in Chapter 4.

Combining POSINST simulation results, SEY measurements and RFA E-cloud measurements, estimates were made about what operational conditions will suppress the E-cloud. These estimates may help guide the decision about whether or not the TiN coated beam pipe, the A-Carbon coated beam pipe, or the original SS316L is the best choice for suppressing E-cloud generation for MI and RR as they go up to PIP-II intensity.

CHAPTER 2

SEY MEASUREMENTS

2.1 Introduction

Understanding how the SEY changes with beam conditioning and having accurate SEY measurements are important steps toward understanding the E-cloud generation process and its implication for accelerator and beam dynamics. The SEY is a primary input parameter to any E-cloud simulation code, and it has a dominant impact on the development of E-cloud. A low enough SEY will suppress E-cloud generation completely.

the effect of surface conditioning due to electron bombardment in an actual accelerator environment has only been studied recently; however, the SEY of different materials and coatings have been studied for many years [27]. Previously, samples exposed to E-cloud in an accelerator environment had to be removed from the accelerator and taken to an external lab for SEY measurements. This meant that the time between measurements took months and introduce uncertainty if the samples were not kept under vacuum during the transfer, knowledge of any surface conditioning could be lost. A series of measurements of SEY in an electron accelerator has been on-going at Cornell [51]. These experiments utilize a SEY measurement stand in the accelerator tunnel and the SEY measurements are done during accelerator shut downs. Cornell has an electron machine, so synchrotron radiation is a factor in the electron cloud dynamics there. As part of this work, measurements are now performed at the Fermilab MI, and are the first such in-situ measurements done in a proton machine [52].

The SEY of a material can change due to the "dose" effect or conditioning effect [31]. Different ways of treating the surface will greatly affect the SEY value, since

the SEY is a material surface property. Baking with high temperature, or exposure to a high density plasma could potentially change the SEY of a surface [33]. It is observed that exposing a surface to electron bombardment can also decrease the SEY. The conditioning effect may happen because of the material's surface contamination that is scrubbed off [27]. In other words, the E-cloud serves as an electron shower that "cooks" the material surface, removing surface contamination, thus conditioning the material surface and decreasing the SEY. On the other hand, measuring the SEY development of a surface under accelerator operational environments provides insights about the E-cloud development in accelerators.

This chapter begins with a description of the SEY measurement station, the data interpretation procedure, and analysis of issues with the station. The main source of error of the SEY station measurements came from the leakage current. Two currents (I_p and I_t) are measured by the station with different bias voltages (150 V and -20 V), then the SEY is calculated based on these two currents. The bias voltage will cause leakage current flow through the isolating ceramic and cause error for the SEY measurement. The leakage current was measured and studied. The leakage current induced error was calculated. In order to mitigate the leakage current, a Faraday box and a dry nitrogen feeding system were installed. The leakage current induced error is controlled to less than 2% for the majority of SEY measurements.

A series of measurement results for stainless steel 316L (SS316L), Titanium Nitride (TiN) and Amorphous Carbon (A-Carbon) coatings are presented. The measurements took place from 2013 to 2019. The first year measurement period was a calibration run. The TiN and SS316L comparison measurements happened over the 2014 to 2017 period. During this time, the MI beam intensity increased from 25×10^{12} to 50×10^{12} protons. The A-Carbon and SS316L comparison measurements happened from 2018 to 2019, and the MI beam intensity was 50×10^{12} protons. During the

long shutdowns, a series of deconditioning studies were conducted. The deconditioning studies showed that the vacuum chamber preserves the conditioned SEY value to some extent. The venting of the vacuum chamber drastically increases the SEY of previously conditioned samples.

2.2 SEY station

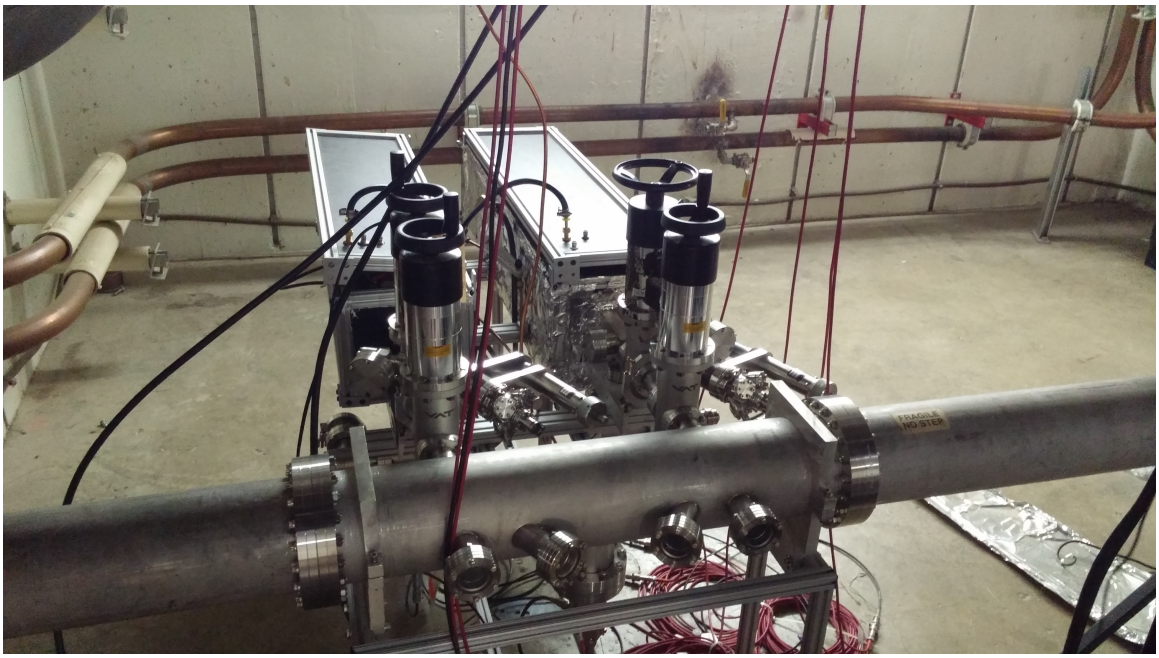

Figure 2.1. The SEY station

The measurement stand used at Fermilab (figure 2.1) was originally designed and built by Cornell. Modifications were made so that it would fit the MI vacuum vessel, and to improve the signal to background ratio for the MI tunnel conditions. The station is located in the MI-10 area of the MI. The location was chosen due to the station space requirement (it needs space behind the beam pipe). The MI-10 area provides a relatively field free background (certain areas of the tunnel have stray magnetic fields which can deflect the electrons). The measurement stand has two arms so that two samples are exposed to the same environment simultaneously for direct comparison. The arms' vacuum can be isolated from the MI vacuum so that

the station can be operated and sample changed more freely.

Figure 2.2 shows one of the samples; the sample is a small curved piece that sits on the vacuum chamber wall. The samples are retracted from the vacuum chamber wall on an electrically isolated arm during measurements and put back afterwards for continuous monitoring of the conditioning effect. Figure 2.2(b) shows how the samples are fit to the beam pipe. Two Kimball Physics ELG-02 electron guns were installed and are directed towards the sample at a 15° angle, which will increase the measured SEY by 1% compared to normal incidence, according to the Furman-Pivi probabilistic model [40]. A Keithley 6487 Pico-Ampmeter is used to measure electron gun beam current and apply bias voltages.

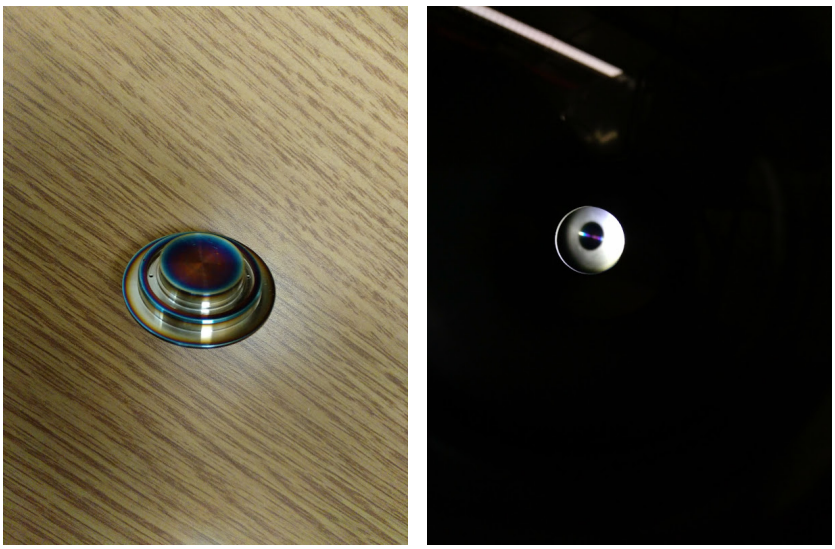

(a) The sample on table (b) The sample in vacuum chamber

Figure 2.2. The station sample.

Each arm of the SEY station consists of two parts that are electrically isolated by a ceramic as shown in figure 2.3. The sample sits on the tip of the arm in figure 2.3. A beam of electrons from the electron gun is sent to the sample and scanned over a range of predetermined energies, the current from the electron beam is measured between the arm and the ground. Using the correct bias voltage, the primary and

secondary electron currents are measured at each energy.

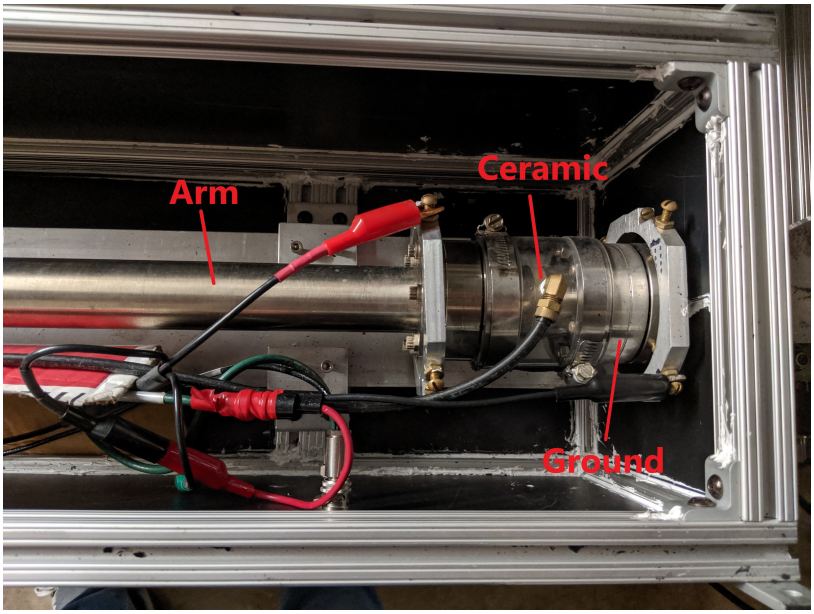

Figure 2.3. The isolating ceramic that separates the arm from the MI vacuum chamber.

A LabView interface originally developed at Cornell is used to control the data acquisition process, it is based on an interface from Kimball Physics and Keithley. During a typical scan, the energy spectrum ranges from 25 eV to 1525 eV with 25 eV increments, the electron beam is directed to a 3×3 grid that at a 1 mm pitch, with a 1 mm^2 spot size on the sample. The control system is mounted on a moving cart. The cart is stored outside the accelerator tunnel and must be moved to the station for each measurement. The measurement cannot be taken remotely so all measurements are taken during accelerator shutdowns.

2.2.1 SEY Measurement Principles. Two currents are measured on the sample with two different bias voltages. The effect of the bias voltage is shown in figure 2.4. As shown in Figure 2.4(a), the primary current I_p is measured by applying a +150V bias voltage to the sample that insures recapture of all secondary electrons. This is a direct measurement of the electron current produced by the gun. As shown in Figure

2.4(b), the total current I_t is measured by applying a -20V bias voltage to the sample that repels all low energy secondary electrons. Then the secondary emission current is given by $I_{SEY} = I_t - I_p$. The SEY can be calculated by the following equation.

$$SEY = \frac{I_{SEY}}{I_p} = \frac{I_t - I_p}{I_p} \tag{2.1}$$

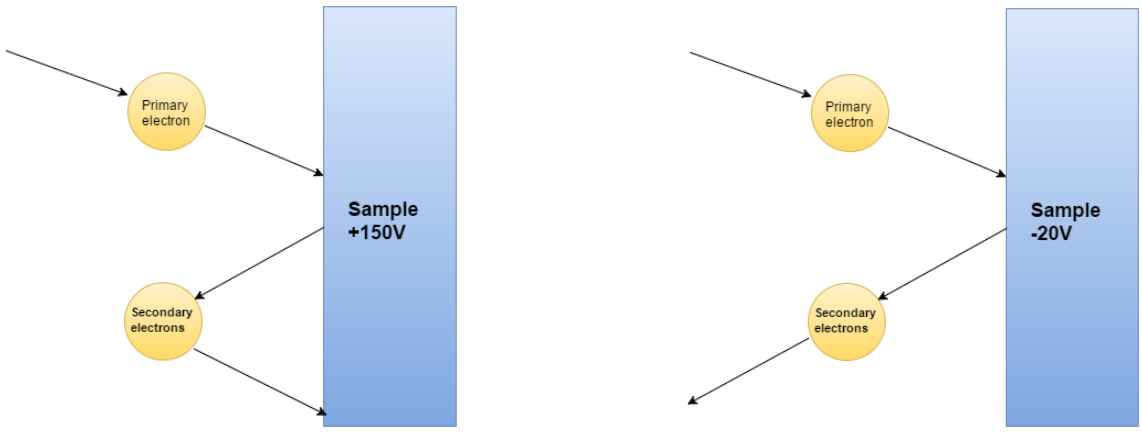

(a) Ip (b) It

Figure 2.4. The primary current is measured by applying a +150V bias to the sample and recapturing all secondary electrons; The total current is measured by applying a -20V bias to the sample and rejecting all secondary electrons.

The $-20V$ and $150V$ bias voltages were decided based on experiments. With the electron beam on, a negative bias voltage decreases the current measured by the picoammeter. The measured current decreases as the bias voltage becomes more negative. As the bias voltage reaches $-20V$, the measured current stops changing. The $150V$ bias voltage is determined with the same process. For the case of the positive bias voltage, as the bias voltage increases over $150V$, the current measured by the picoammeter reaches a plateau.

Typical measurement results are shown in figure 2.5. The I_p is only measured once, since it is only dependent on the electron gun current. The I_t is measured by rastering the beam from the electron gun across the 3×3 grid, for a total of 9 measurements. The I_t measurements lay on top of each other pretty well when the

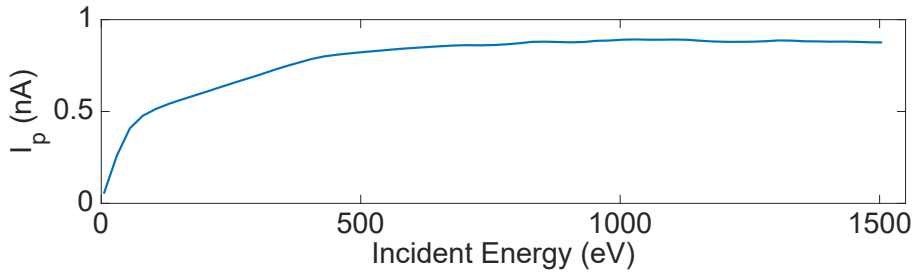

(a) I_t

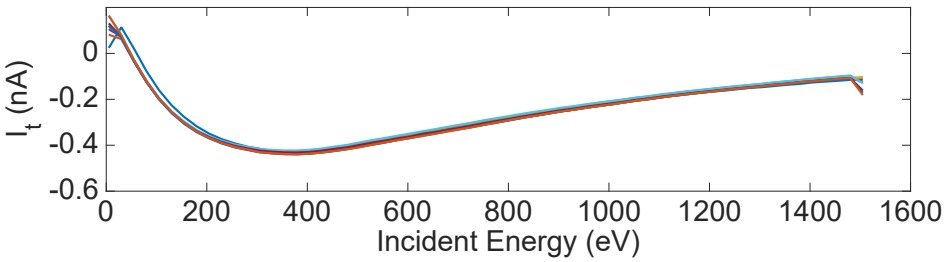

(b) I_p

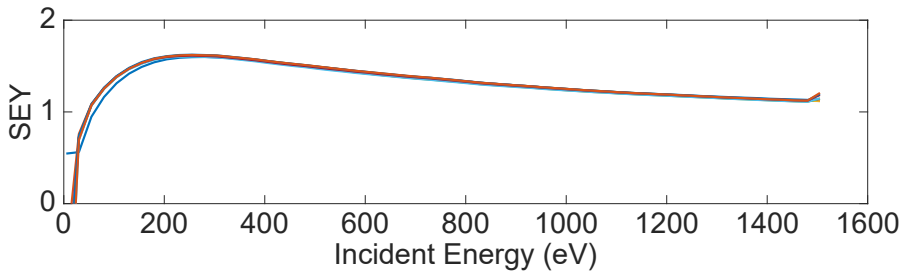

(c) SEY

Figure 2.5. Typical measurements of I_t, I_p and SEY. The 9 measurements for the 3×3 grid are superimposed in b and c. Variation in I_p is a property of the gun.

measurement error is reduced. The major error source for the measurement is leakage current.

2.2.2 Leakage current. It is hard to isolate the sample from the rest of the station so that the bias voltage is only applied to the sample. The bias voltage is applied to the whole arm in figure 2.3 (arm 60cm long). This floating arm set-up is vulnerable to bias voltage induced leakage current. Due to the the low signal level from the electron gun, the bias voltage induced leakage current can cause very high

backgrounds during measurements. The leakage current can reach as high as tens of nano-Amperes while the signal current is on the order of hundreds of pico-Amperes. Potentially, the leakage current noise can be 3 orders of magnitude higher than the signal. To generate a reasonable result, the noise to signal ratio has to be kept to at least 1 to 1. Even with relatively low leakage current, there is an upper limit on the electron gun current.

It is impossible to achieve a low signal-to-noise ratio if the leakage current is ignored. Thus, the leakage current must be compensated for during data analysis to calculate an accurate value for the SEY. Making matters more difficult, the leakage current can be unstable over the course of a measurement, which brings another source of error to the measurement results. A series of studies was done on the control and compensation of leakage currents. Figure 2.6 shows general leakage current behavior. The leakage current generally takes 2 to 5 minutes to reach a steady level (figure 2.6), so before making an SEY measurement it is necessary to wait for the leakage current to become steady. Even after the leakage current reaches a steady level, there still can be a large variation over the measurement time period. Figure 2.6(b) and 2.6(c) show the leakage current variation over the measurement period. A polynomial fit is applied to indicate a general trend.

The leakage current is generally caused by moisture in the isolating ceramic and non-infinite resistance between cables and surrounding metal (< 1 TΩ). The station was slightly modified in order to reduce both leakage current and leakage current variations. The following improvements were made: (1) In order to shield the arms from capacitively induced current, a Faraday box was implemented to shield the arms (black box in figure 2.1), (2) In order to reduce moisture at the isolating ceramic, a nitrogen purging system was implemented to control humidity around the ceramic. A small plastic case that wraps the ceramic was added so that, dry nitrogen

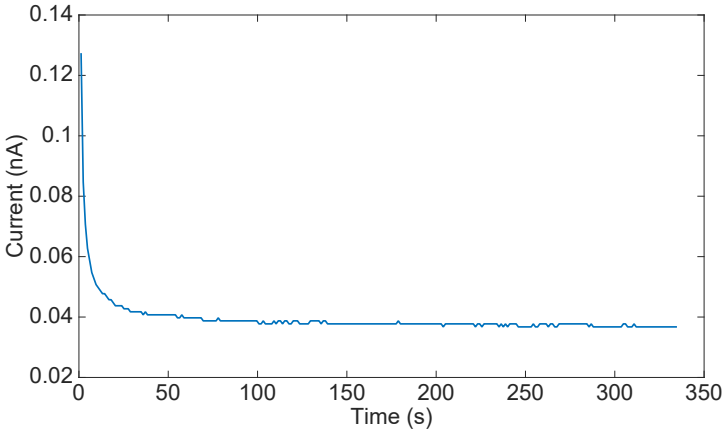

(a) Leakage current with 150 V bias over 5.5 minutes.

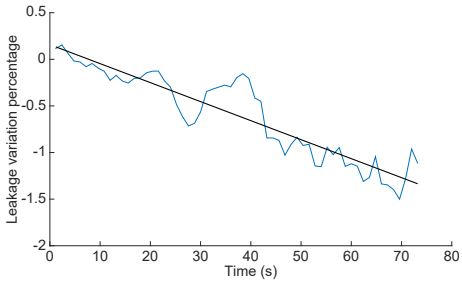

(b) Leakage current variation for I_p, 150 V

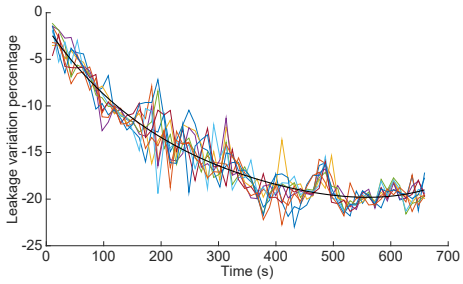

(c) Leakage current variation for I_t, -20 V

Figure 2.6. The leakage current measurement for general leakage current behavior and leakage current behavior over measurement time window. The leakage current was measured over 5 minutes for a general trend. The leakage current is also measured for typical measurement procedure. In a typical measurement, the system waits 3 minutes and then take leakage current measurement. The I_p measurement takes about 70 s, the I_t measurement takes about 630 s. A linear fit is applied to the I_p measurement; a 3 order polynomial fit is applied to the I_t measurement.

could be fed into the small case to drive away the moisture. (figure 2.7 shows the plastic case), (3) In order to reduce leakage current, a simple rack was built inside the Faraday box in order to hold the wires inside and isolate the biased floating arm from the surrounding metal. These modifications successfully controlled the leakage current, keeping it down to tens of pico-Amperes.

Even with these precautions, leakage currents are still not negligible for SEY measurements. The leakage current also varies over time, so a specific value of leakage

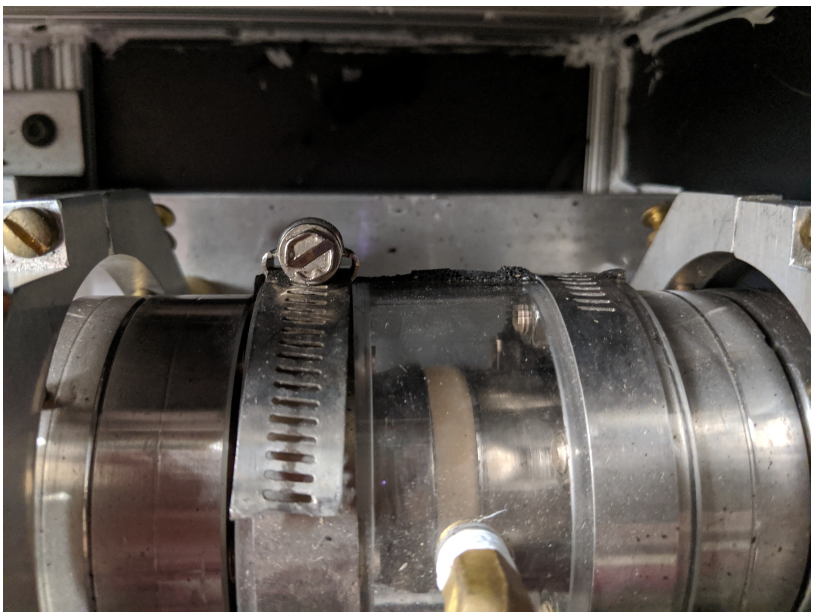

Figure 2.7. The isolating ceramic and the plastic chamber with nitrogen system.

current for each SEY measurement is independently measured. Then, this leakage current is subtracted from the measured I_p and I_t currents for the SEY calculation. To compensate for the leakage current, the following modification needs to be made to the SEY calculation equation:

$$SEY = \frac{(I_t - \delta I_t) - (I_p - \delta I_p)}{(I_p - \delta I_p)} \tag{2.2}$$

where δI_t and δI_p are the leakage currents. Based on equation 2.2, the error induced by the leakage current can be calculated based on the following equations:

$$\Delta_p SEY = \frac{\Delta(\delta I_p)}{I_p - \Delta(\delta I_p)} \tag{2.3}$$

$$\Delta_t SEY = \frac{\Delta(\delta I_t)}{I_p} \tag{2.4}$$

where $\Delta(\delta I_t)$ and $\Delta(\delta I_p)$ are leakage current variations. Based on equation 2.3 and 2.4 the leakage current induced error can be reduced by having I_p be as high as possible, since I_p is inversely proportional to the leakage current induced error. However, there

is a limitation on how high the I_p can go. Because I_p is the electron current that is bombarding the sample surface, I_p needs to be small enough so that the electron beam does not cook to the sample surface, and reduce the SEY during the measurement. The rule-of-thumb is that it takes a $1\,\mathrm{C/m^2}$ electron dose to cause a noticeable change in the SEY [31]. This limit mainly applies to fresh samples, conditioned samples take a lot more electron dose to further condition. As a fresh surface conditions, this limit decreases by several orders of magnitude. For a well-conditioned surface this limit will be on the order of 10000 $\mathrm{C/m^2}$ [31]. The whole measurement should deposit significantly fewer electrons than this limit. With a primary current of $I_p = 1\,\mathrm{nA}$ over the 10 minute measurement, the surface electron bombardment will give an electron dose of 0.067 $\mathrm{C/m^2}$. Unless the leakage current is really bad, I_p is generally under 1.5 nA.

When the leakage current is really high, in order to get a reasonable result, the I_p is generally kept a little higher than δI_p. For the case when the leakage current is above 10 nA, the measurement does not generate reasonable results as the I_p must be limited lower.

2.2.3 Measurement with "good" or "bad" leakage current. In order to calculate the leakage current induced error, the leakage current variation was measured. The leakage current induced error is calculated based on the measured leakage current. Figure 2.8 shows a comparison between good and bad cases of the leakage current. In the good case, the 150V bias voltage induced leakage current is between 77.6 pA to 80 pA with variation less than 3 pA; whereas in the bad case, the leakage current is between 120 pA and 220 pA with 100 pA variation. Assuming that $I_p = 1\,\mathrm{nA}$ and that the measured SEY is 1.3, and plugging these number into equation 2.3:

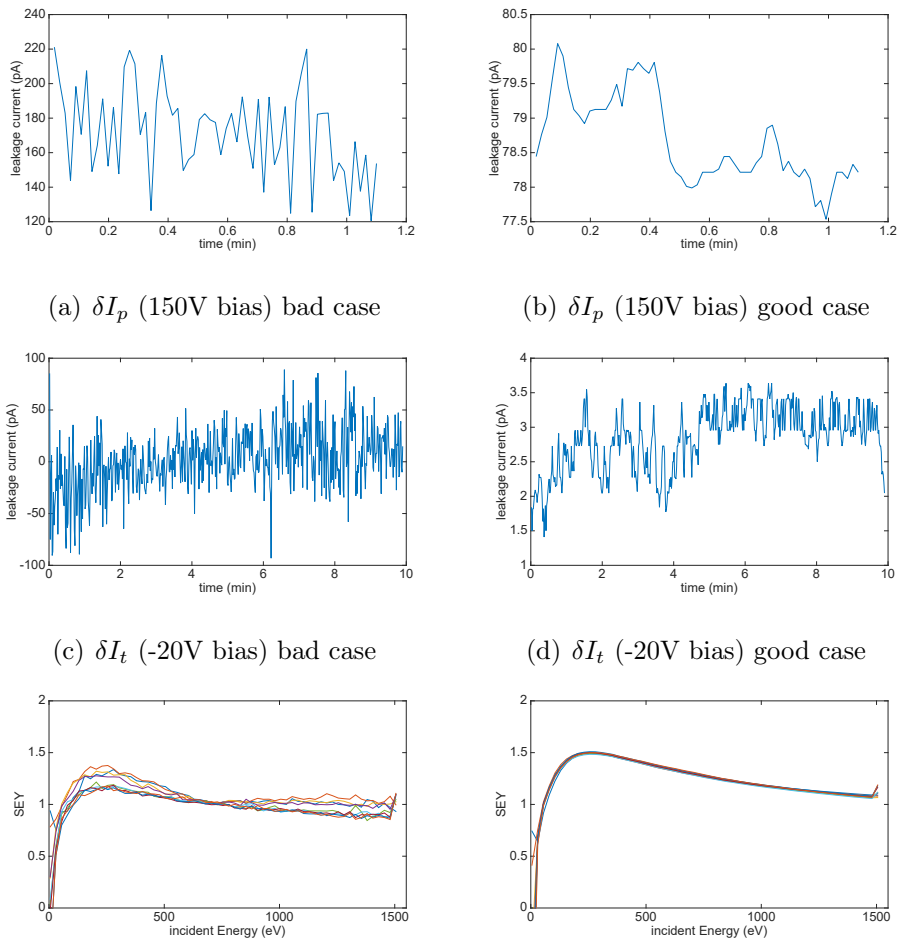

(a) δI_p (150V bias) bad case

(b) δI_p (150V bias) good case

(c) δI_t (-20V bias) bad case

(d) δI_t (-20V bias) good case

(e) SEY bad case

(f) SEY good case

Figure 2.8. Comparison between good and bad cases of the leakage current.

$$\Delta SEY = \frac{\Delta(\delta I_p)}{I_p - \Delta(\delta I_p)}$$
$$\Delta SEY = \frac{3\,pA}{1000\,pA - 3\,pA} \approx 0.003$$
$$\Delta SEY = \frac{100\,pA}{1000\,pA - 100\,pA} \approx 0.11$$

For the good case, the 150V bias voltage induced error is about 0.3%. For the bad case, the 150V bias voltage induced error is about 10%.

For -20V bias case, good leakage current is between 1.5 pA and 3.5 pA, while

bad leakage current is between -90 pA and 90 pA. Assuming $I_p = 1$ nA and that the measured SEY is 1.3, and plugging these numbers into equation 2.4:

$$\Delta SEY = \frac{\Delta(\delta I_t)}{I_p}$$
$$\Delta SEY = \frac{2\,pA}{1000\,pA} \approx 0.002$$
$$\Delta SEY = \frac{180\,pA}{1000\,pA} \approx 0.18$$

For the good case, the -20V bias voltage induced error is about 0.2%. For the bad case, whereas the -20V bias voltage induced error is about 20%. As will be shown in the discussion of simulations results in the next two chapters, a 0.1 difference in SEY could potentially cause 5 orders of magnitude difference of the E-cloud population within the vacuum chamber. It is important to keep the error under control for the measurements. From experience over years of operating the SEY station, the leakage current values are generally good for short 1–2 day shutdowns embedded during accelerator operation time. The bad case mainly appears during the 1–2 month long shutdown periods. This is because when the accelerator is operating, the accelerator tunnel is kept more dry.

2.3 SEY Measurement Results

From 2013 to 2019, three materials were studied. The original MI beam pipe material is stainless steel 316L (SS316L), so the SS316L was used as a control sample installed in one arm of the station to be compared with Titanium Nitride coated SS316L (TiN) and Amorphous Carbon coated SS316L (A-Carbon) installed in the other station arm. Titanium Nitride (TiN) coatings have been observed to suppress E-cloud generation at KEKB LER [36]. Amorphous Carbon has been observed to suppress E-cloud generation at the CERN SPS [35]; the CERN group produced the A-Carbon sample used in this study [34]. The effect of the TiN and A-Carbon on E-cloud generation in the MI was previously studied with the retarding field analyzer

(RFA) [2], but the SEY of these materials were not measured in that study. The SEY development of the TiN and A-Carbon coatings are now measured and will be compared to the SS316L sample in the following part of the chapter. The TiN sample was produced at Fermilab locally with a sputtering coating rig developed in 2011. The TiN coating rig was designed to coat a section of beam pipe. Figure 2.9 shows the coating rig under operation. The A-Carbon sample used in this study was originally produce at CERN with magnet sputtering technique. CERN coated a piece of beam pipe for Michael Backfish's study, a round piece was cut from the original A-Carbon coated beam pipe and welded onto the measurement stand sample.

Figure 2.9. The TiN coating rig under operation. Picture taken by David Capista and Marty Murphy.

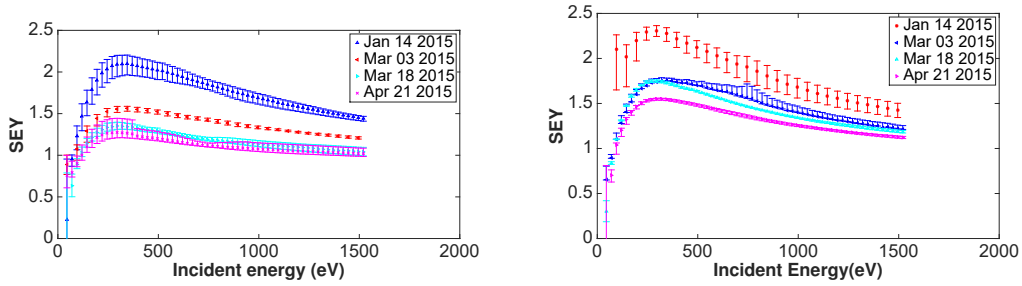

(a) TiN coating

(b) SS316L

Figure 2.10. The first TiN measurement set.

After a two year long shut down, the Fermilab accelerator complex was turned on in late 2013. In a typical year of operation, the accelerator is generally turned off

from late June to early October. From 2013 to 2017, the Proton Improvement Plan (PIP) [12] was implemented, and the beam intensity gradually increased from 24×10^{12} protons to 50×10^{12} protons per acceleration cycle (figure 2.11(b)). A total of five sets of SEY measurement data were collected during these years. The first set was taken during the engineering run, when the station calibration and data analysis procedure were finalized. The other four sets of data were standard SEY measurement studies. During the second to fourth measurement periods a comparison study of TiN to bare SS316L was carried out. During the fifth data period a comparison of A-Carbon and SS316L was done. From the 2013 to 2019, the MI vacuum at the MI-10 area was never broken. The surface of the beam pipe had been conditioned for 5 years, while the samples were conditioned for at most 250 days during a specific measurement period.

Figure 2.10 shows the first data set of the TiN and SS316L comparison. Over this period of acceleration operation, the beam intensity increased from 24×10^{12} protons, to 34×10^{12}. The SEY clearly conditioned over the three month period. In order to study the conditioning effect more quantitatively, the peak SEY for each measurement is extracted and compared with the beam intensity during the measurements.

Figure 2.3 shows the peak SEY from all SEY measurements compared with the beam intensity over the same time period years of measurements. Two different SS316L samples were used; one for the comparison of SS316L with the TiN coating and one for the comparison with the A-Carbon coating. Over the 3 sets of TiN measurements, the beam intensity increased to 50×10^{12} protons. Over the A-Carbon measurement, the beam intensity kept steady around 50×10^{12} protons.

Every year, there is a 2 to 3 month accelerator shut down period for the Fermilab accelerator complex. The shut downs are shown in figure 2.11(b) as large

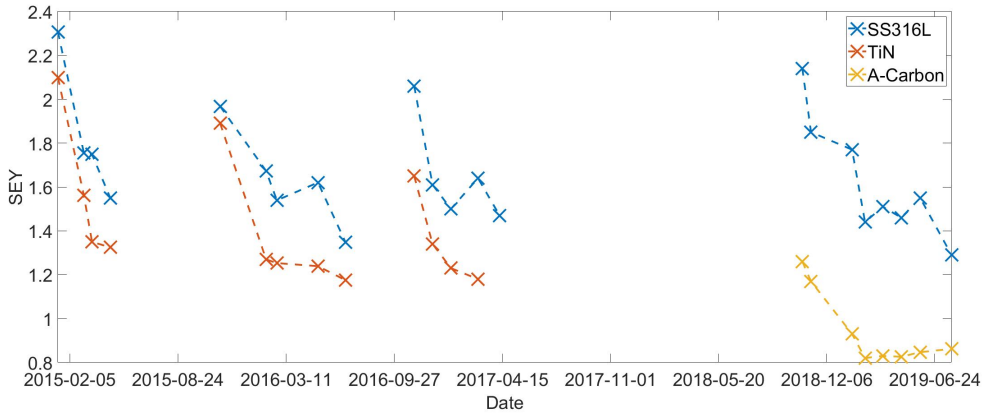

(a) SEY

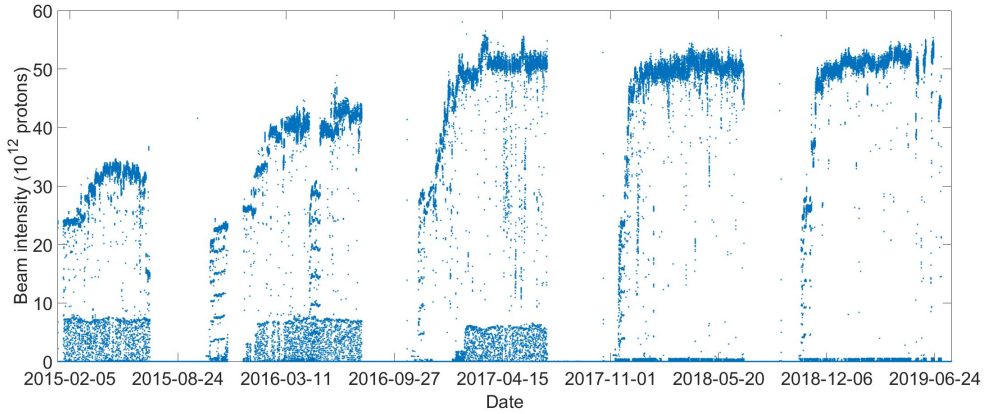

(b) Beam intensity

Figure 2.11. Peak SEY of samples in MI (top) and MI beam intensity (bottom) over four years of measurement.

portions of the plot with zero intensity. During the shut downs, deconditioning was observed to occur and was studied for the samples. The SEY for the samples gets "reset" to higher values during the time when the machine is not operating.

2.3.1 The Titinium Nitride coated Stainless Steel 316L. Figure 2.12 shows the SEY plotted against time for the period that the the sample was exposed to beam operation. The first TiN measurement was done on Jan 14th 2015, starting the first round of TiN studies. The last measurement of this first round was done on Apr 21th 2015. The sample was exposed to beam for a total of 97 days, during

which 11.1×10^{19} protons were accelerated by the MI. During this first round of exposure, the SEY for the TiN sample conditioned to 1.32, while the SEY of SS316L conditioned to 1.55. During the second round of studies, samples were exposed for 232 days while a total of 39.7×10^{19} protons were accelerated in the MI. The SEY conditioned to 1.18 for TiN and 1.35 SS316L. For the last round, samples are exposed for 158 days and a total of 32.1×10^{19} protons. The SEY conditioned to 1.18 for TiN and 1.47 for SS316L. The samples conditioned the most between the first two measurements. After the first two measurements, the conditioning process slows down and reaches a relatively steady plateau. The first 60 days and 15×10^{19} protons did the most conditioning. This observation is in agreement with a quantitative conditioning study [31] that found the electron dose required to decrease the SEY by the same increment increases exponentially as the SEY decreases.

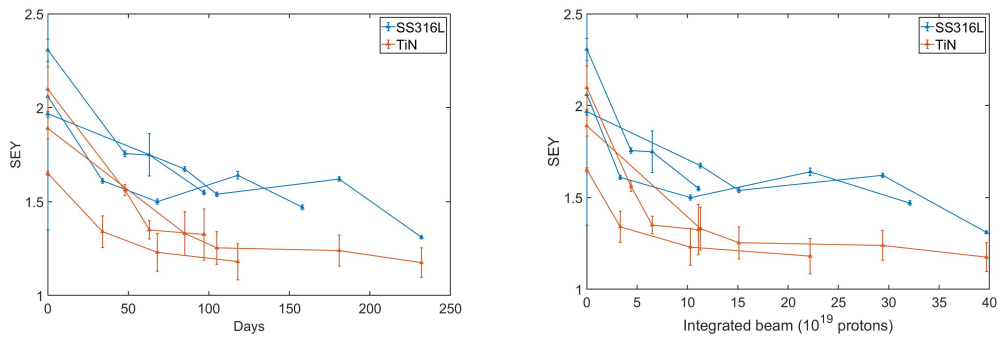

(a) SEY over time

(b) SEY over integrated beam intensity

Figure 2.12. TiN and SS316L comparison study.

Figure 2.12(a) shows that the SEY for stainless steel increased over a portion of the measurement period. This increase happened due to an operational error. The SS316L sample was stored in the measurement position rather than exposure position for 76 and 50 days for the second and last round of TiN studies. The SEY deconditioned by about 0.1 over those periods. A series of deconditioning studies were performed during the 2016 and 2017 shut downs.

Table 2.1. Deconditioning study for TiN

2016			2017		
date	TiN	SS316L	date	TiN	SS316L
Before shut down	1.18	1.35	Before shut down	1.18	1.47
07-29	Beam off		07-01	Beam off	
08-01	1.33	1.51	08-02	1.2	1.39
08-03	1.32	1.60	08-10	1.21	1.41
08-04	1.34	1.60	08-10	Arms retracted	
08-18	1.33	1.61	08-14	1.23	1.43
09-02	1.33	1.61	09-18	1.35	1.58
09-10	Arms retracted		10-14	1.57	1.72
09-19	1.41	1.72	After vacuum vent	1.72	1.87

Table 2.1 shows results from the decondition studies done the two shut downs. During the 2016 shut down, the beam was turned off on Jul 29th, when a quick decondition happened for the first several days. The SEY increased from 1.18 (TiN) and 1.35 (SS316L) to 1.33 (TiN) and 1.60 (SS316L). Then, the SEY stayed relatively constant for a full month. The samples deconditioned further after the arms were retracted to the measurement position, with the SEY increasing to 1.41 and 1.72 for TiN and SS316L respectively. Eventually, for the next round of measurement, the SEY deconditioned to 1.41 and 1.72 for TiN and SS316L. The same happened for the 2017 shut down, the conditioned SEY was preserved when the samples were stored at the beam exposure position. Once the samples were retracted to the measurement position, the SEY started to increase. At the end of the 2017 shut down, before the samples were removed from the station, the samples were exposed to a Nitrogen purge. The purge increased the SEY to 1.72 and 1.87 for TiN and SS316L.

The deconditioning and conditioning processes happens because the material surface becomes more or less contaminated [27, 33]. With the MI generating E-cloud within the beam pipe, the E-cloud cleans the vacuum chamber wall's surface by removing the surface contamination. Due to the surface cleaning process, the

accelerator vacuum chamber's SEY decreases; this is the conditioning process. When samples are stored at the exposure position, samples are in the cleaned MI vacuum chamber. The vacuum pumps are on during the shut downs, so the vacuum are preserved at a good level. With the good vacuum and the cleaned surface, the SEY is well preserved. When the samples are retracted to the measurement position, the samples are surrounded by unclean surfaces. Contamination from the surrounding surface of the unclean arm migrates to the sample surface and deconditions it. The vacuum purge brings even more contamination to the sample surface and increasees the SEY even further.

2.3.2 The Amorphous Carbon coated stainless steel 316L. Figure 2.13 shows the results of the A-Carbon study over the 2018-2019 period of operation. Table 2.2 shows the results of the A-Carbon deconditioning study. During this study period, the samples were exposed for 256 days to 55.9×10^{19} total protons. CERN's A-Carbon study reported an SEY below 1.0 for A-Carbon, which is low enough to completely kill E-cloud generation. An SEY below 1.0 was also observed in these measurements. The SEY for the SS316L sample started at 2.14 and conditioned to 1.25. The SEY for the A-Carbon sample started at 1.26 and conditioned to 0.82. Conditioning for SS316L happened more slowly for the A-Carbon measurement period. This was because the conditioning effect on the MI vacuum chamber surface was preserved over the 5 years of operation. The lower SEY of the MI beam pipe generated less E-cloud thus conditioning the surface more slowly.

Studies show that after sufficient machine operation and conditioning time, the SEY of SS316L will be close to 1.25. Alternatively, for A-Carbon, the SEY starts very low and is conditioned to an SEY below 1.0 after exposure to beam for 100 days or exposure to 30×10^{19} protons. The SEY values found for the SS316L deconditioning process during the latest round of measurements do not show the same trend as shown

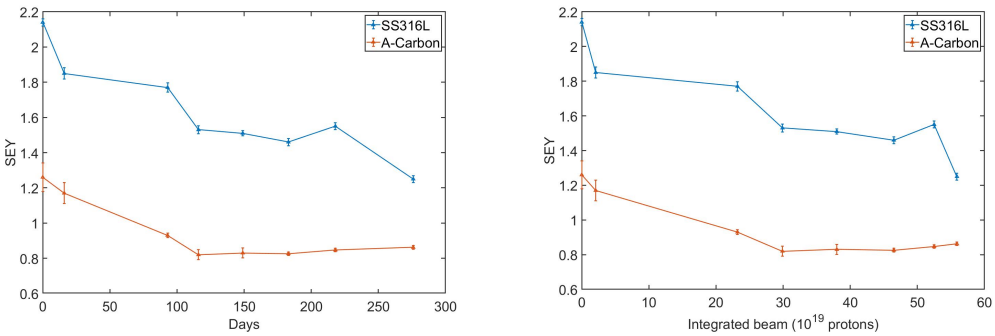

(a) SEY over time (b) SEY over integrated beam intensity

Figure 2.13. A-Carbon and SS316L comparison study.

Table 2.2. Deconditioning study for A-Carbon

2019		
date	A-Carbon	SS316L
Before shutdown	0.82	1.55
07-03	Beam off	
07-25	0.862	1.25
08-08	0.865	1.45
09-10	Arms retracted	
10-03	0.886	1.60
After vacuum vent	0.9868	1.62

previously, the cleaner beam pipe could be the reason. Before the A-Carbon study, the beam pipe had been conditioned for 5 years, especially during the 2017 to 2018 higher intensity operation. The MI operated with 50×10^{12} protons per cycle. The beam pipe surface was well cleaned, which means less E-cloud would be generated and available to further condition the samples. As for the A-Carbon, the conditioned SEY is well preserved at either the exposure or the measurement position. The venting process still causes extra deconditioning. However, even with a purge, the A-Carbon's SEY remained around 1, so E-cloud generation could be completely mitigated with an A-Carbon coating.

2.4 Conclusion

A SEY station is installed to MI-10 area to measure the SEY development for different samples under MI operational conditions. A series of improvements to reduce the leakage current were made to the station.

TiN and A-Carbon are candidate low SEY coatings that were studied with the SS316L as a comparison sample. It was found that for the TiN coating, the SEY started at 2.1, and conditioned to 1.2. The A-Carbon started with an SEY of 1.25 and conditioned to 0.8. The SS316L started with an SEY of 2.2 and conditioned to 1.25. Based on the SEY measurements and the simulation results presented in next chapter, both TiN and A-Carbon are attractive candidates for suppression of E-cloud generation in MI at higher PIP-II intensities (70×10^{12} protons). If the SS316L can be conditioned further with higher beam intensity, it could still potentially suppress the E-cloud generation, but (as will be seen later) the stainless SEY sits at the edge required for stable operation and is a risk at future upgrade intensities. The A-Carbon, the best material studied, starts with an SEY of 1.26, which could potentially suppress the E-cloud generation without much conditioning. With some treatment, the A-Carbon could reach a SEY below 1, which would kill E-cloud generation at all beam intensities. The TiN would require conditioning to reach an SEY of 1.2, which would suppress E-cloud generation for MI based on simulation results presented in the next chapter. However, it was found that it takes on the order of 10^{20} integrated beam intensity for the TiN coated sample to reach an SEY of 1.2 when it starts at a deconditioned state. Under current running conditions, this is on the order of two months of running time. Unless the accelerator vacuum can be maintained during long shut downs, there could be an operational impact during the initial period of a run while the TiN conditions. On the other hand, the TiN sample was produced with a coating rig already developed at Fermilab. The A-Carbon sample was produced by

CERN group. To apply the coatings to the MI, developing an A-Carbon coating rig would be required.

The deconditioning process was studied during the long shutdowns. It was determined from these studies, that for all the materials studied the conditioned SEY should be well preserved in vacuum. Standard venting procedures at Fermilab will not preserve conditioned SEY.

CHAPTER 3

E-CLOUD GENERATION SIMULATION

3.1 Introduction

To understand how E-cloud generation works in an accelerator, the best way is to simulate the process. The simulation codes for E-cloud generation and related problems are of two types; there are E-cloud generation codes (POSINST [38–41], PyECLOUD/ECLOUD [42–46], etc) and E-cloud beam interaction codes (Warp-POSINST [47, 48]). The E-cloud generation codes simulate the process of E-cloud generation based on the accelerator environment. Generally the E-cloud generation codes treat the particle distribution of the beam as a fixed accelerator parameter and do not let the proton distribution evolve due to the field of the electrons in the cloud. The E-cloud beam interaction codes not only simulate the E-cloud generation process, but also any potential change in the proton distribution of the beam due to interactions with the E-cloud. It is more computationally demanding to simulate both E-cloud formation and its interaction with the beam. The E-cloud generation mechanism operates on a bunch-by-bunch time scale (the simulations done here use 400 time steps per bunch passing) while the beam evolution due to the electron cloud happens on a time scale of revolutions or even tens and hundreds of revolutions. There can be up to 5 orders of magnitude of difference in the time scales of E-cloud generation and beam evolution.

It is necessary to simulate the E-cloud generation and beam evolution together to fully understand the E-cloud beam interaction. However, as long as the E-cloud does not significantly perturb the beam or cause any other E-cloud related problems, it is sufficient to study E-cloud build up. The goal is then to mitigate E-cloud related problems by finding strategies to control the build up of electrons, and to make predictions as to when these strategies will not be sufficient to control the electron cloud

density. The E-cloud may be suppressed enough by low SEY coatings or by the SEY conditioning process. E-cloud build up simulations provide important information about what ranges of SEY values and beam parameters become risky to accelerator operation.

This chapter will first present the general logic of the POSINST code. The Particle In Cell (PIC) technique and Furman-Pivi probabilistic model are the main components of the POSINST code. The POSINST simulation input is discussed and simulation results are presented. The E-cloud development over one beam revolution in the MI is examined, and is found to mimic the bunch pattern of the beam. The E-cloud is completely suppressed during an intentional 84 bucket gap in the bunch pattern that is needed for efficient use of the abort kicker. The E-cloud energy distribution and electron incident angle distribution are determined. The energy distribution is important because the SEY coefficient is energy dependent. The angular distribution is important because that impacts how many electrons make it into the E-cloud detector installed in the MI. One interesting phenomenon is that the E-cloud electrons gather around the beam during build up phase in a magnetic dipole field. While not pursued specifically in this work, it is worth noting that the electron densities in a dipole are higher, and so the associated problems may be more acute in these regions.

Studies carried out by S. A. Antipov [3] on an observed RR E-cloud instability found that a certain threshold E-cloud density is required to trigger the development of the instability. The E-cloud linear density must be comparable to the proton beam's linear density. An estimate E-cloud linear density is calculated based on the beam intensity. A series of POSINST simulations were performed for an SEY range of 1.1 to 1.9 and a beam intensity range of 25×10^{12} to 140×10^{12} protons per beam cycle. Based on the SEY and beam intensity scan, a threshold for SEY and beam

intensity is calculated for 10^{10} and 10^{8} electron/m^3 E-cloud density. The 10^{10} and 10^{8} electron/m^3 E-cloud density are 2 and 4 orders of magnitude lower than the estimated E-cloud density that required to caused instability from the RR instability studies.

3.2 POSINST electron cloud build-up code

POSINST is a code that simulates the build-up and dissipation of E-cloud with realistic beam parameters and values for the externally applied magnetic fields [38–41]. The electric fields due to the E-cloud are calculated in POSINST using a Particle In Cell (PIC) technique. These electric fields could be used as an input for codes that simulate beam dynamics, or for analytical calculations (for example the beam instability growth rate due to field from E-cloud). POSINST simulates electron motion in 3D space, but calculates the electric field only for a 2D cross-section of the accelerator. POSINST treats externally applied magnetic fields as a predetermined uniform constant either parallel or perpendicular to the ideal beam trajectory, and thus can only simulate dipole or solenoidal fields. The secondary electron generation calculation is based on the Furman-Pivi probabilistic model [40].

3.2.1 Particle in Cell method. The Particle in Cell (PIC) method was in use as early as 1957 [53]. It provides a computationally efficient way to track the motion of a large quantity of charged particles. POSINST tracks macro-particles representing up to hundreds of electrons rather than tracking every single electron. Since the motion of a charged particle in a given electromagnetic field is determined by the charge-mass ratio, and since a macro-particle has the same charge-mass ratio as an electron, the macro-particle simplification still allows a good simulation of the electron motion. This simplification greatly reduces the computational power needed.

POSINST solves the 2D Poisson equation for a 65×65 mesh grid. For every single mesh grid cell, POSINST locates every macro-particle inside that specific cell

and calculates the charge contained by that cell. POSINST treats the charge distribution inside that cell as uniformly distributed, and solves the Poisson equation for the electric potential. Then, the POSINST will use the difference in electric potential between grid points to calculate the electric field and move the particles accordingly.

3.2.2 Furman-Pivi probabilistic SEY model. The Furman-Pivi probabilistic SEY model is a model developed by M. Furman that simulates the process of secondary electron generation [40]. The model is used to generate an SEY curve, and it is the basis for the generation of secondary electrons when POSINST tracks electron-wall collisions. As a requirement of the secondary electron generation process, the Furman-Pivi-model conserves energy and momentum. The model assumes that when an electron strikes the vacuum chamber surface, there are three possible processes, 1) elastic collision, 2) re-diffusion and 3) generation of true secondary electrons. The elastic collision electrons are electrons that elastically bounce back from the material surface. These electron will have the same kinetic energy before and after the collision. The re-diffused electrons are electrons that bounce back from the material surface inelastically. These electrons lose some kinetic energy. The true secondary electrons are electrons that are knocked off the material surface.

Even though the Furman-Pivi model simulates secondary emission based on these three processes, their relative contributions are unknown. All the input parameters used to generate the SEY curve are chosen to fit the model with experimental measurement data (SEY, incident angle dependency [27] and secondary electron emission energy spectrum [32]) and to conserve energy and momentum for the secondary electron emission process. The model provides equations to calculate an 'emission' curve for all three process, The 'emission' curves of all three process are added up to produce the SEY curve. Figure 3.1 shows an SEY curve fit from the Furman-Pivi-Model.

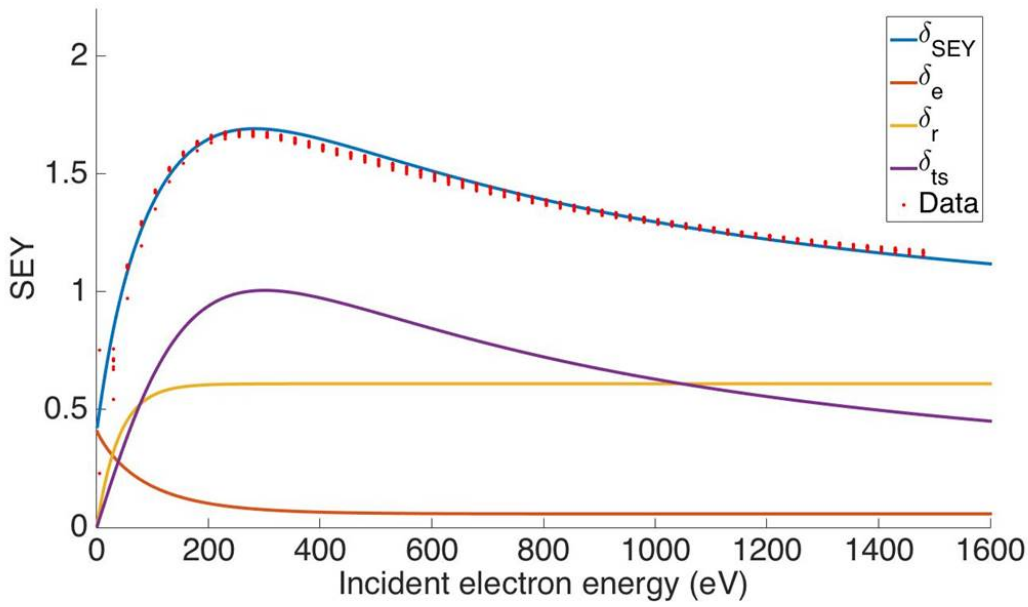

Figure 3.1. The Furman-Pivi-model fitted to measured SEY.

In figure 3.1, δ_e, δ_r and δ_{ts} are defined as $\delta_e = I_e/I_0$, $\delta_r = I_r/I_0$ and $\delta_{ts} = I_{ts}/I_0$ respectively. Where I_e is the elastic electron current; I_r is the re-diffused electron current; I_{ts} is the true secondary electron current and I_0 is the incident electron current. δ_{SEY} is the total SEY curve that is defined as $\delta_{SEY} = \delta_e + \delta_r + \delta_{ts}$. The red dots are measured SEY data for stainless steel 316L. The equations and parameters used to calculate δ_e,δ_r and δ_{ts} are given in the Furman-Pivi-model paper [40], where Furman generated all the parameters used to fit his model to unconditioned stainless steel's SEY (2.05 peak SEY). Once the SEY curve is generated, the POSINST code will generate a probability distribution function for secondary electrons based on the SEY curve. The secondary electrons will be generated based on the probability distribution function.

Furman only fit his model to 2.05 peak SEY for stainless steel in his paper, in figure 3.1, the peak SEY is around 1.6. The SEY curve has to be calculated for each different SEY. In order to keep the role of the SEY comparable across simulation

results, rather than fiddle with all the parameters in Furman-Pivi-model, the SEY curve is simply scaled based on the peak SEY value. The SEY curve is scaled based on the following equation:

$$\delta_{scaled} = \delta_{2.05} \frac{SEY_{peak}}{2.05} \tag{3.1}$$

Here δ_{scaled} is the scaled SEY curve, SEY_{peak} is the desired SEY peak SEY, and $\delta(2.05)$ is the original 2.05 peak SEY curve that Furman generated. (For an example, see figure 3.1 showing a scaled curve with $\delta = \delta(2.05) \times 1.6/2.05$.) Some SEY curves used in simulation (1.2 to 1.9 SEY) are shown in figure 3.2.

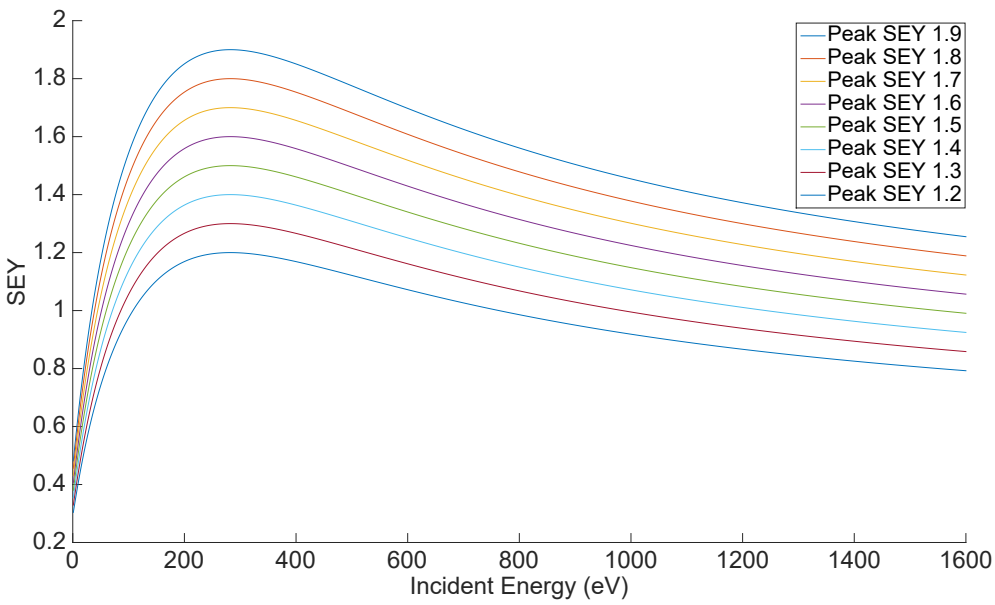

Figure 3.2. The SEY curves used in simulation.

3.2.3 POSINST tracking procedure. With the PIC method, the Furman-Pivi-model and other accelerator parameters in hand, POSINST's initialization procedure and tracking procedures may be completed. All the accelerator related input parameters for POSINST are give in table 3.1, except for details about the beam filling pattern. The beam filling pattern will be discussed in next section. The POSINST

code only tracks the E-cloud generation, treating the beam itself as a predetermined parameter. Once given the user specified the beam parameters, POSINST slices the beam into time steps based on the longitudinal beam distribution. For every time step, the electrons are moved by the electric field due to the rest of the E-cloud, and by kicks from the beam.

Once all the input is provided, POSINST initializes the tracking process by calculating the following items:

1. Slice the beam into time steps based on the time step size and beam particle distribution, calculate the kicks from each slice.
2. Generate the SEY curve based on the SEY related input parameters.
3. Generate initial electrons based on input parameters such as temperature and pressure.

Once POSINST is initialized, the E-cloud is developed for every time step with the following procedure:

1. Solve the electric field based on the electron distribution.
2. Move electrons based on the solved electric field and the beam kicks.
3. Identify all the electrons that collide with the vacuum chamber.
4. Generate secondary electrons based on the SEY curve, incident angle and incident energy.

Table 3.1. Simulation Inputs Parameters

general parameters	
Beam energy [GeV]	8-120
Bunch Intensity [protons/bunch]	5.5×10^{10} - 11.5×10^{10}
Total Intensity [protons]	27.1×10^{13} - 54.1×10^{13}
ring circumference[m]	3319.419
revolution frequency [kHz]	90
revolution period [μs]	11
Harmonic number	588
RF frequency [Mhz]	53
Total RF bucket filled	492
Vacuum pressure [Torr]	2×10^{-8}
Temperature [K]	300
SEY	1.1-1.9
MI specific parameters	
Beam energy [GeV]	25
σ_x [mm]	3
σ_y [mm]	3
σ_z [m]	0.3
σ_t [ns]	1
Bunch length [σ][m][ns]	10; 3; 10
Ellipse chamber major/minor semi-axis [cm]	5.88; 2.39
Round chamber radius [cm]	7.2
Dipole Field[T]	0.234
RR specific parameters	
σ_x [mm]	3.6
σ_y [mm]	1.6
σ_z [m]	0.75
σ_t [ns]	2.5
Bunch length [σ][m][ns]	4; 3; 10
Ellipse chamber major/minor semi-axis [cm]	4.7 2.2
Dipole Field[T]	0.234

3.3 POSINST simulation results

A POSINST simulation can output a variety of useful information about the E-cloud generation process. Parametric studies with POSINST can be used to generate estimates about thresholds when E-cloud generation will be problematic.

3.3.1 General POSINT outputs. The total E-cloud density inside the vacuum chamber generally behaves as shown in Figure 3.3. This figure shows the E-cloud density at a single location in the RR building up on the time scale of one revolution (turn) when there are 5.5×10^{10} protons per bunch. The simulation parameters are given in Table 3.1 The E-cloud density generally reflects the bucket filling pattern. The full revolution period and the RF frequency allow for consist of 588 RF buckets; the 588 RF buckets are grouped into 7 batches of 84 buckets each. Six batches have beam in them, while the seventh batch is empty. Each batch with beam has 82 filled buckets and 2 empty buckets. The 2 bucket gap between batches are reflected by the large dip in the E-cloud density, the E-cloud extinguishes completely during the one batch gap. Since for MI and RR the one batch gap is large enough to reset the E-cloud in a local area of the accelerator, simulating one turn is usually sufficient.

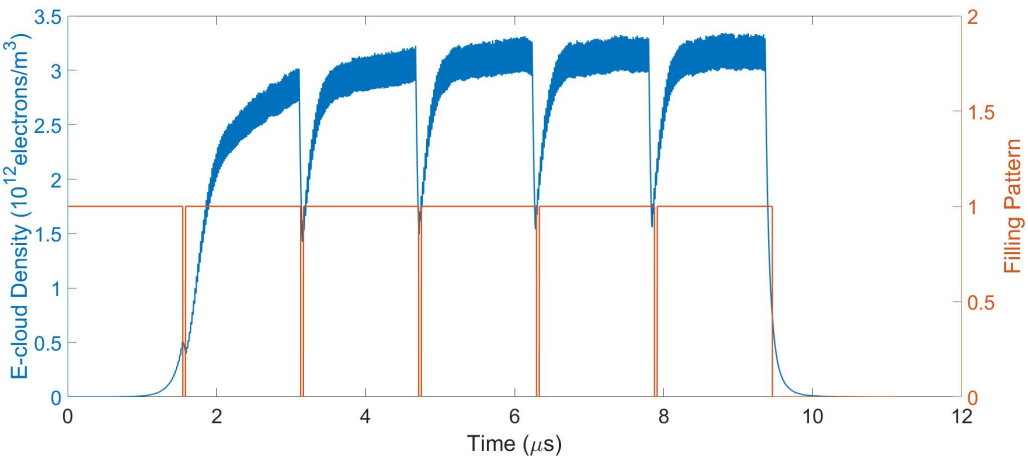

Figure 3.3. Total E-cloud density at a single location in the RR dipole region with 5.5×10^{10} protons per bunch, total of 29×10^{12} protons. When filling pattern is 0, there is no beam in bucket, when filling pattern is 1, there is beam in bucket.

The E-cloud takes time to build up and eventually reaches saturation. The saturation happens when E-cloud's own space charge field cancels out the electromagnetic force from the beam. In term of the E-cloud density, the E-cloud saturates to some density plateau. In figure 3.3, the saturation happens around 4μs into the turn.

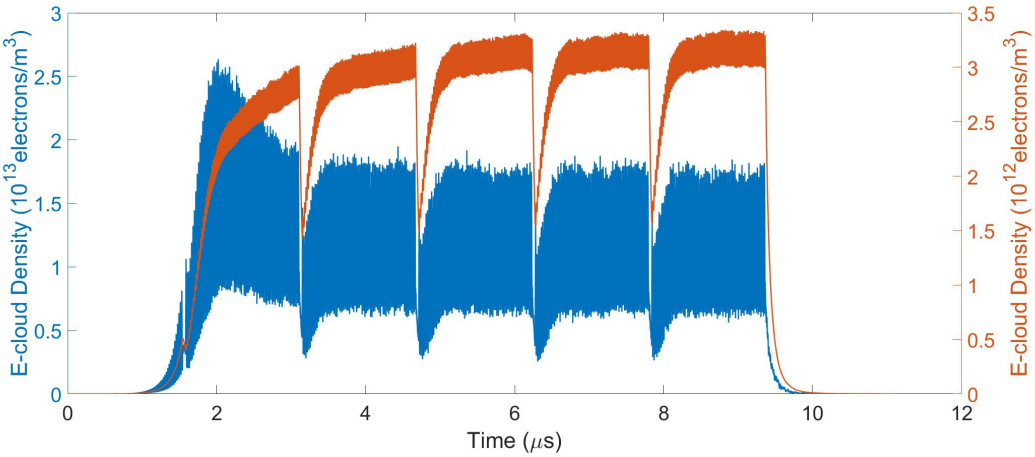

Figure 3.4. E-cloud density within one sigma region of the proton beam compared to the E-cloud density within vacuum chamber. The orange line is the E-cloud density inside the vacuum chamber, the blue curve is the E-cloud density with in the one sigma region of the proton beam.

The characteristics of an electron cloud are influenced by whether or not there is a magnetic field present. In a dipole magnet region, where a net vertical external magnetic field is applied, cloud electrons are trapped by the field, rather than moving in straight trajectories to the beam pipe walls. The E-cloud density is much higher around the beam. As shown in figure 3.4, the E-cloud density around the beam is one order of magnitude higher than the averaged E-cloud density within the vacuum chamber. The E-cloud density development is also different, as figure 3.4 shows, the local electron density around the beam reaches its maximum density during the E-cloud build up phase, dropping to a lower density after the initial saturation is reached. The local E-cloud density was calculated by including only the electrons in the region of an ellipse in the "one-sigma-region" of the proton beam. This phe-

nomenon indicates that beam can be potentially affected more by the E-cloud in the build-up phase than when the density of electrons in the entire beam pipe reaches saturation.

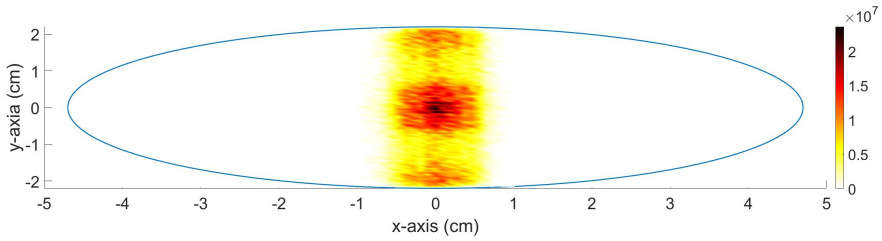

(a) 2μs into the simulation, 1.03×10^{10} electrons presented

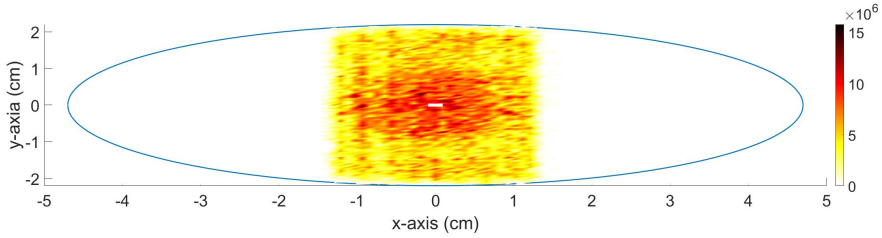

(b) 5μs into the simulation, 1.46×10^{10} electrons

Figure 3.5. E-cloud distribution within the vacuum chamber cross section at specific time. The blue line is the vacuum chamber. Beam located at the center of the vacuum chamber. X and y axis are position relative to the vacuum chamber center, color scale is electron counts.

This phenomenon happens in a dipole magnet region because electrons are confined by its magnetic field. Simulations show that the electrons gather around the beam over the build-up process. After the E-cloud saturates, the electrons are pushed to occupy more space because of the space charge force between electrons. Figure 3.5 shows the E-cloud distribution comparison between 2 μs and 5 μs into the simulation. The 2 μs (figure 3.5(a)) is where the E-cloud density with in the "one-sigma-region"

reach maximum in figure 3.4. The 5 μs (figure 3.5(b)) is where E-cloud saturates to a steady level in figure 3.4. Between the two points, the electron counts increased about 40%, the space electrons occupied almost doubled in figure 3.5.

There are many other features about the E-cloud that can be generated by POSINST, such as bombardment rate: the amount electron that hit the vacuum chamber over every time step, E-cloud average energy: the electrons average kinetic energy for every time step, E-cloud energy deposition: the energy E-cloud deposited into the vacuum chamber every time step. Examples of such feature are shown in figure 3.6.

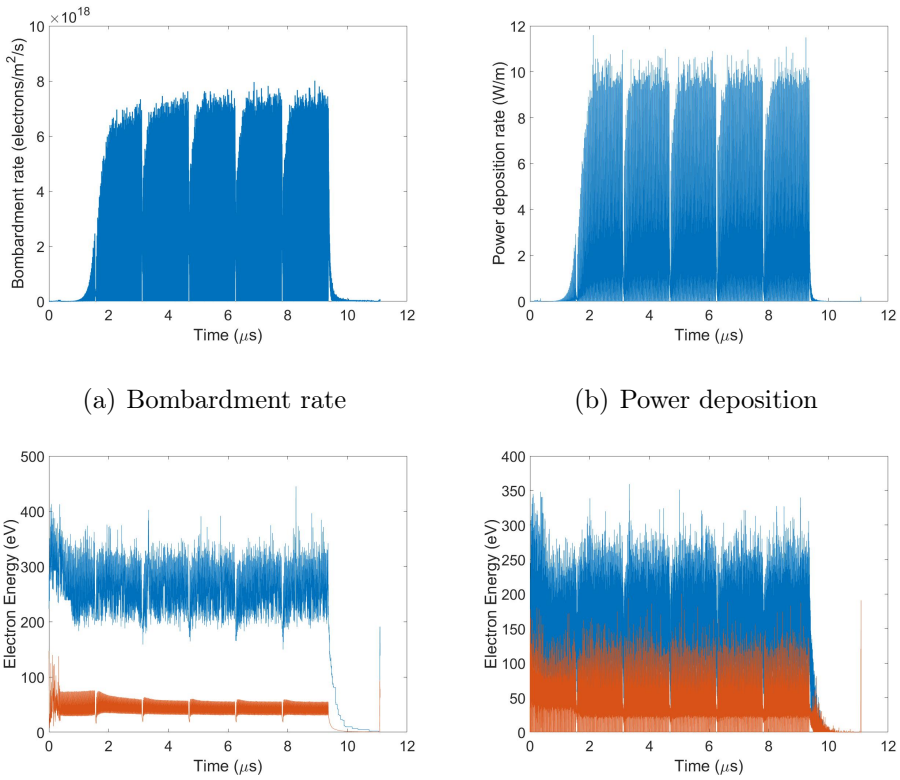

(a) Bombardment rate

(b) Power deposition

(c) Average and maximum electron energy

(d) Average and maximum wall collision energy

Figure 3.6. Some other POSINST outputs.

Figure 3.6(a) shows the average bombardment rate over one turn. The bom-

bardment rate follows the trend of E-cloud density as expected. The more E-cloud, the more electron will hit the vacuum chamber. The bombardment rate is a quantity that can be measured. The study of measuring and comparing bombardment rate will be demonstrated in the next chapter. Figure 3.6(b) shows the E-cloud power deposition rate on the beam pipe. The power deposition on the beam pipe is the heat deposition on the beam pipe. For an accelerator with super conducting magnets, the heat deposition on magnets could be problematic. Figure 3.6(c) shows the average and maximum energy of all electrons over one turn. The average electron energy is around 60 eV, the maximum electron energy is around 300 eV. The average electron energy decreases a little bit as the E-cloud saturates. Figure 3.6(d) shows the average and maximum wall collision energy.

3.3.1.1 Incident angle and energy distribution. POSINST can output the E-cloud distribution for specific times steps. Figure 3.5 gives an overall E-cloud distribution inside the beam pipe for specific time steps. The POSINST code can also output E-cloud wall collision related information. Figure 3.3.1.1 shows the incident angle and energy distribution for wall collisions over a full simulation. The simulation here is in a MI field-free region with a round beam pipe. The beam intensity is 50×10^{12} protons, the SEY is 1.3. From the energy distribution, the majority of the wall collisions happen with collision energy less than 400 eV. From the collision angle distribution, a majority of electrons hit the vacuum chamber with an incident angle less than 20°. In fact, about 50% of the electrons hit the vacuum chamber with less than 18° incident angle. The incident angle distribution results are used in the next chapter to calibrate the E-cloud measurement device. Also in the next chapter, the simulated energy distribution is compared to the measured energy distribution of the E-cloud electrons.

3.3.2 Comparison to M. Furman's simulation results. M. Furman, the author

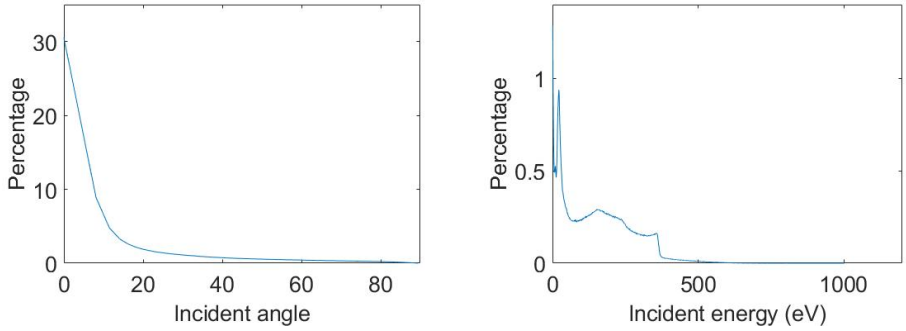

(a) Angle distribution (b) Energy distribution

Figure 3.7. Incident angle and energy distribution for wall collision over the full simulation.

of POSINST, simulated the dependency of E-cloud generation on beam intensity for the MI [49]. This result was reproduced with the POSINST code as a check that the simulation was being used correctly (see figure 3.8) before launching detailed simulation studies for the thesis research. Both simulations used an SEY value of 1.3, the E-cloud density dependence on the MI beam intensity was reproduced for the 588 harmonic number case. Furman did a study to compare E-cloud production for the normal 53 MHz (h=588) RF frequency and for a hypothetical RF frequency 4×53 MHz $= 212$ MHz (h=2352). The new simulation faithfully reproduced the same features as Furman's 53 Mhz case. The E-cloud density for each beam intensity is the average over the full turn.

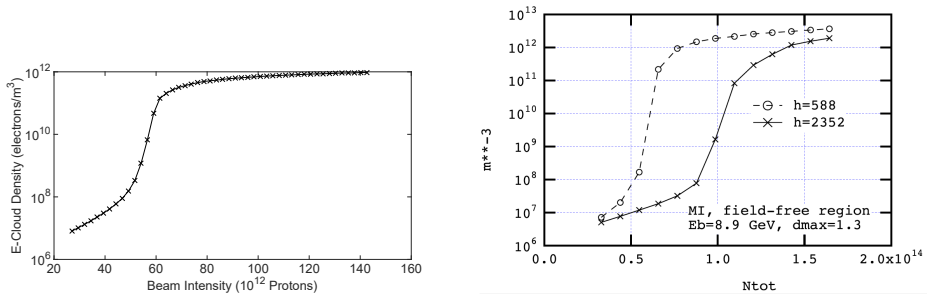

(a) Simulation (b) M. Furman's result

Figure 3.8. The comparison between M. Furman's result and my simulation.

3.3.3 Threshold simulation. Ideally, to mitigate E-cloud related problems, suppressing E-cloud generation with low SEY would be a very good strategy. However, E-cloud increases with increasing beam intensity, as verified by simulation. (See figure 3.8.) So, an SEY value that is acceptable for current operations may not be sufficiently low in the future. Increasing the beam intensity is a major improvement goal for the MI. The improvement plans [15, 54, 55] for accelerators typically aim at increasing beam intensity. So, it is useful to explore the dependence of E-cloud generation on combinations SEY and beam intensity.

In order to interpret the results of parametric studies on the dependence of E-cloud generation on SEY and beam intensity, it is helpful to know approximately what level of E-cloud is dangerous to operations. Previous studies found that development of E-cloud induced instabilities in the RR occurs when the E-cloud and the beam have comparable average linear charge density [3]. Even though this is just a rule of thumb estimation, it is useful as a benchmark E-cloud density threshold above which E-cloud will likely be problematic. As shown in later studies, from saturation to non-saturation, the E-cloud density can have changes up to 5 orders of magnitude. With low enough SEY (a safe operation SEY), E-cloud generation can be suppressed 2 orders of magnitude away from the E-cloud density that will be problematic. By simulating E-cloud dependency on SEY and beam intensity, the safe operation SEY for current and future beam intensity can be estimated. With the safe SEY decided and the SEY measurement results, weather or not a coating will be sufficient to deal with the E-cloud problem for the MI and RR can be determined.

Based one the rule of thumb that the E-cloud have to have comparable linear charge density with the beam to cause instabilities, one can identify some important threshold. Currently, the MI and RR beam intensity is from 5×10^{10} to 11×10^{10} protons per bunch. An increase in intensity to 13×10^{10} protons per bunch is planned

for the PIP-II accelerator complex upgrade. The bucket length for MI and RR is equal to the circumference of the ring divided by the number of buckets $C_{ring}/N_b = 3319.419$ m/588=5.65 m. So the average linear density of protons in the RR and MI is on the order of 10^{10} protons per meter. The simulation produces the volume charge density of the E-cloud. Dividing it by the cross-sectional area of the beampipe will convert it to a linear charge density. The cross sectional area of the round beam pipe for MI is 0.0163 m^2, while the cross sectional area of the elliptical pipe is 0.0044 m^2. The cross sectional area of the RR beampipe is 0.0032 m^2. In order for the E-cloud to have a linear density comparable with the proton beam (10^{10} electrons/m), the E-cloud density within beam pipe would have to be on the order of 10^{12} to 10^{13} electrons/m^3. Figure 3.3 shows an example case where the E-cloud has a comparable linear charge density to the beam. As shown in the figure, the E-cloud electron density is about 3×10^{12} electrons/m^3. The average linear proton density of the beam inside beam pipe is about 5.5×10^{10} protons /5.65m = 0.9735×10^{10} protons/m. The average linear density of the E-cloud for the full beam pipe is 3×10^{12}electrons/m^3 $\times$ 0.0032m^2=0.96×10^{10} electrons/m (RR beam pipe, 0.0032 m^2). The linear particle densities of the proton beam and the saturated E-cloud are close in this case (0.9735×10^{10} protons/m and 0.96×10^{10} electrons/m).

Based on a prior RR instability study [3], and the estimated average linear particle density for the beam, in order for the E-cloud to cause an instability, the E-cloud density would need to be on the order of to 10^{13} electrons/m^3 (so that the E-cloud and beam have comparable linear charge density). A series of simulations with different beam intensities and SEY values were done to find out what parameters will lead to E-cloud densities at the 10^{11} to 10^{13} electrons/m^3 level. Figure 3.9 shows simulation results for MI and RR E-cloud densities in field and field-free regions of the accelerator for different SEY and intensity values. For MI the SEY range is 1.0 to 1.9, and the intensity range is 25×10^{12} to 146×10^{12} protons per acceleration cycle.

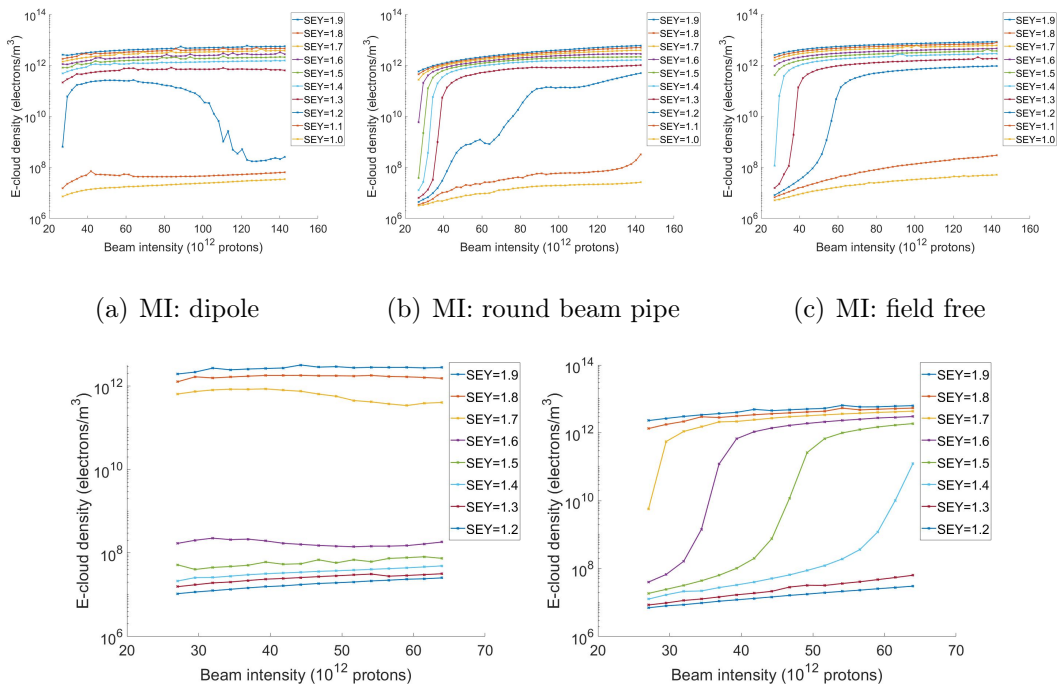

(a) MI: dipole (b) MI: round beam pipe (c) MI: field free

(d) RR: dipole (e) RR: field free

Figure 3.9. Dependence of average E-cloud density over one full turn on beam intensity for different SEY values. The subfigures show this dependence for different regions of the MI and RR. The round beam pipe region for MI is on field free region. The MI dipole and MI field region share the same elliptical beam pipe. The RR field free and dipole region share the same elliptical beam pipe.

For RR the SEY range is 1.2 to 1.9, and the intensity range is 25×10^{12} to 65×10^{12} protons acceleration cycle. The scan covers a field free region and a dipole region, for MI an extra round beam pipe field free region is included. The E-cloud density for each SEY and beam intensity combination is calculated based on averaging over the full revolution, the abort gap is included in the averaging process, so the averaged E-cloud density is lower than the saturated E-cloud density (in figure 3.3, the saturated E-cloud density is 3×10^{12} electrons/m^3, the averaged E-cloud density is 4.91×10^{11} electrons/m^3). The averaged E-cloud density is potentially 5 to 10 times smaller than the saturated (peak) E-cloud density, which means that the averaged E-cloud linear charge density could be 5 to 10 times smaller than the beam's linear charge density, and still be near the instability threshold.

As can be seen in Figure 3.9, the E-cloud build up saturates when the E-cloud and beam have comparable linear charge densities (this is when the volume charge density of E-cloud is in the range from 10^{11} electrons/m^3 to 10^{13} electrons/m^3). Note that for the purposes of this discussion the linear charge density of the E-cloud was calculated over the pipe cross-section, which is much larger than the beam; however, in the dipole regions the majority of electrons are trapped near the beam. This is consistent with results of the prior RR instability study, that indicated that the RR instability happened in the 'dipole' region [3]. The process of saturation will be more thoroughly studied in the next chapter.

When the SEY and beam intensity are low enough, the E-cloud density can be 5 orders of magnitude lower than the saturated density. The E-cloud density is very sensitive to the SEY and beam intensity. Low E-cloud generation and high intensity can be achieved with low enough SEY. According to figure 3.9, when the SEY in the Main Injector is below 1.1, E-cloud generation is stopped for up to 146×10^{12} protons per acceleration cycle beam intensity. For RR, 1.6 SEY would stop E-cloud generation for dipole regions, and 1.3 for field free regions. One reason the dipoles might tolerate a higher SEY is that the fields trapping the electrons prevent them from hitting the beampipe walls.

Linear extrapolations between the SEY and intensity grid of simulation results may be used to create contour lines of E-cloud density for different SEY and beam intensity values. In this way, one can calculate different threshold lines for select E-cloud densities. Figure 3.10 shows contour plots for both MI and RR for 10^8, 10^{10} and 10^{12} electrons/m^3 E-cloud density. The estimated average E-cloud density where an instability could occur at present beam intensities is 10^{12} electrons/m^3. (The saturated E-cloud density can reach 10^{13} electrons/m^3, however the contour plot is based on averaged E-cloud density over the full turn. The averaged E-cloud density

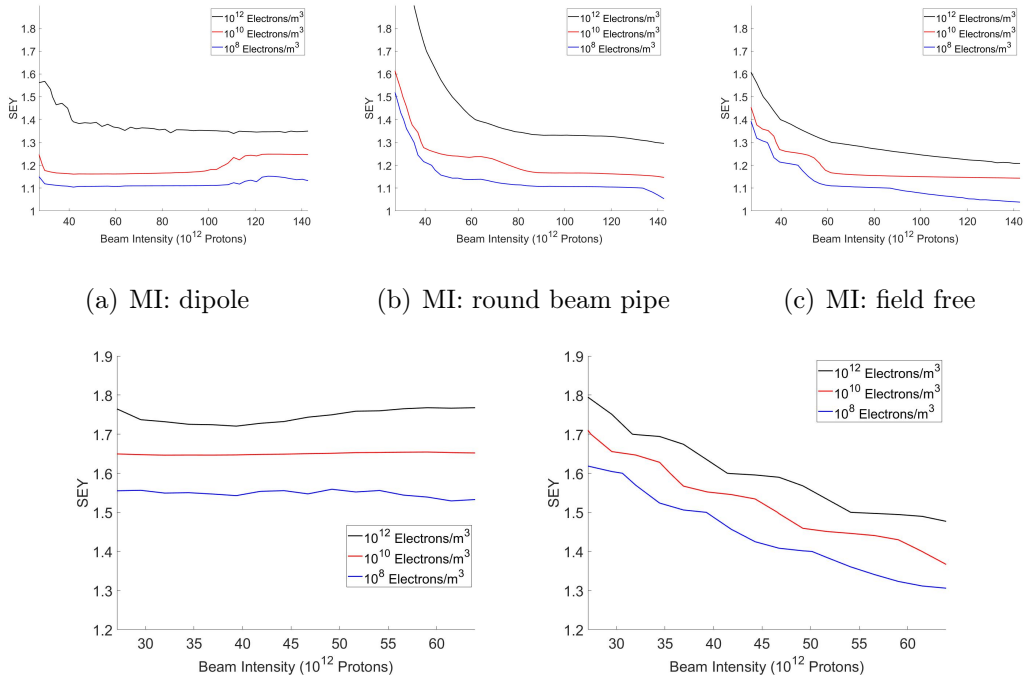

(a) MI: dipole (b) MI: round beam pipe (c) MI: field free

(d) RR: dipole (e) RR: field free

Figure 3.10. The SEY and beam intensity contour plots for different E-cloud densities. Each line represents sets of (Beam intensity, SEY) points that are at the threshold of the E-cloud density represented by that line. So, any Beam intensity, SEY value above the line will have at least the E-cloud density value represented by that line. In order to have an E-cloud density less that the one represented by a line, the (Beam intensity, SEY) values in the accelerator must fall below that line.

is 5 to 10 times smaller than the saturated E-cloud density. So 10^{12} electrons/m^3 is a good threshold.) E-cloud average densities of 10^8 and 10^{10} electrons/m^3 are 4 and 2 orders of magnitudes lower; at these low densities potential E-cloud related problems will be suppressed.

Figure 3.11 shows the E-cloud density dependence on SEY at PIP-II intensity for three different regions in the accelerator; a region with a dipole field and field free regions in an elliptical and round beam pipe. As can be seen from the plot, the E-cloud density for 1.1 SEY is below 10^8 electron/m^3 while for 1.2 SEY, the E-cloud density almost reached 10^{12} electron/m^3 for a field free region with an elliptical beam pipe and for a dipole region. When the SEY increased from 1.1 to 1.2, the E-cloud

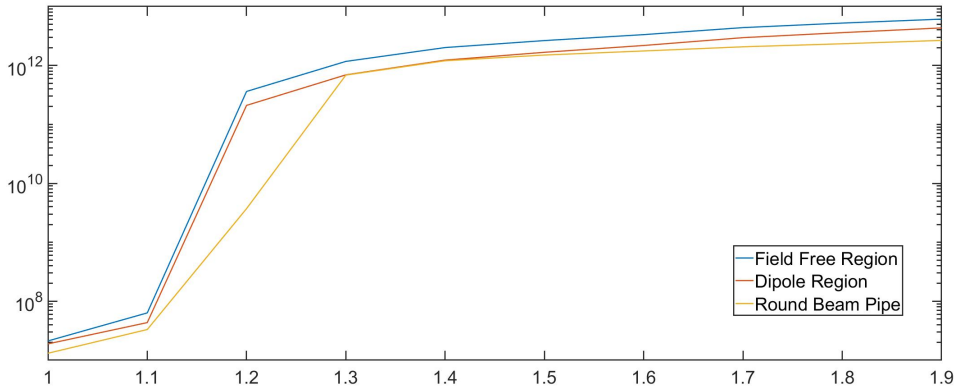

Figure 3.11. The E-cloud density dependence on SEY for PIP-II beam intensity (70×10^{12} protons).

density almost increased by 4 orders of magnitude. The E-cloud build up reaches saturation at an E-cloud density of 10^{12} (here E-cloud and beam have comparable linear density). The 10^{12} E-cloud density indicates where the E-cloud is expected to be problematic. The 10^{8} E-cloud density is where the E-cloud generation process is completely suppressed, because the secondary emission process is completely shut off. The 10^{10} E-cloud density is in between the two situations. When the E-cloud density is on the order of 10^{10} electron/m^3, it is very sensitive to all input parameters. In this E-cloud density regime, the E-cloud generation dependencies on all related parameters are exponential; however, this is a very small regime. Despite the fact that at 10^{10} the E-cloud density shows an exponential rise, because this happens over such a small range of SEY values, E-cloud generation can be suppressed by a small decrease in SEY. The 10^{10} E-cloud density threshold thus provides a good indication of SEY values where the suppression of E-cloud generation starts.

Examination of figure 3.10 shows that 1.5 SEY in a RR dipole region will suppress the E-cloud density to below 10^{8} electrons/m^3; and 1.4 SEY can suppress E-cloud generation in field free region to below 10^{8} electrons/m^3 up to around 55×10^{12} proton intensity. It is much harder to suppress E-cloud generation in the MI. In a

dipole region, an SEY of 1.18 is needed to suppress E-cloud generation to below 10^{10} electrons/m^3. In a field-free region, an SEY below 1.2 is needed to suppress E-cloud generation to below 10^{10} electrons/m^3. However, when the beam intensity is below 70×10^{12} protons, a 1.2 SEY will be enough to suppress the E-cloud generation to 10^{10} electrons/m^3.

One major cause of the difference in E-cloud generation threshold between the RR and MI is the beam bunch length. Referring to Table 3.1, the bunch length, σ_t, of MI is 1 ns, while the σ_t of RR is 2.5 ns. Longer bunch lengths can greatly suppress E-cloud generation. More bunch length related studies will be presented in the next chapter.

Using the beam intensity for future Fermilab upgrades, the average linear charge density of the proton beam can be estimated. Requiring that the linear charge density of the E-cloud be comparable to the beam, the related E-cloud volume charge density may be calculated. Taking this as the maximum allowable E-cloud density, the SEY that would produce this intensity can be obtained from simulation. This is a 'threshold SEY', such that a higher SEY will be in a 'danger' region of E-cloud density, where E-cloud could cause instabilities. This is called the danger SEY in table 3.2. Since the E-cloud density is an average over the full revolution, which includes the abort gap, 10^{12} electrons/m^3 is used as the threshold for determining whether or not E-cloud could cause an instability. A 'safe operation' SEY is also extracted from figure 3.10 for 10^{10} electrons/m^3. For the 1.2MW PIP-II beam intensity (70×10^{12} protons), 1.17 SEY is likely to suppress E-cloud generation for all regions to 10^{10} electrons/m^3. For the RR, 1.3 SEY would likely suppress E-cloud to 10^8 electron/m^3 density in all regions.

Table 3.2. Beam intensity for each stage of the MI, corresponding E-cloud density and SEY threshold

	Before PIP-I	PIP-I	Current upgrade	PIP-II
Beam power	400kW	700kW	900kW	1.2MW
Beam intensity (protons)	24×10^{12}	50×10^{12}	55×10^{12}	70×10^{12}
Beam Linear charge intensity (protons/m)	0.86×10^{10}	1.8×10^{10}	2×10^{10}	2.5×10^{10}
E-cloud Density Comparable to Beam (electrons/m^3)	1.95×10^{12}	4.1×10^{12}	4.5×10^{12}	5.7×10^{12}
SEY threshold danger to instability (10^{12} electrons/m^3, 4.4×10^9 electrons/m)				
Field Free region Elliptical beam pipe	1.45	1.24	1.24	1.17
Field Free region Round beam pipe	1.61	1.24	1.24	1.23
Dipole region	1.57	1.39	1.39	1.37
Safe operation SEY threshold (10^{10} electrons/m^3, 4.4×10^7 electrons/m)				
Field Free region Elliptical beam pipe	1.45	1.24	1.24	1.17
Field Free region Round beam pipe	1.61	1.24	1.24	1.23
Dipole region	1.25	1.17	1.17	1.17

3.4 Chapter conclusion

This chapter described the POSINST simulation code. POSINST solves for the electric field from the electron distribution, and evolves the electron distibution using a PIC method. The POSINST code models the secondary electron emission process with the Furman-Pivi-model. The code outputs E-cloud density, bombardment rate and also has the capability to give specific E-cloud distributions. The incident E-cloud energy and incident angle distribution are calculated for MI. The incident angle distribution is used to estimate the conversion of the RFA signal to E-cloud bombardment rate in the next chapter. The simulation of the incident energy distribution is favorably compared to a measurement in the next chapter. A POSINST simulation of the E-cloud density dependence on beam intensity is compared with an early result from M.A. Furman. The POSINST simulation done for this purpose agrees well with M.A. Furman's simulation.

Simulations of E-cloud show that the build up of E-cloud mimics the bunch pattern in the ring, and that it dies away during the abort gap (an empty string of buckets in the fill pattern). Since the E-cloud is 're-set' each beam revolution (turn), it may be studied on a turn-to-turn basis. Its character depends on parameters such as the beam intensity and bunch length, but E-cloud is not dependent on history stretching back further than a revolution.

A result from Sergey A. Antipov's study on a RR instability [3], is that in order for the RR instability to happen, the E-cloud must have a comparable linear density with the beam. This result was used as the basis for estimations of safe SEY values for a range of intensities at otherwise current operating parameters. At present beam intensities, the average E-cloud density over a full revolution would have to be on the order of 10^{12} electrons/m^3 to be comparable to the average proton density. Using this rough estimation scheme, the SEY thresholds at various beam intensities

were studied for the MI and RR. Some E-cloud densities and SEY threshold estimates for future MI upgrade intensities were presented in Table 3.2. For these studies, a 10^8 and 10^{10} electrons/m^3 E-cloud density threshold for MI and RR were also calculated. These lower thresholds correspond to an E-cloud density that is 4 and 2 orders of magnitude below the E-cloud density required to cause a RR instability. With such low E-cloud densities, the majority of E-cloud related problems could be suppressed.

CHAPTER 4
ELECTRON CLOUD MEASUREMENTS

4.1 Introduction

E-cloud is observed in the Main Injector [2, 56], and may be a problem in the future due to planned increases in beam intensity [15]. While E-cloud is not causing instabilities or other operational problems in the Main Injector at this time, the E-cloud is already present in the Main Injector. It provides an opportunity to study the build-up process of the E-cloud and bench mark simulation codes that simulate such processes.

There are many techniques to directly or indirectly measure E-cloud build up and related effects. One can monitor the beam behavior to indirectly understand the impact of E-cloud. However, it is useful to implement one of the several techniques available to measure E-cloud directly. A Retarding Field Analyzer (RFA) [57] is a device that collects electrons incident on the vacuum chamber wall of the accelerator. The RFA will generate a signal that measures the E-cloud bombardment rate at the collector. Simulation results can be directly compared to the electron cloud build-up process, and parametric comparisons made between the RFA data and simulations.

The SEY test stand located at MI-10 provides local SEY information, so this is also one of the better places to install an RFA for E-cloud measurements. The SEY value is a needed input for the E-cloud simulations, and the electron cloud density (obtained from the RFA) is an output parameter of the simulation. These two co-located instruments enable comparison of simulation results to experimental measurements for a field free region of the accelerator.

A series of studies of the E-cloud build-up were performed. The SEY of the beampipe material influences how many secondary electrons are liberated from the

material into the vacuum chamber where these electrons may potentially affect the proton beam. The SEY is not the only factor impacting the electron cloud density; E-cloud production also depends on the properties of the proton beam such as the intensity, the bunch length and the filling pattern. The beam intensity and bunch length both affect the particle density of the proton beam. The filling pattern describes the large scale proton density modulation with time. The electron cloud tends to die away when there are significant gaps (empty buckets) in the proton density profile. A series of studies were performed to better quantify the influence of these beam parameters. Measurments were done using the RFA, and data compared to simulation results.

This chapter begins with a description of the RFA detector, and interpretation of the signal. A comparison of the measured and simulated energy distribution of the electrons in the E-cloud is presented. Beam studies providing information on the electron cloud dependence on beam intensity, and bunch length were carried out and are compared to simulation results. For the E-cloud versus beam intensity study, the MI intensity covered the range from 20×10^{12} to 50×10^{12} protons, and it was found that only when the beam intensity reached 46×10^{12} was there significant E-cloud generation. When there is a detectable E-cloud, several prominant features can be observed. The E-cloud dies away every revolution during the abort gap, which is 1/7 of the revolution period. The E-cloud density spikes up and down at transition, and then grows over the rest of the acceleration cycle. The transition energy occurs when there is a loss of longitudinal focusing, which is when the particle transit time around the ring does not depend on its momentum error.

In order to better study the E-cloud dependence on the bunch length, it must be known how it changes over the acceleration cycle. Although there is instrumentation (the wall current monitor) to measure the bunch length, it does not now have

the capability to track bunch length over the entire cycle. The bunch length over the cycle is reconstructed using a combination of wall current measurments and simulation results provided by R. Ainsworth obtained using the BlonD [58] code. Once information about the bunch length over the cycle is available, it is possible to use as an input for the POSINST code to more accurately simulate the E-cloud density over the cycle. Matching the simulation inputs to machine parameters as closely as possible, POSINST simulations of E-cloud density are compared with beam measurements of E-cloud. The way that the E-cloud density changes with bunch length for the shorter bunch lengths after transition is very sensitive to the beam intensity and the SEY. Although the absolute numerical value of the E-cloud bombardment rate from simulation does not match the estimated E-cloud bombardment rate at the RFA, using the beam intensity and measured SEY as inputs to the simulation, the detailed evolution of the E-cloud density over the acceleration cycle is reproduced accurately. Since the E-cloud evolution is very sensitive to the input parameters, it can be concluded that simulation results may be extrapolated to other machine parameter regimes with confidence.

4.2 The RFA set-up

The specific RFA used at the MI-10 area is the same as the RFA used in Michael Backfish's thesis [2], it is a copper collector cup with a metal grid on top. As electrons enter the collector cup a current signal proportional to the E-cloud bombardment is generated. Figure 4.1 shows the RFA, and a schematic of the RFA. The screen is electrically isolated from the collector cup. By applying a negative bias voltage on the grid, electrons that pass the grid will be forced into the collector and all secondary electrons that are generated inside the collector cup will be recaptured. The grid also stops electrons below the grid bias voltage from entering the collector. By controlling the grid bias voltage, the RFA can be used to measure the E-cloud

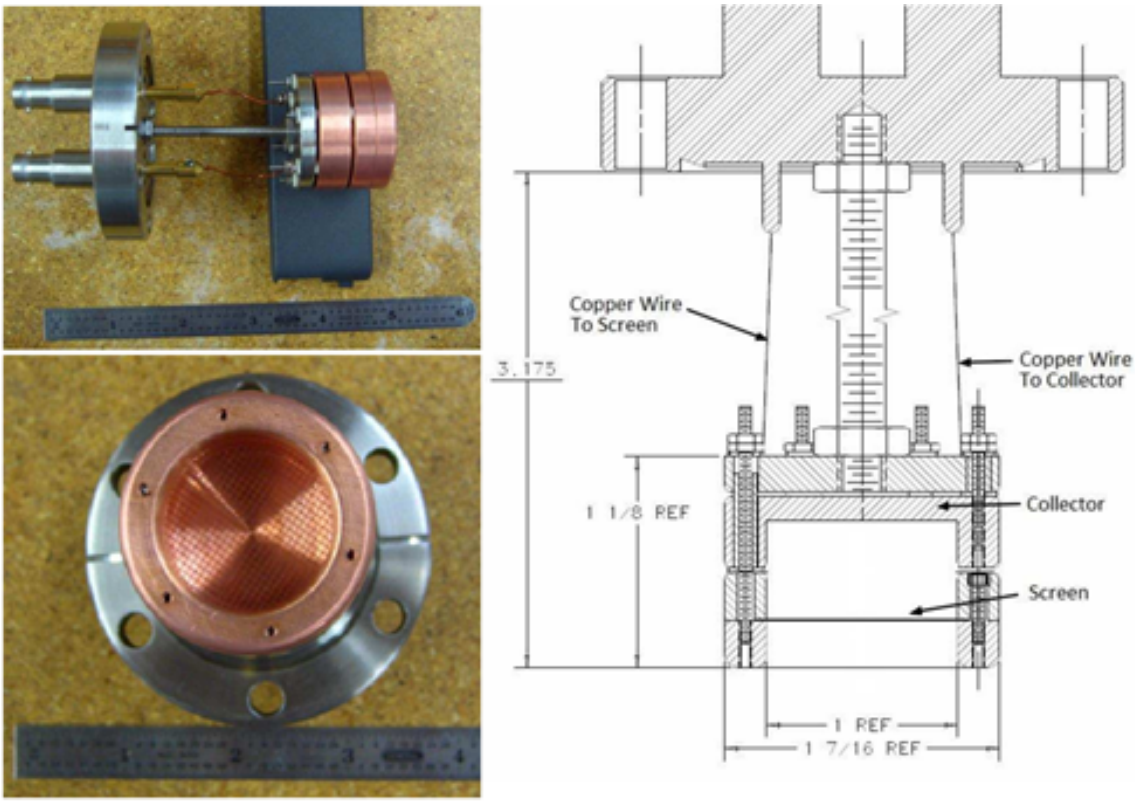

Figure 4.1. The Retarded Field Analyzer. The picture and drawing are created by Michael Backfish [2]

wall collision energy distribution.

4.2.1 The RFA circuitry. The RFA is connected to a SONOMA 310b Broadband Amplifier. The amplifier has an overall 30 dB gain. The bandwidth is 9 kHz to 1 GHz and the input impedance is 50 Ω. The signal is monitored directly by a scope. The scope used is a TBS2000 Digital Storage Oscilloscope. The scope has an input frequency range up to 100 Mhz and a maximum sampling rate at 500 MHz. The RFA is installed at the bottom of the MI-10 beam pipe. Based on the drawing of the grid above the RFA. The grid consists of a series of 0.04 inch diameter holes. The circular RFA cup has a 1 inch diameter. The RFA cup roughly covered 101 holes of the grid, the total surface area of the RFA is roughly 0.82 cm^2. The beam pipe is 0.12 inches thick and combine this with with the 0.04 inch diameter of the holes, only

electrons with incident angle less than 18° have a chance to pass the holes. Based on simulation, the average solid angle of incident electrons is 34°. The RFA capture efficiency was measured to be around 90% [59].

With these parameters, we can estimate the conversion factor from RFA signal to E-cloud bombardment rate. To start, every electron has a 90% chance of being captured by the RFA cup. Based on a POSINST simulation of the collision angle distribution and the geometry of the holes on the surface of the beam pipe, electrons have a 50% (50% of electrons have a incident angle small than 18° from previous chapter) chance to pass through the beam pipe holes and reach the RFA. Let R_{Brate} be the electron bombardment rate per area, [electron/(s cm^2)], then:

$$I_{RFA} = eR_{Brate}P_C P(\theta)A_{RFA} \tag{4.1}$$

$$= 1.602 \times 10^{-19}\,[\mathrm{C}]\, R_{Brate} \left[\frac{N_e}{\mathrm{s\ cm}^2}\right] \times 90\% \times 50\% \times 0.82\,[\mathrm{cm}^2]$$

$$I_{RFA} = 5.59 \times 10^{-20}\,[\mathrm{C\ cm}^2]\, R_{Brate} \left[\frac{N_e}{\mathrm{s\ cm}^2}\right] \tag{4.2}$$

In Eq. 4.1 I_{RFA} is the direct RFA current, e is the charge of an electron, P_C is the RFA capture efficiency, $P(\theta)$ is the electron's probability of passing through the beam pipe holes, which is dependent on the incident angle θ, and A_{RFA} is the active area of the RFA detector.

Then the RFA current signal goes through the SONOMA 310b amplifier and becomes a voltage signal.

$$V_{RFA} = I_{RFA}Z_{in}(\frac{V_{out}}{V_{in}}) = eR_{Brate}P_C P(\theta)A_{RFA}Z_{in}(\frac{V_{out}}{V_{in}}) \tag{4.3}$$

The amplifier has a 50 Ω input impedance and 30 dB gain. The 30 dB gain increases the signal by 31 times, so that:

$$(\frac{V_{out}}{V_{in}}) = 10^{\frac{gain[dB]}{20}} = 10^{3/2} = 31 \tag{4.4}$$

Putting Eq. 4.2 and Eq. 4.4 into Eq. 4.3,

$$\begin{aligned} V_{RFA} &= I_{RFA} Z_{in} (\frac{V_{out}}{V_{in}}) \\ &= 5.59 \times 10^{-20}\ [\mathrm{C\ cm^2}]\ R_{Brate} \left[\frac{N_e}{\mathrm{s\ cm^2}}\right] \times 50[\Omega] \times 31 \\ &= 8.865 \times 10^{-17} [\mathrm{C\ \Omega\ cm^2}]\ R_{Brate} \left[\frac{N_e}{\mathrm{s\ cm^2}}\right] \end{aligned} \tag{4.5}$$

The RFA signal to bombardment rate conversion factor is obtained using equation 4.5.

$$\begin{aligned} R_{Brate} \left[\frac{N_e}{\mathrm{s\ cm^2}}\right] &= \frac{V_{RFA}[\mathrm{V}]}{8.865 \times 10^{-17}\ [\mathrm{C\ \Omega\ cm^2}]} \\ &= V_{RFA}\ (\text{in volts}) \times 1.128 \times 10^{16} \left[\frac{N_e}{\mathrm{s\ cm^2}}\right] \end{aligned} \tag{4.6}$$

Putting the electron charge e back into the equation 4.6:

$$eR_{Brate} \left[\frac{A}{\mathrm{cm^2}}\right] = V_{RFA}\ (\text{in volts}) \times 1.807 \times 10^{-3} \left[\frac{A}{\mathrm{cm^2}}\right] \tag{4.7}$$

$$eR_{Brate} \left[\frac{\mu A}{\mathrm{cm^2}}\right] = V_{RFA}\ (\text{in mV}) \times 1.807 \left[\frac{\mu A}{\mathrm{cm^2}}\right] \tag{4.8}$$

The conversion factor in equation 4.8 will be used in a later section when the simulation results are compared to RFA measurements.

4.2.2 RFA signal processing. The purpose of an RFA detector is to measure the density of an electron cloud in the beam chamber. However, the beam induces an

image current in conducting beam pipe walls that has nothing to do with the electron cloud density in the vacuum chamber; yet it can add to the RFA signal. The image current mimics the beam current, and so it must be distinguished from the signal due to electron cloud. It is necessary to filter out the image current to clearly identify the electron cloud signal.

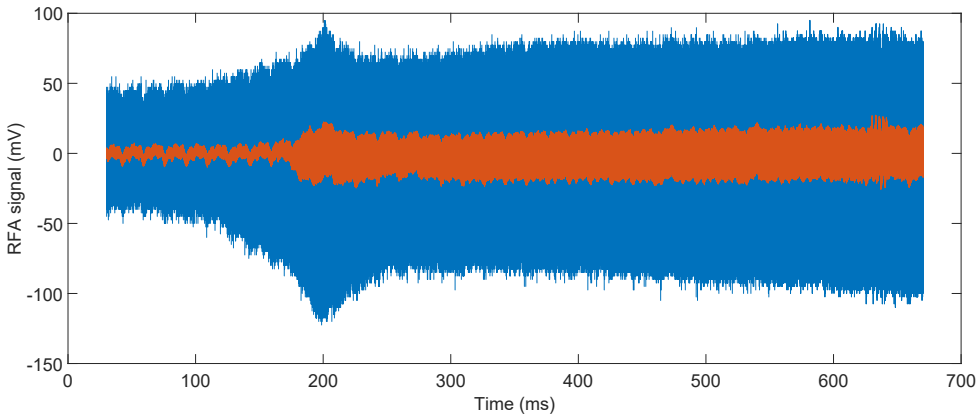

Figure 4.2. The RFA signal over a full acceleration cycle for Main Injector. The blue trace is the raw data, and the orange trace is filtered data. The beam intensity was 50×10^{12} protons.

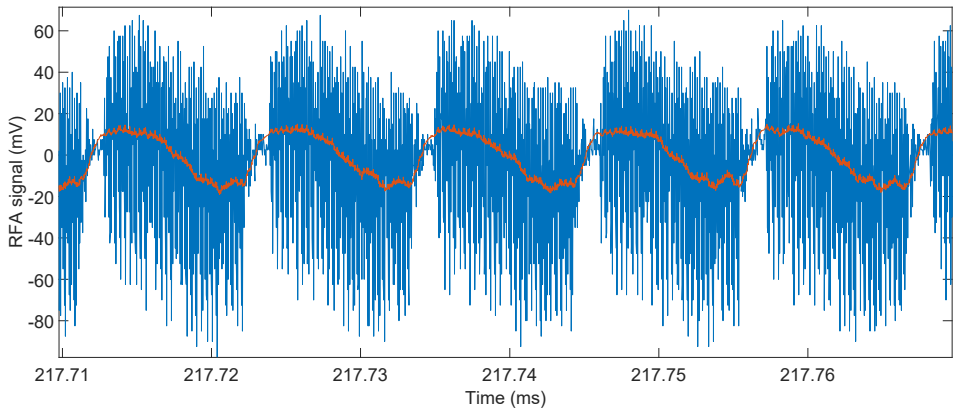

Figure 4.3. The RFA signal zoomed in for 5 turns. The blue trace is the raw data, and the orange trace is filtered data. The beam intensity was 50×10^{12} protons. Note that this is electron induced current, the signal is negative.

Figure 4.2 shows a typical RFA signal. This signal covers 0.64 seconds of the 0.72 MI cycle. During the data acquisition, the beam intensity was 50×10^{12} protons,

Table 4.1. MI parameters

Acceleration cycle [s]	1.33
Beam energy [GeV]	8-120
Intensity [protons]	50×10^{12}
revolution frequency [kHz]	90
Harmonic number	588
RF frequency [Mhz]	53
Total RF bucket filled	492
SEY	1.2-1.4
Bunch length [ns]	0.5-4
Transition energy [GeV]	20
Transition time [s]	0.2
Extraction time[s]	0.67

the SEY was measured to be 1.3 ± 0.05. The scope was set to trigger 0.355 seconds after beam enters the MI. The signal misses the first 0.015 seconds and the last 0.1 seconds of the acceleration cycle. Table 4.1 shows the relative parameters of the MI. Figure 4.3 shows the RFA signal over a time span of 5 beam revolutions(turns). As shown in the figure, the RFA signal not only contains the E-cloud build up information, but also image current that mimics the beam current. In order to measure the E-cloud generation signal, the image current induced noise has to be removed. To remove such noise, a frequency filtering process is introduced. The RFA data is collected at a 31.25 MHz sampling frequency by the scope, then averaged over 62 points to filter out high frequencies above 0.5 MHz. The RF frequency is 53 MHz and the revolution frequency is 90 kHz. This filtering process will remove the 53 MHz image current and bunch-by-bunch E-cloud generation signal, while keeping the turn-by-turn E-cloud generation signal. In figures 4.2 and 4.3, the blue line is the original signal, and the orange line is the filtered data. In figure 4.3 the image current noise was clearly observable and largely shadowed the electron cloud build-up signal.

After filtering, a clear build-up is observed.

The image current signal can also be used to determine when the beam is passing the RFA detector. Then, the RFA signal can be separated into each turn. The figure 4.3 zoomed in 5 turn signal shows how each turn is distinguished. There is a clear gap between each turn due to the MI filling pattern. Beam fills only 6/7 of the MI ring; 1/7 of the MI is left empty to enable a beam abort kicker to turn on with no beam passing through it. The full acceleration cycle signal may therefore be cleanly separated into each turn. The 0.64 second data contains about 58000 turns. The E-cloud build up process is very fast, it's a turn-by-turn process. Figure 4.3 shows that the E-cloud builds up when beam is present and resets over the abort gap.

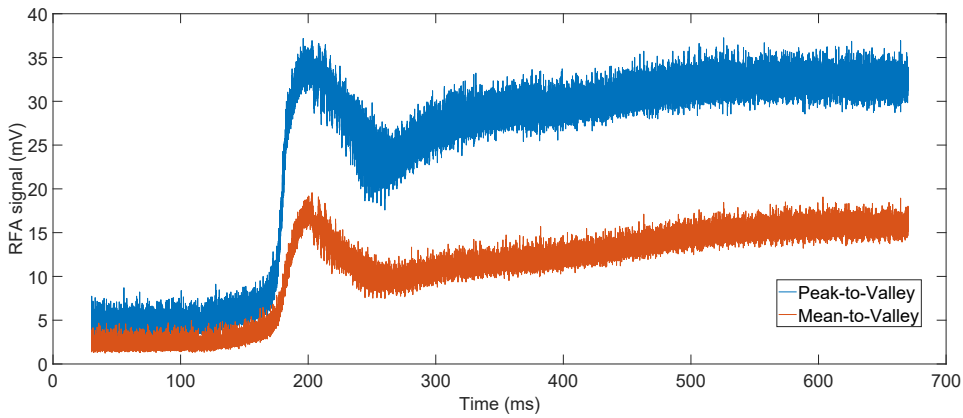

Figure 4.4. The RFA processed signal with 50×10^{12} beam intensity and 1.3 SEY.

As shown in figure 4.2 there is also extra low frequency noise introduced to the RFA signal. This low frequency noise came from ramping up of magnets and other cycle dependent background. The low frequency noise can be removed with some processing. The peak-to-valley and mean-to-valley variation is extracted for each turn. Once this is done, the variation in the ecloud signal can be plotted over the entire acceleration cycle, using either the peak-to-valley or the mean-to-valley number for each turn. Figure 4.4 shows the processed RFA data.

4.3 Experimental Data

4.3.1 Energy distribution of the E-cloud. The screen voltage of the RFA is an adjustable retarding voltage experienced by electrons before the RFA detector collects them. The screen is located between the beam pipe holes and the detector cup. Ideally, the screen voltage prevents low energy electrons from making it to the RFA detector while not affecting the E-cloud build up process. By changing the screen voltage, the RFA measures the E-cloud collision energy distribution. As the screen voltage increases, the RFA signal should go down as the energy acceptance goes down. Figure 4.5(a) shows a measurement of the RFA signal vs screen voltage, where the RFA signal is the peak-to-valley signal measured at the end of the accelerating cycle. The screen voltage measurement is directly comparable to the simulated collision energy distribution. As the screen shields electrons with collision energy lower than the screen voltage, ideally the collision energy from simulation should be one-to-one comparable with the screen voltage measurements. The collision energy gives the electron energy distribution when they hit the beam pipe. The electrons that hit the beam pipe with collision energy higher the screen voltage will be collected by the RFA; electrons hitting the beam pipe with collision energy lower than the screen voltage will be ignored by the RFA. Figure 4.5(b) shows the simulated percentage of electrons in the distribution that are above each collision energy.

The comparison between the measured and simulated electron energy distribution provides confirmation that the source of the RFA signal is the E-cloud. On the other hand, this comparison gives the ground level of the RFA system. When the number of electron counts is too low, the noise will shadow the E-cloud build up signal. In the RFA signal processing procedure, the ground level is the minimum peak-to-valley value. When there are not enough electrons hitting the RFA to produce a signal higher than the ground level, the RFA signal will always be at the ground

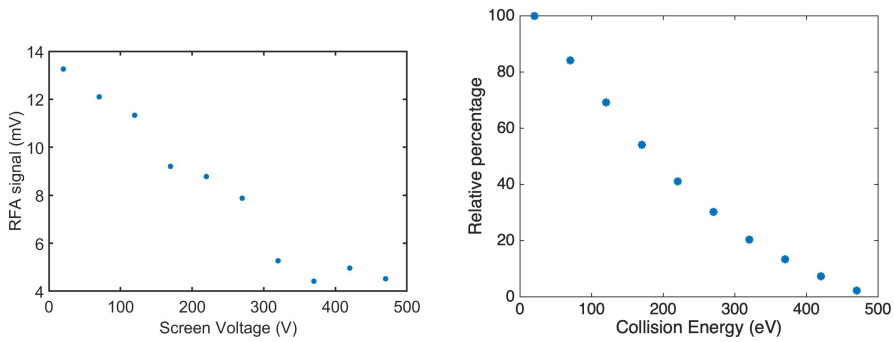

(a) The RFA signal (b) The simulation

Figure 4.5. The RFA signal vs screen voltage compared to collision energy simulation

level. The screen voltage measurement can be used to determine the noise level of the system. By increasing the screen voltage, the number of electrons entering the RFA decreases and the RFA signal reaches a plateau at the ground level. As can be seen in figure 4.5(a), at a 20 V screen voltage, the RFA signal is around 13 mV. As the screen voltage is increased, the RFA signal decreases, reaching a plateau after 300 V. Examination of figure 4.5(b) shows the simulation predicts that the signal should continue to decrease. The RFA ground level noise starts to shadow the E-cloud signal after a 300 V screen voltage. The noise level is determined to be around 5 mV. Plugging the 5 mV ground level noise into equation 4.8, the RFA ground level noise translates to 9.035 μA/cm^2 electron dose.

$$eR_{Brate}\left[\frac{\mu A}{\text{cm}^2}\right] = V_{RFA}\,(\text{in mV}) \times 1.807\left[\frac{\mu A}{\text{cm}^2}\right]$$

$$9.035\left[\frac{\mu A}{\text{cm}^2}\right] = 5mV \times 1.807 \tag{4.9}$$

4.3.2 Bunch length and intensity dependency of the E-cloud generation. The beam intensity is a major factor of the E-cloud build-up process. The RFA can be used to measure how intensity affects the E-cloud build up process. Figures 4.6

and 4.7 show scans of the E-cloud generation dependence on beam intensity over the MI acceleration cycle. The scope trigger is set to be 0.355 seconds after the beam leaves the RR and covers 0.64 seconds of the 0.7 second MI acceleration cycle. Figure 4.6 shows how the peak to valley E-cloud generation changes for every turn over the acceleration cycle. Figure 4.7 shows the averaged E-cloud build up signal over every turn of the acceleration cycle. For E-cloud to generate a signal above the 5 mV ground level noise, the beam intensity has to be above 45×10^{12} protons.

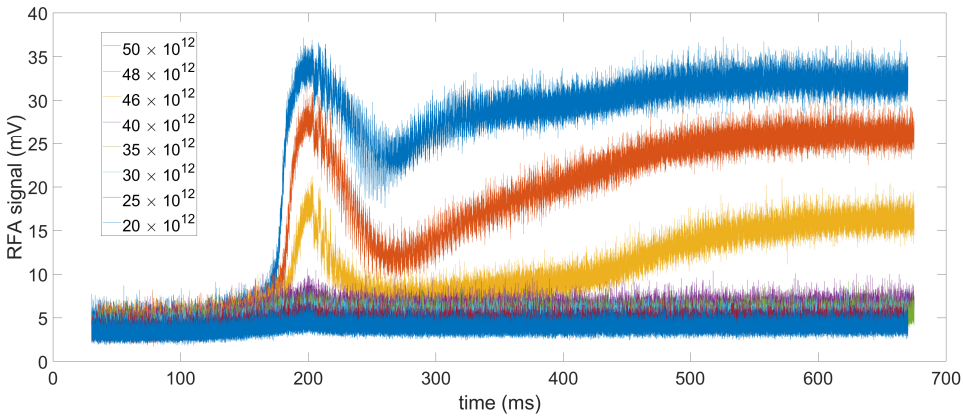

Figure 4.6. The Peak-to-Valley RFA signal of 8 different intensities

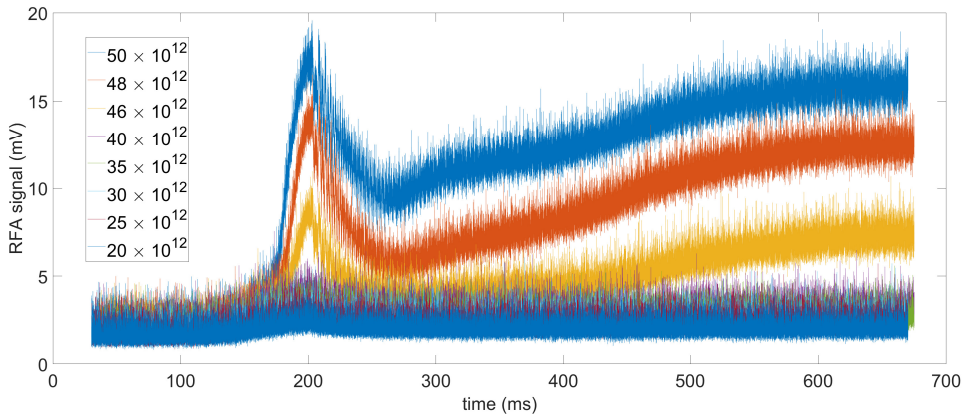

Figure 4.7. The Mean-to-Valley RFA signal of 8 different intensities

The RFA measurements show that the E-cloud generation starts about 0.17

second into the acceleration cycle, is a maximum at transition, drops after transition and rises up slowly again. E-cloud generation over one machine cycle could be dependent on several factors. In this case, the E-cloud generation trend is mainly caused by bunch length (σ_t), and changes over the acceleration cycle. Figure 4.8 shows a comparison of the peak-to-valley RFA signal and the bunch length over the acceleration cycle. The bunch length was obtained using the BlonD simulation code with inputs matched to MI conditions. The electron cloud density trend is the inverse of the bunch length trend. E-cloud generation starts when the bunch length decreases enough to generate an observable E-cloud. At transition, the bunch length is minimized and the E-cloud generation is maximized. After transition, the bunch length increases and then decreases, while the RFA signal decreases and then increases. The major features of the bunch length are inversely matched on the RFA signal.

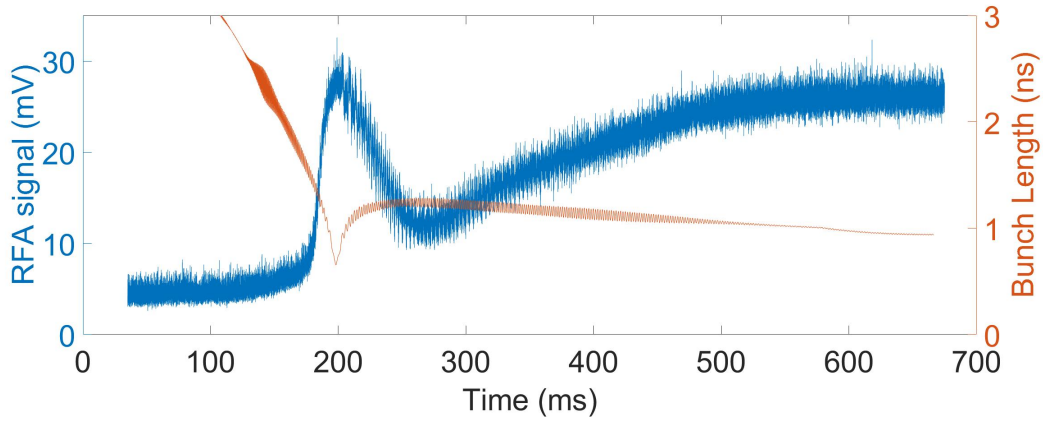

Figure 4.8. The RFA signal measuring electron cloud density compared with the simulated bunch length (σ_t) over an acceleration cycle. The bunch length was simulated using the BlonD code with MI conditions. The beam intensity was 50×10^{12} during the measurement.

The peak-to-valley and the mean-to-valley plot in figures 4.6 and 4.7 show a little different trend after transition. The mean-to-valley drops more compared to the peak-to-mean. Then when the E-cloud generation starts to increase again, the peak-to-valley for 50×10^{12} case shows a short sharp increase where the mean-to-valley

shows a smoother increase. This effect was caused by the E-cloud saturation. The saturation of the E-cloud density is caused by the space charge force between the E-cloud electrons. The saturation happens when the E-cloud density is high enough so that the space charge force of the E-cloud on an electron cancels the kick from the bunched beam. Because the E-cloud generation is a turn-to-turn effect, the E-cloud resets every turn. Saturation has a major effect on the RFA signal, and affects the peak of the signal differently than the mean of the signal. Figure 4.9 shows simulations of the E-cloud build up over one turn for different cases. To illustrate the saturation process, the individual cases are chosen with relative extreme parameters.

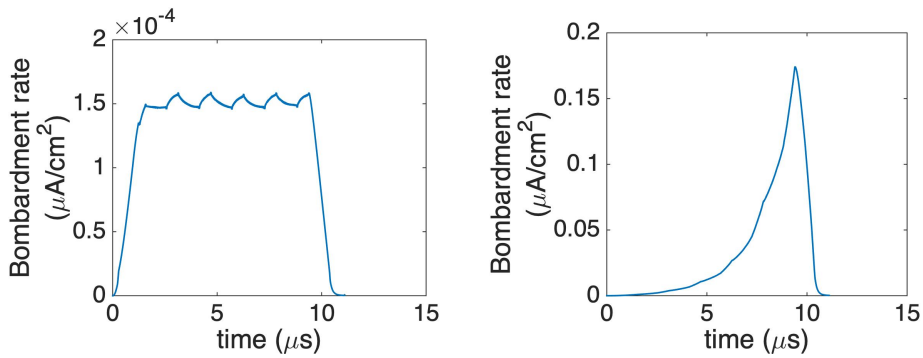

(a) No cloud build up (SEY=1.2, BL=3) (b) Cloud build up but no saturation (SEY=1.2, BL=0.8)

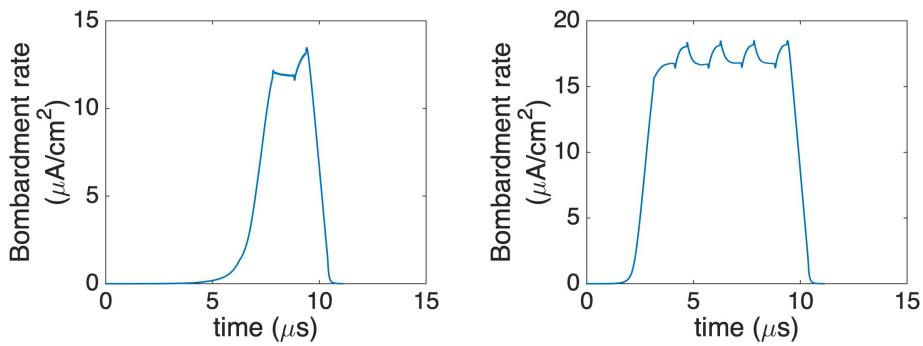

(c) Slow saturation (SEY=1.35, BL=2) (d) Fast saturation (SEY=1.4, BL=0.8)

Figure 4.9. Simulation of the electron bombardment rate over one turn for different combinations of SEY and bunch length. One revolution (turn) takes about 11 μs. Top left: no cloud buildup, top right: build up but no saturation, bottom left: slow build up to saturation, Bottom right: fast build up to saturation. BL stands for bunch length, beam intensity $= 50 \times 10^{12}$.

Figure 4.9(a) shows the case where E-cloud does not build up (note the scale of the figure). Figure 4.9(b) shows the case where E-cloud builds up but does not reach saturation within that turn. Figure 4.9(c) shows a case where E-cloud reaches saturation relatively slowly, saturation is reached right before the abort gap kills the E-cloud generation. Figure 4.9(d) shows the case where E-cloud reaches saturation relatively fast, the saturation is reached very soon into that turn. Whether E-cloud generation reaches saturation or not primarily depends on bunch length, SEY and beam intensity. The density of the E-cloud at saturation also depends on bunch length, SEY and beam intensity. For the RFA measurements shown in figures 4.6 and 4.7, the SEY and beam intensity stay relatively constant within a specific acceleration cycle. The variation of the bunch length causes the variation of the RFA signal over the cycle. When the bunch length decreases, the E-cloud generation starts with the non-satuation case, then starts to saturate and eventually, when the bunch length is short enough, the E-cloud density saturates relatively fast. Before the E-cloud generation saturates, the peak-to-valley and mean-to-valley of the RFA signal increase in the same way. After saturation, the peak-to-valley only measures the saturation density while the mean-to-valley also measures how early the saturation happens. This explains the different trend between figures 4.6 and 4.7.

4.4 Comparison of data to simulations

Comparing the RFA data to simulation is a good benchmark of the simulation performance. When there is reasonable agreement between simulation results and measurements, the simulations can be used to predict electron cloud generation for future or alternative operational regimes. Using measured bunch length data, the measured RFA E-cloud bombardment rate trend can be reconstructed with the POSINST simulation. The bunch length measurement for the MI beam is not readily available over the entire acceleration cycle. So instead, the bunch length over the

acceleration cycle is calculated based on BlonD simulations paired with several wall current monitor measurements. The bunch length was measured with the wall current monitor at several different times over the acceleration cycle of the MI.

4.4.1 Bunch length over acceleration cycle. The wall current monitor measures the longitudinal particle distribution of the beam using the beam image current. Figure 4.10 shows a typical wall current monitor measurement consisting of 1000 ns of data. Figures 4.10(b) and 4.10(c) show single bunch wall current monitor data. A Gaussian fit is applied to extract the bunch length.

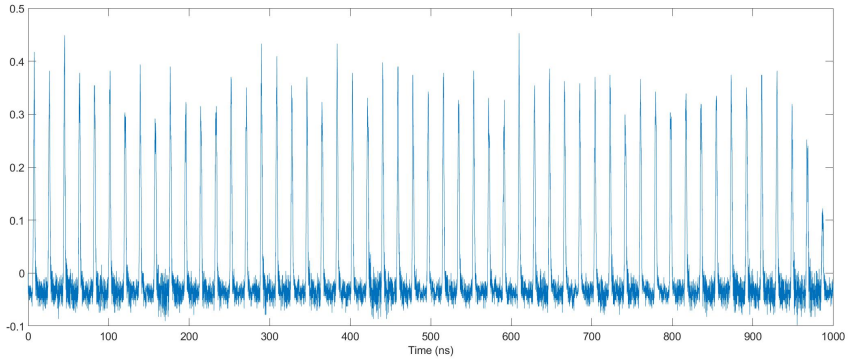

(a) 50 bunches at extraction, 1.03 ns bunch length

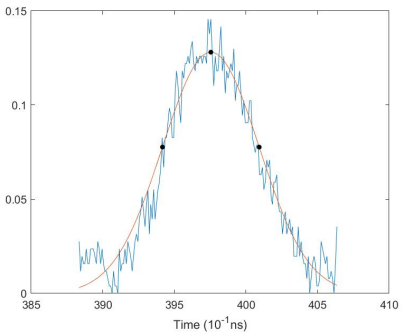

(b) Single bunch at injection, 3.7 ns bunch length

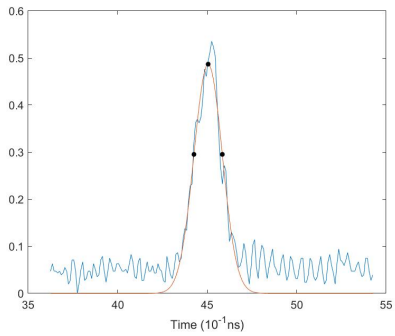

(c) Single bunch at extraction, 1.03 ns bunch length

Figure 4.10. The wall current bunch length measurements at 50×10^{12} beam intensity.

There is currently no capability to get detailed bunch length data over a full

acceleration cycle. The wall current monitor beam diagnostic gives good bunch length measurements, but only for very short time period. In order to get bunch length data for every turn for a full acceleration cycle to compare with the RFA data, the bunch length must be simulated and then scaled with wall current monitor data.

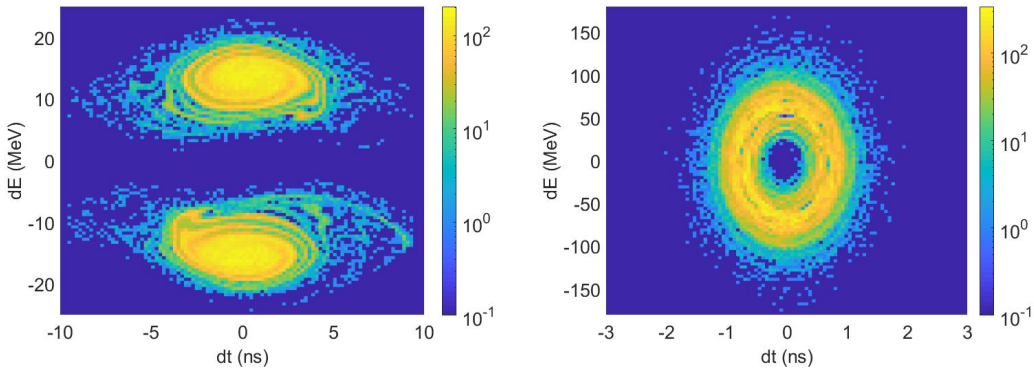

(a) Initial (b) Final

Figure 4.11. The initial and final macro-particle phase space distribution for the MI in BlonD simulation.

Table 4.2. MI input parameter for BlonD simulation

Parameters	Value
Macro-particles	131072
Intensity [ppb]	11×10^{10}
f_{rev} [kHz]	89.6
Harmonic number	588
f_{rf} [MHz]	53
γ_t	21.6

Rob Ainsworth simulated the MI longitudinal beam dynamics over the acceleration cycle [60, 61] with the BlonD code; results from the best fit simulation are used to get the basic bunch length trend over the acceleration cycle and then this is scaled with the wall current measurements. The BlonD simulation code or Beam Longitudinal Dynamics code was developed by CERN [58]. It tracks the longitudinal dynamics of the beam based on the longitudinal distribution of particles in the

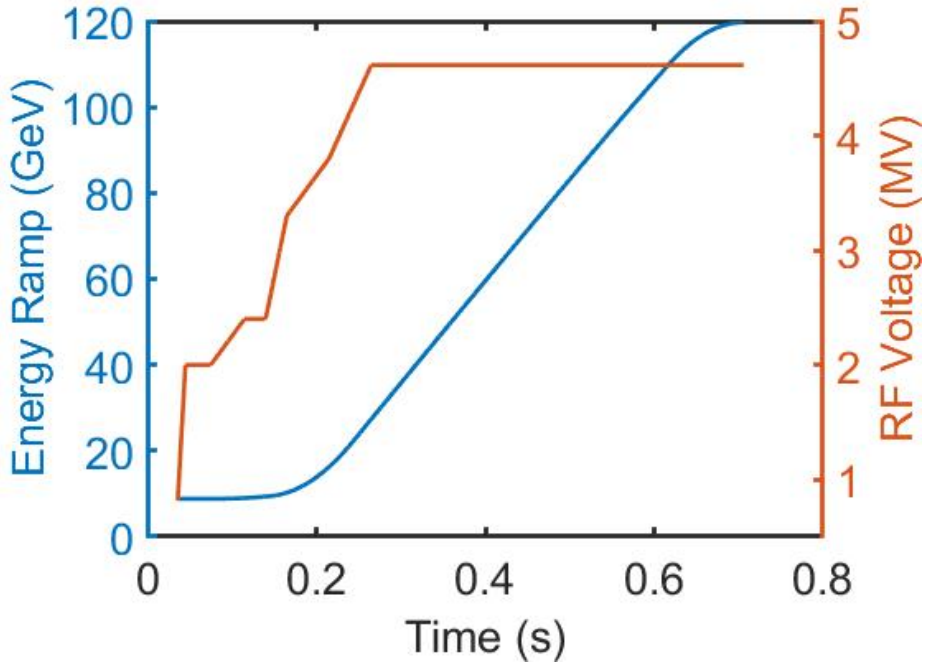

Figure 4.12. The beam energy ramp and RF voltage ramp during the acceleration cycle used for the BlonD simulation.

bunch and known machine parameters such as the energy gain versus time during the cycle. The energy gain and the RF voltage over the acceleration cycle are shown in figure 4.12. The BlonD input parameters are given in table 4.2. The initial and final longitudinal beam phase space is shown in figure 4.11. In figure 4.11 the x-axis is the time deviation from the reference time of an ideal particle following the design trajectory; the y-axis is the energy deviation from the design energy; the color scale indicates the number of macro-particles. The effect of slip stacking is shown in figure 4.11(a) [13]. Slip stacking is a technique that fills one bucket with two beam bunches. In the BlonD simulation, the initial beam distribution (figure 4.11(a)) is slip stacked beam, the two bunches are separated in phase space due to a difference in their average energy. After the MI acceleration, the two slip stacked bunches smear and merge into one unit (figure 4.11(b)). The beam energy depends on the beam energy gain each turn, the RF voltage, RF frequency and RF phase over the acceleration cycle.

Such input data are directly determined from MI [61] parameters. Figure 4.12 shows the beam energy and the RF voltage ramp over the acceleration cycle.

Figure 4.14 shows the BlonD simulation result (blue line), the wall current data (orange dots) and the scaled bunch length (yellow line). The bunch length from BlonD simulation is scaled to fit the wall current measured data; the method will be described in more detail below. Eight wall current monitor measurements were used. The 8 data points were taken at 0.00007 s, 0.10007 s, 0.20007 s, 0.30007 s, 0.40007 s, 0.50007 s, 0.60007 s and 0.6394 s after the beam left the RR. (The RR acts as the injector for the MI.). The 0.00007 s and 0.6394 s measurements were taken at the exact moment that beam was injected and extracted from the MI, while the 0.20007 s measurement was taken exactly at the beam transition.

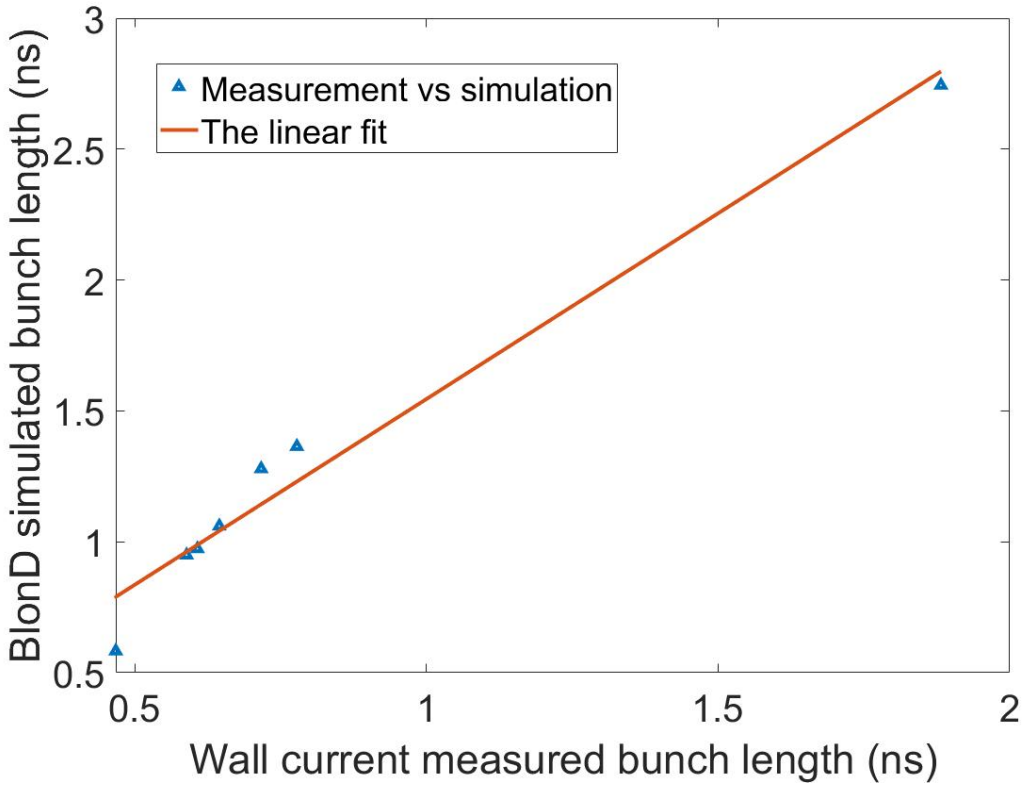

Figure 4.13. The linear fit between the BlonD simulation result and the wall current monitor measurements

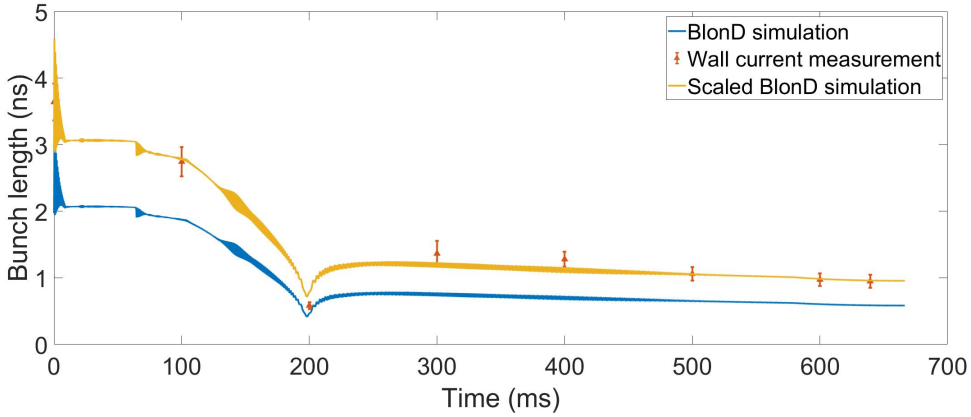

Figure 4.14. The BlonD simulated bunch length (blue curve); eight wall current bunch length measurements (yellow circles); and the scaled, simulated bunch length (yellow curve).

Eight bunch length data points were extracted from the BlonD simulation at the times corresponding to the wall current data measurements. The wall current data and the BlonD simulation were aligned based on the transition time. A linear fit was calculated based on the points extracted from BlonD and the wall current measurements. Figure 4.13 shows the linear fit. Since the Blond data were extracted based on the wall current measurement time, each measured bunch length has a corresponding BlonD simulated bunch length. The blue dots in figure 4.13 plot the two corresponding bunch lengths for 0.10007 s, 0.20007 s, 0.30007 s, 0.40007 s ,0.50007 s, 0.60007 s and 0.6394 s. In figure 4.13, the x-axis is the wall current measured bunch length and the y-axis is the corresponding BlonD simulated bunch length. The 0.00007 s point is ignored because the BlonD simulation result starts with a large bunch length oscillation, which does not compare well with wall current measurements. A linear fit (red line in figure 4.13) is applied to the other points. This linear fit can be used to scale the full BlonD simulation result based on the measured bunch length. The simulated, scaled bunch length trend over the acceleration cycle is shown by the yellow line in figure 4.14.

4.4.2 Simulation of the RFA signal. The scaled BlonD simulation result is used as the bunch length input to the POSINST simulation. The bunch length data is used as an input to the E-cloud generation simulation(POSINST), and the resulting electron bombardment rate plotted against time will produce a simulated RFA signal. Figure 4.15 shows a series of simulations of RFA signals of the peak-to-valley and mean-to-valley electron bombardment rate dependency on bunch length for different values of SEY and beam intensities. In figure 4.15 the simulated bunch length range is 0.2 ns to 2 ns with a 0.1 ns increment. The simulation used values of MI parameters and the measured beam intensity as input parameters to allow comparison with measurements. The SEY range starts at 1.25 because it is known from previous studies that 1.2 SEY suppresses all E-cloud generation for MI. The bunch length covers the range that the E-cloud at a beam intensity of 50×10^{12} protons saturates up to 1.4 SEY. The scaled BlonD simulated bunch length over the acceleration cycle is fed to the POSINST simulation so that it can calculate the E-cloud developments over the acceleration cycle. The POSINST simulation does not have the resolution to cover all the fine bunch length variance. The bombardment rate for bunch lengths that are between simulation points are linear extrapolations between simulated data points.

Figure 4.16 shows POSINST simulations of E-cloud generation over the acceleration cycle from 0.167 s into the acceleration cycle to the end of acceleration for different values of SEY. The first 0.167 s of the acceleration cycle is ignored because the bunch length for that time period is higher than 2 ns, so E-cloud build up does not happen for the SEY values plotted. The SEY range starts at 1.25 since E-cloud generation is generally suppressed below 1.2. It can be seen from figure 3.9 that the 1.25 SEY simulation result matches the RFA measurement relatively well. The general trend around injection, transition and extraction agrees. In the RFA measurement, only beam intensities 45×10^{12}, 48×10^{12} and 50×10^{12} showed clear E-cloud build-up.

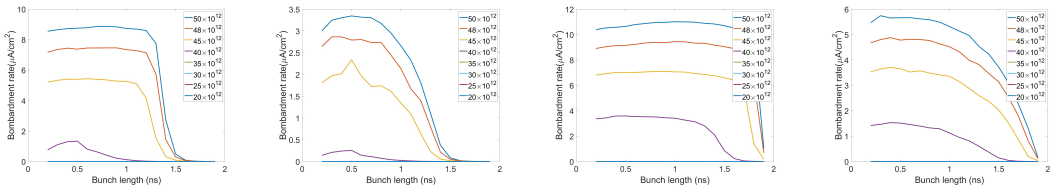

(a) 1.25 SEY Peak-to-Valley (b) 1.25 SEY Mean-to-Valley (c) 1.30 SEY Peak-to-Valley (d) 1.30 SEY Mean-to-Valley

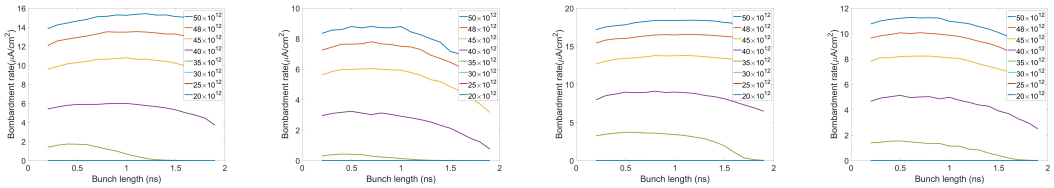

(e) 1.35 SEY Peak-to-Valley (f) 1.35 SEY Mean-to-Valley (g) 1.40 SEY Peak-to-Valley (h) 1.40 SEY Mean-to-Valley

Figure 4.15. The POSINST simulated bunch length dependency of the electron bombardment rate for different SEY and beam intensities.

This feature matches the 1.25 SEY result as well. The SEY measured on Jul 25th 2019 was 1.25 ± 0.05, about 3 weeks after the RFA measurement. The SEY measured SEY and simulation suggested SEY agrees.

The general shape of the measured RFA signal matches well with the simulation for the same beam intensity and very similar SEY value. Now a comparison between the estimated electron bombardment rate based on the RFA signal strength and the calculated rate from simulation can be done. Using the bombardment rate at transition for the beam intensity of 50×10^{12}, the RFA signal level from figure 4.6 is about 35 mV. Inserting this value into equation 4.8 results in an estimated bombardment rate from the measurement.

$$eR_{Brate}\left[\frac{\mu A}{\text{cm}^2}\right] = V_{RFA}\,(\text{in mV}) \times 1.807\left[\frac{\mu A}{\text{cm}^2}\right]$$

$$63.245\left[\frac{\mu A}{\text{cm}^2}\right] = 35mV \times 1.807 \tag{4.10}$$

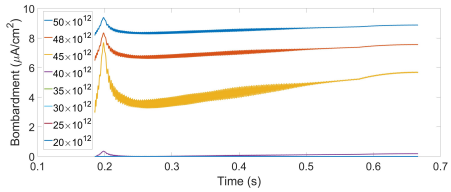

(a) 1.25 SEY Peak-to-Valley

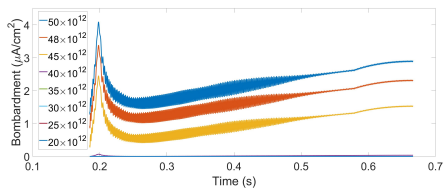

(b) 1.25 SEY Mean-to-Valley

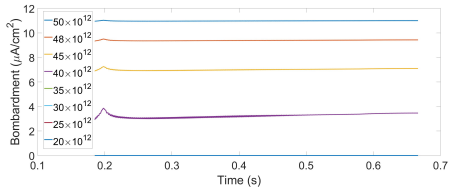

(c) 1.30 SEY Peak-to-Valley

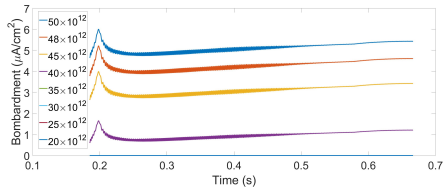

(d) 1.30 SEY Mean-to-Valley

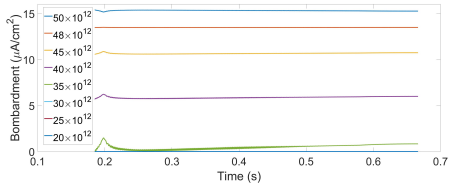

(e) 1.35 SEY Peak-to-Valley

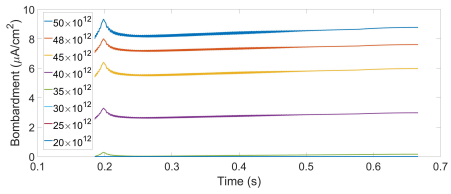

(f) 1.35 SEY Mean-to-Valley

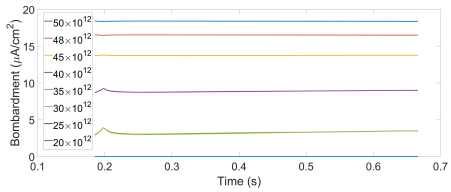

(g) 1.40 SEY Peak-to-Valley

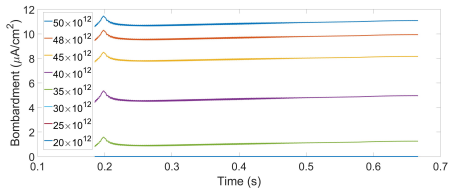

(h) 1.40 SEY Mean-to-Valley

Figure 4.16. The POSINST simulated electron bombardment rate dependence on bunch length for different values of SEY and beam intensities.

The simulated bombardment rate at transition for the 50×10^{12} intensity case is about 9 μA/cm^2 (see figure 4.16(a)). The simulated value is 7 times smaller than is suggested by the RFA measurement. While there is a quantitative disagreement between the bombardment rates from the RFA measurement and the POSINST simulation, it still can be concluded that the simulation and the measurement agree well qualitatively. In order for POSINST to generate the bombardment rate dependence on bunch length that is observed on the RFA signal, the input parameters for the simulation (SEY, bunch length, beam intensity) must be in good agreement with the measured values of these parameters. The measured bombardment rate shows sensitive bunch length dependency for the range of 1 ns to 1.5 ns (the bunch length variance range for majority of the acceleration cycle). The input parameter space for SEY and beam intensity is narrow for good agreement between simulation and experimental data. Further, these input values must be specifically those that match conditions when data was taken. In particular, for the beam studies presented here, the simulation requires an SEY between 1.225 to 1.25, while only beam intensities in the range measured experimentally (50×10^{12}, 48×10^{12} and 45×10^{12}) result in the type of E-cloud build up that was observed.

While there is excellent qualitative agreement between data and simulation, the discrepancy in the measured to simulated bombardment rate is not unexpected. This quantitative difference can came from uncertainties in the parameters used to calculated the conversion factor. The signal level to bombardment rate conversion for the RFA is based on estimations of the angular distribution of electrons, the acceptance of the detector, and the performance of the electronics. Also, the bombardment rate calculated from the simulation is the average bombardment rate over the full vacuum chamber surface, compared to the RFA which measures the bombardment rate at a small portion of the vacuum chamber surface. A difference of 7 in the bombardment rate is within an order of magnitude, and it would be difficult to pin that down

better. It is expected that there are sources of systematic error in the absolute bombardment rate determination. Since the simulation is in good qualitative agreement with data, the quantitative disagreement of the simulated bombardment rate to that inferred from the measurement is not a cause to doubt the validity of the simulation results.

To aid in the direct comparison of simulation to measurement, a conversion factor can be calculated for one point in parameter space. Matching the simulated transition bombardment rate, 9 μA/cm^2 (peak-to-valley), for the 50×10^{12} intensity case to the RFA measurement (to simplify this factor use 36 mV), a quick conversion factor can be calculated.

$$\begin{aligned} eR_{Brate} &\approx 9 \left[\frac{\mu A}{\text{cm}^2}\right] \\ V_{RFA} &\approx 36\,[mV] \\ eR_{Brate} \left[\frac{\mu A}{\text{cm}^2}\right] &\approx V_{RFA}\,(\text{in mV}) \times \frac{9}{36} \left[\frac{\mu A}{\text{cm}^2}\right] \\ &= \frac{V_{RFA}\,(\text{in mV})}{4} \left[\frac{\mu A}{\text{cm}^2}\right] \end{aligned} \tag{4.11}$$

The noise floor of the RFA signal gives the lower limit for the detectable E-cloud bombardment rate. Substituting the 5 mV noise floor into equation 4.12:

$$\begin{aligned} eR_{Brate} \left[\frac{\mu A}{\text{cm}^2}\right] &= \frac{5mV}{4} \left[\frac{\mu A}{\text{cm}^2}\right] \\ &= 1.25 \left[\frac{\mu A}{\text{cm}^2}\right] \end{aligned} \tag{4.12}$$

When the E-cloud bombardment is below 1.25 μA/cm^2, the RFA will not catch the E-cloud signal because the signal is shadowed by the noise. For example, the 1.25 μA/cm^2 noise floor shadows the E-cloud signal for beam intensities below 45×10^{12} protons, in agreement with figure 4.16(a). Figure 4.17 shows the comparison between the measured RFA signal with the conversion factor applied and the simulated bombardment rate at three different intensities. The simulation and the measurement generally match with the scaling factor from equation 4.12.

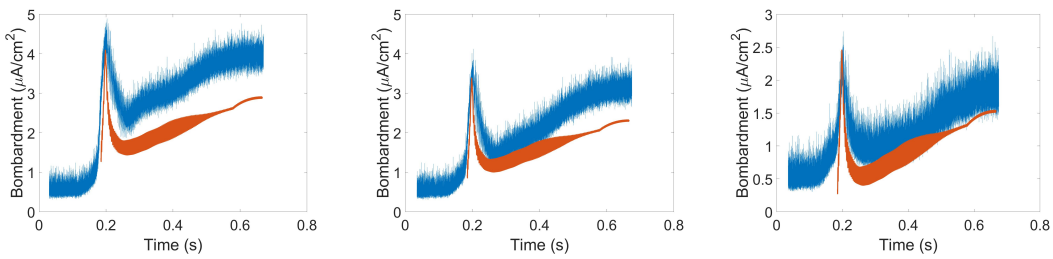

(a) 50×10^{12} protons (b) 48×10^{12} protons (c) 45×10^{12} protons

Figure 4.17. The simulation and measurement match for the new conversion factor. Comparison of the mean to valley RFA signal and bombardment rate for the three beam intensity that show clear E-cloud build up.

4.4.3 Effect of saturation. Although the estimated numerical values of the simulated and measured bombardment rates are not the same, the simulated behavior of the E-cloud otherwise matches measurements very well. As can be seen by examining the simulation results in figure 4.16, when the SEY is higher than 1.3 the peak-to-valley measurements show that the E-cloud generation saturates over the full acceleration cycle. Only in the 1.25 SEY case, does the E-cloud not saturate over the full acceleration cycle, but instead produces a bombardment rate dependence similar to that of the RFA measurement. In order to match the RFA measurement the peak-to-valley bombardment rate must change drastically over the bunch length variation that occurs during the MI acceleration cycle. Figure 4.14 shows that after transition, the MI bunch length peaks at 1.43 ns and then decreases to 0.9 ns at extraction.

Figure 4.18 is an enlarged plot of the 1.25 SEY peak-to-valley simulation result showing the bombardment rate dependence on bunch length at different beam intensities. The peak-to-valley value dives with the 1 ns to 1.5 ns range because E-cloud bombardment rate transitions from non-saturation at bunch lengths in the 1.5 ns range to saturation when the bunch length has decreased to about 1 ns. To further study the saturation process boundaries, a series of simulations around 1.25 SEY with bunch lengths between 0.9 ns to 1.5 ns were performed for 40×10^{12}, 45×10^{12},

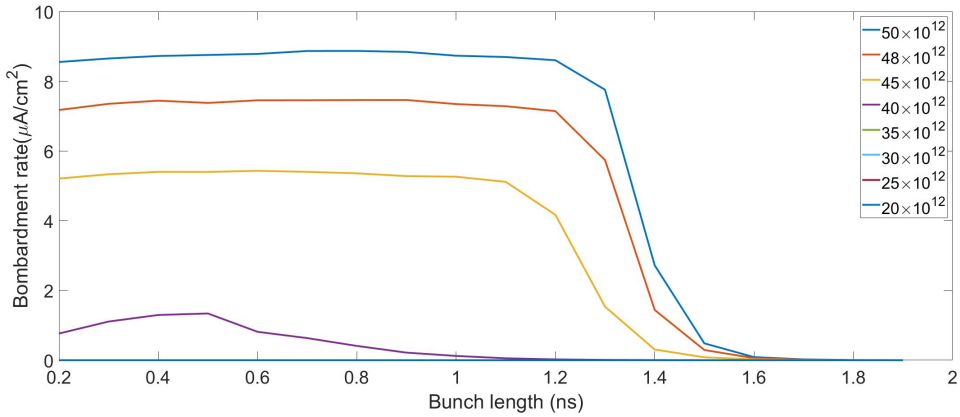

Figure 4.18. The POSINST simulated bunch length dependency for 1.25 SEY.

48×10^{12} and 50×10^{12} beam intensities. Figure 4.19 shows peak-to-valley simulation

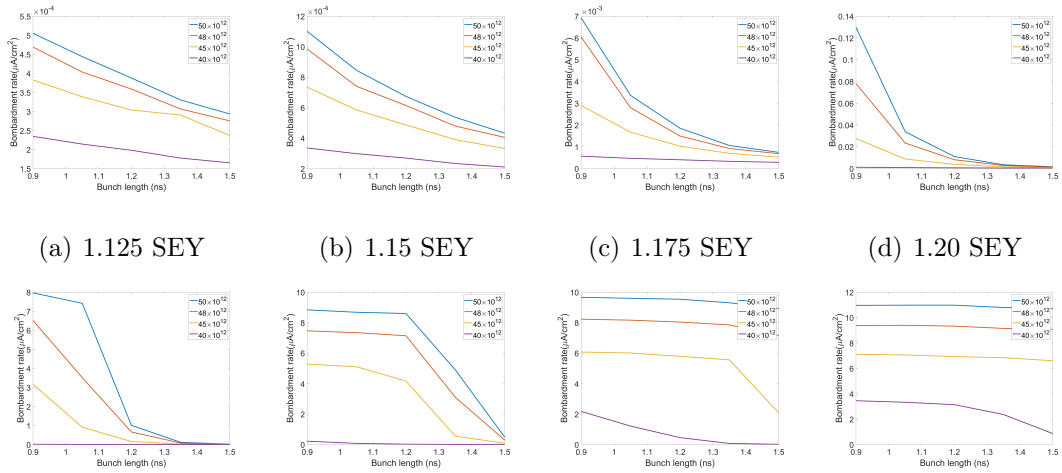

(a) 1.125 SEY (b) 1.15 SEY (c) 1.175 SEY (d) 1.20 SEY

(e) 1.225 SEY (f) 1.25 SEY (g) 1.275 SEY (h) 1.30 SEY

Figure 4.19. E-cloud bombardment rate versus bunch length for various SEY values near 1.25.

results for this parameter range. For the RFA measurement to match the simulation results, the E-cloud generation has to saturate within the 0.9 ns to 1.5 ns bunch length range. From figure 4.19, it is clear the E-cloud build up process is suppressed at and below 1.2 SEY. The two cases where E-cloud generation saturation happens within the 0.9 ns to 1.5 ns bunch length range are 1.225 and 1.25 SEY. The E-cloud generation saturates over the full 0.9 ns to 1.5 ns bunch length range for 1.275 and

1.3 SEY.

The bunch length after transition ranges from 1.5 ns to 0.9 ns. The highest three beam intensities from the E-cloud vs. beam intensity study show a significant climb in the bombardment rate during this time. For those beam intensities, there is a narrow range of SEY values that produce the same E-cloud trend in simulation. Below an SEY of 1.2 the rate does not rise above a detectable level, whereas the bombardment rate for an SEY of 1.275 or above is in saturation over the entire range of bunch lengths. (See figure 4.19.) The beam intensity and SEY are well-known directly measured parameters; whereas the bombardment rate has more uncertainty since it is an estimated parameter not based on direct measurements. There is a tight range in parameter space where the simulation matches the measurements, and the directly measured parameters of beam intensity and SEY are what place the simulation in that specific range of parameter space. So, there can be confidence in the fidelity and predictive power of the simulation.

4.4.4 Conditioning process and the RFA signal. The conditioning of surface SEY happens because of E-cloud bombardment [31]. When there is not enough E-cloud to bombard the surface of the beam pipe, the conditioning process will stop. As can be seen from figure 4.19, the bombardment rate basically goes to 0 at a threshold around 1.2 SEY, which means that the conditioning process should stop before the SEY drops below 1.2. With the current beam intensity (50×10^{12} protons), the E-cloud bombardment rate over the full acceleration cycle would stay relatively constant and relatively high if the SEY were above 1.3. (figure 4.16(d)). Once the SEY is conditioned to 1.25, the bombardment rate only stays high for a portion of the acceleration cycle(figure 4.16(b)), causing the conditioning process to slow down. As the SEY conditions further, the portion of the cycle where the E-cloud saturates decreases and further slows down the conditioning process.

On the other hand, based on studies of the SEY conditioning process [31], the electron dose required to condition a surface increases as the SEY decreases. So, when the SEY is conditioned to a range where the RFA trend is observed (only partial saturation in the 0.9 ns to 1.5 ns bunch length range), the E-cloud bombardment rate will decrease dramatically for small decreases in SEY. At the same time, the electron dose required for further conditioning increases dramatically. It can be concluded that the SEY conditioning process will stop or is about to stop very soon once an RFA trend such as exhibited in figure 4.7 is observed.

A prediction of the lowest value of SEY that can be obtained through conditioning can be made by finding where the E-cloud bombardment rate comes out of saturation. Recent measurements in MI show that E-cloud comes out of saturation at the bunch lengthens from 0.9 to 1.43 ns, so the SEY should be nearing its final conditioned value. Since the saturation process depends on SEY beam intensity and bunch length, the SEY on the threshold of mitigating E-cloud can be found in simulation by determining where the bombardment rate comes out of saturation as the bunch length increases. That SEY would also be nearing its final conditioned value. For MI operations now, a comparison between the E-cloud bombardment rate at 0.9 ns and 1.43 ns bunch lengths provides information on if the E-cloud generation saturates over the full acceleration cycle. If E-cloud is in saturation, the bombardment rate at these two bunch lengths will be comparable. As the SEY decreases with conditioning, and E-cloud generation decreases, the 1.43 ns bunch length will transition to non-saturation first. The ratio of the bombardment rate between 1.43 ns and 0.9 ns bunch lengths gives a good indication of where the condition effect will end.

For pairs of SEY and beam intensity values Figure 4.20 shows the ratio of the E-cloud bombardment rate at 1.43 ns bunch length to the bombardment rate at 0.9 ns bunch length, $R_{1.34}/R_{0.9}$. The percentage given by that ratio is indicated on the

plot by color coding the (beam intensity, SEY) point. For example, at beam intensity 60×10^{12} and SEY 1.3, the bombardment rates are equal $R_{1.43} = R_{0.9}$. In this case $R_{1.43}$ is 100% of $R_{0.9}$ and the the point is plotted in black indicating a fully saturated E-cloud. The SEY range is from 1.12 to 1.3, and the intensity range is from 40×10^{12} to 70×10^{12} protons. The color scale gives the ratio $R_{1.43}/R_{0.9}$ in percentage, where the $R_{1.43}$ and $R_{0.9}$ are bombardment rates for 1.43 ns and 0.9 ns bunch lengths. The blue line is where bombardment rate for 0.9 ns is 1.25 $\mu A/cm^2$. Bombardment rates below the blue line can not be measured by the RFA, since this is the noise level of the detector. The ratio from RFA measurements are in range of 30% to 60%, which is the yellow-red area in figure predict. When the E-cloud saturates at 1.43 ns bunch length, both 0.9 ns and 1.43 ns bunch lengths saturate, and so the ratio $R_{1.43}/R_{0.9}$ should be close to 100%. When there is a transition into non-saturation at the 1.43 ns bunch length, the $R_{1.43}$ decreases much faster than the $R_{0.9}$ rate, so the ratio $R_{1.43}/R_{0.9}$ starts to decrease and eventually reaches 0. As the SEY and beam intensity decrease further, E-cloud generation start to transition into the non-build-up situation (figure 4.9(a)). Then the $R_{1.43}/R_{0.9}$ ratio starts to increase again.

As shown in figure 4.20, at the highest levels of SEY and beam intensity, the $R_{1.43}/R_{0.9}$ starts close to 100% (dark region on top of figure 4.20), and slowly drops to almost 0% (white region in figure 4.20) as the beam intensity and SEY decrease. The black region is where E-cloud generation saturates for both 0.9 ns and 1.43 ns bunch length. Moving out of the black region, the rate at the 1.43 ns bunch length stops saturating while 0.9 ns still saturates. Eventually when the SEY and beam intensity are low enough, both 0.9 ns and 1.43 ns bunch lengths stop experiencing E-cloud generation. Then the ratio increases again to almost 100% (dark region on bottom of figure 4.20).

The white region in figure 4.20 separates the parameter space where E-cloud

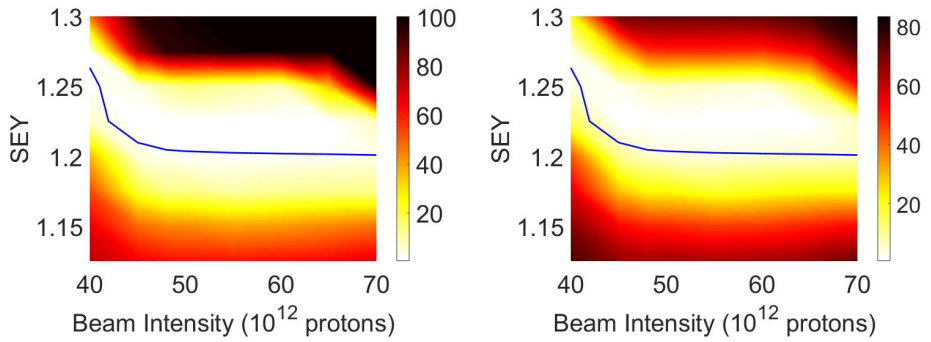

(a) Bombardment rate calculated based on peak to valley difference.

(b) Bombardment rate calculated based on mean to valley difference.

Figure 4.20. The simulated ratio $R_{1.43}/R_{0.9}$ for 1.125 to 1.3 SEY and 40×10^{12} to 70×10^{12} protons beam intensity. The blue curve is the ground noise level (1.25 $\mu A/cm^2$) line. RFA cannot measure data below blue line.

generation happens and does not happen. For any beam intensity where the ratio falls within the white region, E-cloud will not condition the beam pipe surface because E-cloud generation is greatly suppressed there. So, in the MI the beam pipe will never condition below 1.2 SEY for beam intensities below 70×10^{12}. At the same time, the 30% to 60% $R_{1.43}/R_{0.9}$ ratio from the RFA measurement suggests that the conditioning process for MI-10 vacuum chamber is stopped or is on the edge of stopping. The RFA trend should only be observable in the top red to yellow region, as the bombardment of the white region drops below the noise level, 1.25 $\mu A/cm^2$.

4.5 Conclusion

In this chapter the RFA measurement system used to measure E-cloud in the Main Injector was described. The RFA system is located in the MI-10 SEY test stand area. The RFA is capable of measuring E-cloud generation with turn-by-turn resolution over the full MI acceleration cycle. The peak-to-valley (maximum signal minus minimum for RFA measurement and simulation over one turn) and mean-to-valley (average signal minus minimum for RFA measurement and simulation over one

turn) RFA signal was measured for 8 different beam intensities and studied. Only the highest three intensities, 45×10^{12}, 48×10^{12} and 50×10^{12}, produced a significant E-cloud. With high enough beam intensity the RFA signal is inversely correlated to the bunch length development over the acceleration cycle.

The bunch length dependency of the RFA signal was compared to POSINST simulation, especially for the three highest beam intensities studied experimentally. The POSINST simulation showed that the E-cloud bombardment rate was very sensitive to input parameters corresponding to machine conditions, such as bunch length, SEY value of the beampipe material, and the beam intensity. Specifically, when the measured SEY, beam intensity, and measured/constructed bunch lengths were used as input parameters for the simulation, the E-cloud bombardment over the acceleration cycle was in good agreement with data. When the input parameters stray from these values, the acceleration cycle dependence of the bombardment rate no longer matches data well. Higher SEY values or intensities result in bombardment rates which do not change significantly over the acceleration cycle, but stay up at some 'saturated' level throughout the cycle, rather than building up significantly as the bunch length shortens from 1.5 ns to 1 ns during acceleration. Lower beam intensities or SEY values do not result in significant E-cloud.

The qualitative simulation results are in excellent agreement with data, while a comparison of the estimated bombarment rate at the detector to the rate calculated by the simulation differ by a factor of seven. This quantitative disagreement is almost to be expected since the estimated bombardment rate at the detector is based on many parameters that are not directly measured. These include the detector acceptance, angular distribution of electrons in the E-cloud, and signal processing details. It is concluded that the simulation may still be used for predictive purposes due to the excellent qualitative agreement when effort is made to provide the simulation with

accurate input parameters. The simulation is, in fact, quite sensitive to the input parameters which both builds confidence in the results and underlines the necessity of providing accurate information on machine conditions to get meaningful results.

Conversely, the RFA signal trend with bunch length and beam intensity could be used to estimate the SEY at the RFA location. If the bombardment rate is not saturated throughout the cycle, it indicates that the conditioning process is nearing completion. When the beampipe is conditioning or conditions, fewer secondaries are produced, reducing E-cloud, especially at longer bunch lengths. As the E-cloud drops, less conditioning is possible, so the SEY will not decrease much further. Based on this, the current RFA signal suggests that the conditioning process for the MI-10 vacuum chamber is stopped or on the edge of stopping. Based on the figure 4.20 for PIP-II beam intensity (70×10^{12}) the SEY at the test stand will condition to about 1.23.

CHAPTER 5
CONCLUSION

This research was a study of unwanted electrons known as E-cloud that are generated in the vacuum chamber of the the Fermilab Main Injector (MI). This work extends studies done previously at Fermilab [2, 3], both by detailing the evolution of the Secondary Electron Yield coefficent (SEY) for several materials, and by fruitful comparisons of simulation results to direct measurements of electron cloud under various conditions. The research used an in-situ SEY measurement test stand located at MI-10 to measure the SEY for SS316L, TiN and A-Carbon coatings in the environment of the operating accelerator. The POSINST E-cloud build-up code was used to simulate the E-cloud build up process. A Retarding Field Analyzer (RFA) was used to directly measure the E-cloud build up process at MI-10 area of the Main Injector, where the SEY test stand is located.

5.1 SEY measurements

Operational improvements were made to the in-situ SEY measurement test stand. A written operating procedure was produced [62]. The test stand operation will be continued and there are plans to study other materials besides the ones studied here in the future. The test stand was used to measure the SEY of SS316L, TiN and A-Carbon coatings, materials of interest. The MI beam pipe is made from SS316L stainless steel. TiN and A-Carbon coatings lower the SEY of the beam pipe surface, and could be utilized if E-cloud cannot otherwise be controlled.

During the operation of the SEY test stand, the biggest source of error, leakage current was studied, and a strategy of reducing the leakage current was developed. The leakage current is caused by moisture in the isolating ceramic and non-infinite resistance between cables and the surrounding metal ($< 1\ T\Omega$). The capacitively

induced current from the surrounding environment causes variation in the leakage current. Based on these studies, a nitrogen feeding system was built to prevent moisture on the isolating ceramic. A Faraday box was built to reduce the leakage current variation. The leakage current is controlled to be under 500 pA for a majority of SEY measurements. The leakage current variation is controlled to be under 10 pA, which brings about a 2% error to the SEY measurements.

The TiN and A-Carbon coated samples were studied with SS316L samples next to them as comparison samples. The SS316L SEY value started at 2.2 and conditioned to 1.25. The TiN SEY value started at 2.1 and conditioned to 1.18. The A-Carbon SEY value started at 1.26 and conditioned to 0.82.

During an SEY measurement, it was discovered that when samples were stored in the measurement position, isolated from the clean beam pipe and exposed to the less clean surrounding surface of the test stand, the SEY increased. This observation inspired a series of deconditioning studies. The conditioned SEY is well preserved by the MI vacuum chamber, but venting the vacuum resets the SEY to its deconditioned value. Since it then takes an integrated beam intensity of 10^{20} to condition again, either the unconditioned SEY must be low enough not to disrupt operations, or a conditioning period must be expected once the accelerator is turned on again after venting has occurred.

5.2 The POSINST simulations

POSINST is a build-up code used to simulate the E-cloud generation process, using real accelerator parameters and the SEY as input. The POSINST code tracks electrons in a 3D space and solves the electric field based on the 2D electron distribution. The code treats the proton distribution of the beam as a fixed input parameter and does not allow the proton distribution to change. The goal here was to

determine what conditions can lead to dangerous E-cloud build up, not to study the beam dynamics once there is an E-cloud problem. POSINST is a suitable code for this purpose. POSINST can output a lot of E-cloud related information. Some useful information includes the E-cloud density, bombardment rate, electron distribution, energy distribution. Initially a simulation of the E-cloud density dependence on the beam intensity for the MI was compared to an old simulation result generated by the author of the POSINST code, M.A. Furman. Good agreement verified correct use of the code before simulation studies commenced.

Simulation results demonstrate major factors that influence E-cloud density; for example, the electron distribution can be altered by a background magnetic field. When there are no externally applied or stray magnetic fields, the E-cloud is more evenly distributed inside the beam pipe. The presence of a dipole field confines the electron motion to helical trajectories around the direction of the field.

The POSINST simulation was used to generate E-cloud density or electron bombardment rates for direct comparison to measured bombardment rates in beam studies. The dependence of the bombardment rate on beam intensity, bunch length, and fill pattern over the MI acceleration cycle was studied. In order to insure faithful representation from the simulation results, care was taken to accurately determine the input parameters.

A rule of thumb for estimating when E-cloud density could cause beam instability is based on Sergey A. Antipov's [3] study of a RR instability. It was found that in order for a RR instability to happen, the E-cloud and the beam should have comparable linear charge density. The linea charge density of the beam was calculated for current and upgrade intensities. Then, assuming the same linear electron cloud density, the corresponding E-cloud volume charge density was determined. It was found that for current and future proton intensities the E-cloud density would have to be on

Table 5.1. Beam intensity for each stage of the MI, corresponding safe and danger SEY threshold

	Before PIP-I	PIP-I	Current upgrade	PIP-II
Beam power	400kW	700kW	900kW	1.2MW
Beam intensity (protons)	24×10^{12}	50×10^{12}	55×10^{12}	70×10^{12}
SEY threshold danger to instability (10^{12} electrons/m^3, 4.4×10^9 electrons/m)				
Dipole region	1.57	1.39	1.39	1.37
Safe operation SEY threshold (10^{10} electrons/m^3, 4.4×10^7 electrons/m)				
Dipole region	1.25	1.17	1.17	1.17

the order of 10^{12} electrons/m^3 to be comparable to the beam and potentially cause an instability. The SEY and beam intensity combinations that would cause E-cloud to reach this density threshold were examined using POSINST simulations. These simulations were used to find combinations of SEY and beam intensity for which the E-cloud density falls below 10^{12}, 10^{10} and 10^8 electrons/m^3. When the E-cloud density is above 10^{12} electrons/m^3, E-cloud related instabilities are likely to happen. Since the E-cloud density grows rapidly with SEY, an SEY below 10^{10} electrons/m^3 is taken as a safe E-cloud level. The E-cloud density of 10^{10} was chosen since there is a sufficient margin away from E-cloud saturation. The lowest SEY that could produce the dangerous E-cloud density of 10^{12} and the lowest SEY that could produce the safe E-cloud density of 10^{10} are calculated for each stage of MI upgrade. These SEY thresholds are shown in Table 5.1. For example, for the PIP-II beam intensity, an SEY above 1.37 could potentially cause an instability, while an SEY below 1.17 would ensure safe operation.

5.3 RFA measurements

The RFA detector is used to measure the E-cloud generation process, and it is located near the MI SEY test stand location. Since the SEY is then well-known at the RFA, it may be used as the SEY value input for POSINST, and the RFA measurement results may be directly compared with POSINST simulation results.

The RFA signal analysis procedure was developed. The high frequency beam image current induced noise was removed with numerical averaging. The turn-by-turn RFA signal peak was compared to the minium signal level (peak-to-valley), and the average signal level compared to the minium signal level (mean-to-valley) for each cycle to eliminate the effect of low frequency drift in the signal level. In this way it was possible to extract reasonable data on the E-cloud bombardment evolution over an acceleration cycle.

Obtaining the bunch length over the acceleration cycle was particularly challenging since a continuous measurement of bunch length is not available. A set of bunch length measurements at different times in the acceleration cycle were taken with the wall current monitor, and then these measurements were used to scale the output of BlonD. The BlonD simulation code can calculate the bunch length over the cycle as long as certain operating parameters of the machine are provided.

The POSINST simulation (using BlonD bunch lengths) generates the E-cloud bombardment rate over the full acceleration cycle. In order for the simulated rate over a full acceleration cycle to match the RFA signal data, the simulated bombardment rate must shift from a non-saturated value to a saturation peak when the bunch length shortens from 1.5 ns to 1 ns after transition. It was found that The RFA signal trend was only reproduced when the SEY scaling input was between 1.225 to 1.25. The SEY measured on July 25th 2019 was 1.25, and the measurement was made 2 weeks

before the RFA studies were done.

A conversion factor for scaling the measured RFA signal voltage to the E-cloud bombardment rate on the beam pipe surface was calculated based on the RFA circuitry, detector geometry, and the simulated angle distribution of the cloud electrons. There is a factor of seven difference in the simulated bombardment rate and the measurement-based bombardment rate (at SEY=1.25). In spite of this, the simulation results are assumed to be accurate because of their sensitivity to direct input parameters such as the SEY. A slight shift in the SEY input away from the measured SEY produces a completely different trend in the simulated bombardment rate compared to the measurement. The numerical value of the bombardment rate is not a directly measured parameter, so it is reasonable to have confidence in the simulation results in spite of the numerical difference with respect to the estimated bombardment rate.

Based on the previous conditioning studies [31], the RFA trend can be used to determine the SEY conditioning limit. A bombardment rate ratio for 1.43 ns bunch length to 0.9 ns bunch length ($R_{1.42}/R_{0.9}$) can be used to determine where will the conditioning process ends. Based on this simulation result, the SEY conditioning limit for up to PIP-II beam intensity has been calculated.

5.4 SEY coating choice for Fermilab upgrades

The most straightforward way to control E-cloud density is to ensure that the SEY of the beampipe material is sufficiently low. Based on these studies, achieving an SEY of 1.17 would ensure safe operation of the accelerator, generating an E-cloud at a 10^{10} electrons/cm^3 level. On the other hand, an SEY of 1.37 would generate an E-cloud level dangerous to operations (10^{12} electrons/cm^3). While TiN, A-Carbon and SS316L could all condition to an SEY below the dangerous 1.37 level, both SS316L

and TiN coated SS316L decondition to signifcantly higher SEY. Deconditioning occurs when the vacuum chamber is not maintained at high vacuum or is vented. This may happen during long shutdowns, and the resulting higher SEY values could be disruptive to operations for up to a few months. An SEY of 1.17 can be achieved by TiN and A-Carbon but not SS316L based on SEY measurements, which means A-Carbon and TiN can both help MI achieve safe operation. However, the A-Carbon is the best candidate for an E-cloud suppression coating, because the SEY for A-Carbon starts at 1.25, which is below the 1.37 SEY danger threshold and an SEY below 1 is achieved which will completely suppress E-cloud generation.

BIBLIOGRAPHY

[1] J. Eldred, N. Eddy, M.-J. Yang, J. Thangaraj, I. Kourbanis, Y. Ji, P. Adamson, R. Zwaska, D. Morris, and D. Capista, "Fast transverse instability and electron cloud measurements in fermilab recycler," tech. rep., 2015.

[2] M. Backfish, J. Eldred, C.-Y. Tan, and R. Zwaska, "Beam tests of beampipe coatings for electron cloud mitigation in fermilab main injector," *IEEE Transactions on Nuclear Science*, vol. 63, no. 2, pp. 957–964, 2015.

[3] S. A. Antipov, *Fast transverse beam instability caused by electron cloud trapped in combined function magnets*. Springer, 2018.

[4] J. S. Eldred, M. Backfish, C.-Y. Tan, and R. Zwaska, "Electron cloud measurements in fermilab main injector and recycler," tech. rep., 2015.

[5] A. de Gouvea and N. Saoulidou, "Fermilab's intensity frontier," *Annual Review of Nuclear and Particle Science*, vol. 60, pp. 513–538, 2010.

[6] S. Kopp, "The numi neutrino beam at fermilab," in *Proceedings of the 2005 Particle Accelerator Conference*, pp. 1–3, IEEE, 2005.

[7] J. Bian, "The nova experiment: overview and status," *arXiv preprint arXiv:1309.7898*, 2013.

[8] D. Collaboration, R. Acciarri, M. Acero, M. Adamowski, C. Adams, P. Adamson, S. Adhikari, Z. Ahmad, C. Albright, T. Alion, *et al.*, "Long-baseline neutrino facility (lbnf) and deep underground neutrino experiment (dune) conceptual design report volume 2: the physics program for dune at lbnf," 2016.

[9] R. K. Kutschke, "The mu2e experiment at fermilab," in *AIP Conference Proceedings*, vol. 1182, pp. 718–721, AIP, 2009.

[10] F. Jegerlehner and A. Nyffeler, "The muon g-2," *Physics Reports*, vol. 477, no. 1-3, pp. 1–110, 2009.

[11] R. Ainsworth, B. Brown, M.-J. Yang, K. Hazelwood, M. Xiao, I. Kourbanis, P. Adamson, D. Morris, and D. Capista, "High intensity proton stacking at fermilab: 700 kw running," tech. rep., 2018.

[12] W. Pellico, F. Garcia, K. Domann, R. Zwaska, K. Seiya, and K. Gollwitzer, "Fnal-the proton improvement plan (pip)," tech. rep., 2014.

[13] J. Eldred and R. Zwaska, "Dynamical stability of slip-stacking particles," *Physical Review Special Topics-Accelerators and Beams*, vol. 17, no. 9, p. 094001, 2014.

[14] R. Ainsworth, S. Chaurize, E. Stern, and I. Kourbanis, "Transition crossing in the main injector for pip-ii," tech. rep., 2017.

[15] S. Holmes, S. Mishra, V. P. Yakovlev, P. Derwent, V. Lebedev, and D. Mitchell, "Pip-ii status and strategy," tech. rep., 2015.

[16] F. Zimmermann, "Electron-cloud effects in past and future machines-walk through 50 years of electron-cloud studies," *arXiv preprint arXiv:1308.1274*, 2013.

[17] G. Rumolo, J. Esteban-Muller, G. Arduini, T. Pieloni, G. Maury Cuna, W. Höfle, C. Zannini, W. Venturini Delsolaro, V. Kain, N. Mounet, *et al.*, "Electron cloud observation in the lhc," tech. rep., 2011.

[18] G. Arduini, T. Bohl, E. Métral, K. Cornelis, F. Zimmermann, and W. Höfle, "Beam observations with electron cloud in the cern ps and sps complex," 2005.

[19] W. Fischer, M. Blaskiewicz, J. Brennan, H. Huang, H.-C. Hseuh, V. Ptitsyn, T. Roser, P. Thieberger, D. Trbojevic, J. Wei, *et al.*, "Electron cloud observations and cures in the relativistic heavy ion collider," *Physical Review Special Topics-Accelerators and Beams*, vol. 11, no. 4, p. 041002, 2008.

[20] I. Ben-Zvi, J. Kewisch, J. Murphy, and S. Peggs, "Accelerator physics issues in erhic," *Nuclear Instruments and Methods in Physics Research Section A: Accelerators, Spectrometers, Detectors and Associated Equipment*, vol. 463, no. 1-2, pp. 94–117, 2001.

[21] H. Fukuma, "Electron cloud effects at kekb," 2002.

[22] Y. Suetsugu, H. Fukuma, M. Tobiyama, K. Ohmi, and K. Shibata, "Study to mitigate electron cloud effect in superkekb," 2019.

[23] G. Zhi-Yuan, L. Yu-Dong, Q. Qing, W. Jiu-Qing, and X. Jun, "The studies of electron cloud instability in the bepc," *Chinese Physics C*, vol. 30, no. S1, pp. 102–104, 2006.

[24] X. Zhang, A. Z. Chen, W. Chou, B. M. Hanna, K. Y. Ng, J.-F. Ostiguy, L. Valerio, and R. M. Zwaska, "Electron cloud studies at tevatron and main injector," in *2007 IEEE Particle Accelerator Conference (PAC)*, pp. 3501–3503, IEEE, 2007.

[25] R. Zwaska, "Electron cloud experiments at fermilab: Formation and mitigation," *arXiv preprint arXiv:1203.1936*, 2012.

[26] A. Dekker, "Secondary electron emission," in *Solid State Physics*, vol. 6, pp. 251–311, Elsevier, 1958.

[27] H. Bruining, *Physics and Applications of Secondary Electron Emission: Pergamon Science Series: Electronics and Waves—a Series of Monographs*. Elsevier, 2016.

[28] E. Somersalo, D. Proch, and P. Yla-Oijala, "Electron multipacting in rf structures," tech. rep., 1994.

[29] J. R. M. Vaughan, "Multipactor," *IEEE Transactions on electron devices*, vol. 35, no. 7, pp. 1172–1180, 1988.

[30] H. Seiler, "Secondary electron emission in the scanning electron microscope," *Journal of Applied Physics*, vol. 54, no. 11, pp. R1–R18, 1983.

[31] V. Baglin, J. Bojko, C. Scheuerlein, O. Gröbner, M. Taborelli, B. Henrist, and N. Hilleret, "The secondary electron yield of technical materials and its variation with surface treatments," tech. rep., 2000.

[32] R. E. Kirby and F. King, "Secondary electron emission yields from pep-ii accelerator materials," *Nuclear Instruments and Methods in Physics Research Section A: Accelerators, Spectrometers, Detectors and Associated Equipment*, vol. 469, no. 1, pp. 1–12, 2001.

[33] N. Hilleret, C. Scheuerlein, and M. Taborelli, "The secondary-electron yield of air-exposed metal surfaces," *Applied Physics A*, vol. 76, no. 7, pp. 1085–1091, 2003.

[34] C. Yin Vallgren, *Low secondary electron yield carbon coatings for electron cloud mitigation in modern particle accelerators*. No. CERN-THESIS-2011-063, CERN, 2011.

[35] C. Y. Vallgren, G. Arduini, J. Bauche, S. Calatroni, P. Chiggiato, K. Cornelis, P. C. Pinto, B. Henrist, E. Métral, H. Neupert, *et al.*, "Amorphous carbon coatings for the mitigation of electron cloud in the cern super proton synchrotron," *Physical Review Special Topics-Accelerators and Beams*, vol. 14, no. 7, p. 071001, 2011.

[36] M. Nishiwaki and S. Kato, "Residual gas analysis and electron cloud measurement of dlc and tin coated chambers at kekb ler," *Proc. IPAC*, 2010.

[37] M. Nishiwaki and S. Kato, "Residual gas analysis and electron cloud measurement of dlc and tin coated chambers at kekb ler," *Proc. IPAC*, 2010.

[38] A. Kulikov, A. Fisher, S. Heifets, J. Seeman, M. Sullivan, U. Wienands, and W. Kozanecki, "The electron cloud instability at pep-ii," in *PACS2001. Proceedings of the 2001 Particle Accelerator Conference (Cat. No.01CH37268)*, vol. 3, pp. 1903–1905 vol.3, June 2001.

[39] G. Bellodi, "Code comparisons and benchmarking with different sey models in electron cloud build-up simulations," 2005.

[40] M. A. Furman and M. T. F. Pivi, "Probabilistic model for the simulation of secondary electron emission," *Phys. Rev. ST Accel. Beams*, vol. 5, p. 124404, 2002. [Erratum: Phys. Rev. ST Accel. Beams16,no.6,069901(2013)].

[41] M. Furman and M. Pivi, "Simulation of secondary electron emission based on a phenomenological probabilistic model," tech. rep., Lawrence Berkeley National Lab.(LBNL), Berkeley, CA (United States), 2003.

[42] F. Zimmermann, "A simulation study of electron-cloud instability and beam-induced multipacting in the lhc," tech. rep., 1997.

[43] O. S. Brüning, "Simulations for the beam-induced electron cloud in the lhc beam screen with magnetic field and image charges," tech. rep., 1997.

[44] O. S. Brüning, "Numerical simulations for the beam-induced electron cloud in the lhc beam screen," tech. rep., 1998.

[45] O. S. Brüning, "Numerical simulations for the beam-induced electron cloud in the lhc beam screen," tech. rep., 1998.

[46] G. Rumolo, F. Ruggiero, and F. Zimmermann, "Simulation of the electron-cloud build up and its consequences on heat load, beam stability, and diagnostics," *Physical Review Special Topics-Accelerators and Beams*, vol. 4, no. 1, p. 012801, 2001.

[47] J.-L. Vay, A. Friendman, and D. Grote, "Self-consitstent simulations of high-intesity beams and e-clouds with warp posinst," 2006.

[48] J.-L. Vay, C. M. Celata, M. Furman, M. Venturini, K. G. Sonnad, G. Penn, and D. Grote, "Update on electron-cloud simulations using the package warp-posinst," tech. rep., Lawrence Berkeley National Lab.(LBNL), Berkeley, CA (United States), 2009.

[49] M. Furman, I. Kourbanis, and R. Zwaska, "Status of electron-cloud build-up simulations for the main injector," 2010.

[50] U. Iriso, *Electron Clouds in the Relativistic Heavy Ion Collider*. PhD thesis, PhD Thesis, Univ. of Barcelona, 2006.

[51] W. Hartung, D. Asner, J. Conway, C. Dennett, S. Greenwald, J.-S. Kim, Y. Li, T. Moore, V. Omanovic, M. Palmer, *et al.*, "In-situ measurements of the secondary electron yield in an accelerator environment: Instrumentation and methods," *Nuclear Instruments and Methods in Physics Research Section A: Accelerators, Spectrometers, Detectors and Associated Equipment*, vol. 783, pp. 95–109, 2015.

[52] D. Scott, D. Capista, K. Duel, R. Zwaska, S. Greenwald, W. Hartung, Y. Li, T. Moore, M. Palmer, R. Kirby, *et al.*, "Secondary electron yield measurements of fermilab's main injector vacuum vessel," *arXiv preprint arXiv:1301.6989*, 2013.

[53] M. W. Evans, F. H. Harlow, and E. Bromberg, "The particle-in-cell method for hydrodynamic calculations," tech. rep., Los Alamos National Lab NM, 1957.

[54] E. Aschenauer, M. Baker, A. Bazilevsky, K. Boyle, S. Belomestnykh, I. Ben-Zvi, S. Brooks, C. Brutus, T. Burton, S. Fazio, *et al.*, "erhic design study: An electron-ion collider at bnl," *arXiv preprint arXiv:1409.1633*, 2014.

[55] G. Apollinari, I. Béjar Alonso, O. Brüning, M. Lamont, and L. Rossi, "High-luminosity large hadron collider (hl-lhc): Preliminary design report," tech. rep., Fermi National Accelerator Lab.(FNAL), Batavia, IL (United States), 2015.

[56] X. Zhang, A. Z. Chen, W. Chou, B. M. Hanna, K. Y. Ng, J.-F. Ostiguy, L. Valerio, and R. M. Zwaska, "Electron cloud studies at tevatron and main injector," in *2007 IEEE Particle Accelerator Conference (PAC)*, pp. 3501–3503, IEEE, 2007.

[57] R. Rosenberg and K. Harkay, "A rudimentary electron energy analyzer for accelerator diagnostics," *Nuclear Instruments and Methods in Physics Research Section A: Accelerators, Spectrometers, Detectors and Associated Equipment*, vol. 453, no. 3, pp. 507–513, 2000.

[58] "Cern beam longitudinal dynamics code blond http://blond.web.cern.ch."

[59] L. McCuller, "Simulations and testing of retarding field analyzers for electron cloud monitoring," tech. rep., 2009.

[60] R. Ainsworth, S. Chaurize, E. Stern, and I. Kourbanis, "Transition crossing in the main injector for pip-ii," tech. rep., 2017.

[61] R. Ainsworth, I. Kourbanis, E. Stern, and M. Xiao, "Transition simulations for the main injector.".

[62] J. E. Yichen Ji, "Operation of sey test stand experiment at mi-10," *Beams Document 4947-v2*.